EES Catalysis

REVIEW ARTICLE

View Article Online
View Journal | View Issue

Cite this: *EES Catal.*, 2024, 2, 411

Crystalline carbon nitrides for photocatalysis

Han Li,[ab] Bei Cheng,[ac] Jingsan Xu,[d]* Jiaguo Yu[e] and Shaowen Cao[ac]*

Received 10th December 2023,
Accepted 5th January 2024

DOI: 10.1039/d3ey00302g

rsc.li/eescatalysis

Photocatalysis is considered as an effective approach to address energy and environmental issues. Carbon nitride (CN) is a promising metal-free semiconductor photocatalyst because of its unique properties such as tunable electronic band structure, facile/cheap synthesis and high chemical stability. However, the pristine CN prepared by the traditional thermal polymerization method is usually an amorphous or semi-crystalline conjugated bulk with a high density of structural defects, resulting in its moderate photocatalytic activity. Increasing the crystallinity of CN is an effective strategy to enhance its photocatalytic activity, and a few methods have been proposed, including high-temperature and high-pressure treatment, ionothermal method, solvothermal synthesis and microwave-assisted thermal polymerization. This review summarizes recent advances in the preparation of crystalline carbon nitrides (CCNs) and the design of CCNs-based photocatalysts in terms of nanostructure design, molecular structure engineering and construction of CCNs-based heterojunctions. In addition, their applications in a range of photocatalysis fields such as water splitting, carbon dioxide reduction, degradation of pollutants, organic synthesis and H_2O_2 production are reviewed. Finally, the concluding remarks are presented as well as challenges and prospects for future development of CCNs-based photocatalysts.

Broader context

The excessive consumption of fossil fuel has not only led to energy shortages, but also resulted in environmental pollution. Semiconductor-based photocatalysis is recognized as an effective strategy to alleviate the above issues since it can directly convert clean solar energy into valuable chemical fuels and degrade pollutants. Carbon nitride (CN) has emerged as a promising photocatalyst due to its unique properties including tunable electronic structure, facile/cheap synthesis and high chemical stability. However, pristine CN suffers from limited light absorption and severe charge recombination, thus resulting in moderate photocatalytic activity. Improving the crystallinity of CN has been demonstrated as an effective approach to enhance the photocatalytic performance because of the improved charge transfer, reduced bulk defects and enhanced light absorption. This review summarizes recent advances in the preparation of crystalline carbon nitrides (CCNs) and the design of CCNs-based photocatalysts in terms of nanostructure design, molecular structure engineering and construction of CCNs-based heterojunctions. In addition, their applications in a range of photocatalysis fields are reviewed. Finally, the challenges and prospects for future development of CCNs-based photocatalysts were also discussed. We hope that this review could provide valuable insights for designing highly efficient CCNs-based photocatalysts for energy and environmental applications.

1. Introduction

Semiconductor-based photocatalysis is recognized as an effective solution to the energy shortage and environmental pollution since it can directly convert clean solar energy into valuable chemical fuels such as hydrogen and hydrocarbon, selectively synthesize organic compounds, and degrade organic pollutants.[1–6] In the past decades, various semiconductors (such as TiO_2,[7–9] Fe_2O_3,[10] ZnO,[11] Bi_2WO_6,[12] $BiVO_4$,[13] CdS,[14] *etc.*) have been investigated as photocatalysts for solar-to-chemical energy conversion. However, the large band gap of metallic oxide semiconductors restricts the applications of photocatalysis due to the insufficient utilization of sunlight. While metal sulfides have also been considered due to their narrow band gap and appropriate conduction band positions, their further applications were limited by the disadvantages including chemical instability due to photo-corrosion and self-oxidation.[15] Therefore, the development of photocatalysts with visible-light activity and chemical stability has become a popular research topic and major task for a long time.

[a] State Key Laboratory of Advanced Technology for Materials Synthesis and Processing, Wuhan University of Technology, Wuhan 430070, P. R. China. E-mail: swcao@whut.edu.cn
[b] School of Materials Science and Engineering, Hubei University of Automotive Technology, Shiyan 442020, P. R. China
[c] Hubei Technology Innovation Center for Advanced Composites, Wuhan University of Technology, Wuhan 430070, P. R. China
[d] School of Chemistry and Physics, Queensland University of Technology, Brisbane, QLD 4000, Australia. E-mail: jingsan.xu@qut.edu.au
[e] Laboratory of Solar Fuel, Faculty of Materials Science and Chemistry, China University of Geosciences, Wuhan 430074, P. R. China

Polymeric carbon nitride has emerged as a promising candidate photocatalyst since 2009 due to its extraordinary properties, such as non-toxicity, low cost, easy preparation, high physicochemical stability, and well-matched band structure,[16] enabling its widespread applications in photocatalytic water splitting, carbon dioxide reduction, pollutant degradation, organic synthesis, *etc.*[17–22] Unfortunately, the pristine CN prepared by traditional thermal polymerization is usually an amorphous or semi-crystalline conjugated polymer with high-density of structural defects, leading to its moderate photocatalytic activity. The low crystallinity caused by incomplete polymerization leads to the formation of hydrogen bonds in the covalent CN framework. The intralayer hydrogen bonds in pristine CN hinder the in-plane electron conduction, resulting in poor intralayer transport. Theoretically, increasing the crystallinity of CNs not only enhances the transport of charge carriers and reduces the recombination rate of electron–hole pairs, but also extends the π-conjugated system and improves the light absorption capability. Therefore, reducing structural defects by increasing the crystallinity of CNs is a critical strategy to optimize their photocatalytic performance.[23–26] Notably, the kinetic hindrance is a dominant issue during bulk condensation, which leads to incomplete polymerization. Hence, it is highly desirable to promote the mass and heat transfer to improve the crystallinity. To this end, considerable effort has been made to prepare CCNs, including high-temperature and high-pressure strategy, ionothermal route, solvothermal approach and microwave-assisted thermal synthesis.

Up to now, there has been numerous publications on the design of CCNs-based photocatalysts for various applications, including several specific and inspiring reviews.[21,23,27,28] However, an overarching understanding on the preparation, design, mechanism and applications of CCNs-based photocatalysts is still lacking. Hence, we present a comprehensive review of the latest significant progress in the preparation, design, and applications of CCNs-based photocatalysts. Specifically, the development history of CNs will be introduced first, followed

Han Li

Han Li received his BE degree from North China University of Water Resources and Electric Power. Then he obtained his MS and PhD degrees in Materials Science and Engineering from Wuhan University of Technology. Now he works at the School of Materials Science and Engineering, Hubei University of Automotive Technology. His current research focuses on photocatalytic H_2O_2 production, CO_2 reduction, water splitting, and environmental purification.

Bei Cheng

Bei Cheng received her BS degree and MS degree from Tongji University, and her PhD degree from Wuhan University of Technology (WUT). In 2010, she became a Professor at WUT. Her research interests include semiconductor photocatalysis (such as photocatalytic hydrogen production, CO_2 reduction, H_2O_2 evolution, and so on) and the fabrication and application of environmental cleaning materials.

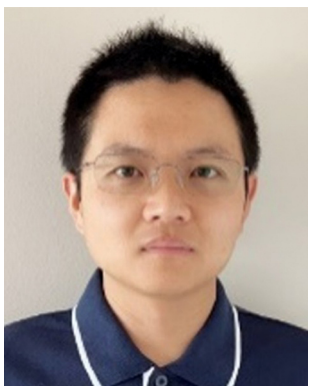

Jingsan Xu

Jingsan Xu received his BS degree in Materials Science and Engineering in 2008 from Jilin University, and his PhD degree in 2013 from Shanghai Institute of Ceramics, Chinese Academy of Sciences. Then he finished the postdoctoral work from 2013 to 2016 in the Max Planck Institute of Colloids and Interfaces. He commenced as an ARC DECRA fellow at QUT in 2016 was promoted to full professor in 2021. His research field is focused on solar energy harvesting, catalysis and interfaces. One topic he is particularly interested in is light-driven chemical reactions, such as organic synthesis, supramolecular assembling, crystal transformations.

Jiaguo Yu

Jiaguo Yu received his BS degree and MS degree in Chemistry from Central China Normal University and Xi'an Jiaotong University, respectively, and his PhD degree in Materials Science from Wuhan University of Technology (WUT). In 2000, he became a Professor at WUT. In 2021, he moved to China University of Geoscience (Wuhan). His research interests include semiconductor photocatalysis, photocatalytic hydrogen production, CO_2 reduction, perovskite solar cells, electrocatalysis, and so on. He is a foreign member of Academia Europaea (2020), foreign fellow of the European Academy of Sciences (2020), and fellow of the Royal Society of Chemistry (2015).

by the synthesis method and design of CCNs-based photocatalysts. Then the applications of CCNs-based photocatalysts in water splitting, carbon dioxide reduction, pollutant removal and organic synthesis, and H_2O_2 production are presented. Finally, the concluding criticism and perspectives on the challenges and future development of CCNs-based photocatalysts are briefly discussed.

2. Discovery and development history of CNs

To gain a comprehensive understanding of CNs, it is necessary to discuss their development history (Fig. 1a), which dates back to 1834, when Berzelius first synthesized a linear polymer, named "melon" by Liebig.[29] A more in-depth understanding of the composition and structure of these compounds was described by Franklin in 1922.[30] Pauling and Sturdivant proposed in 1937 that the coplanar tri-*s*-triazine unit was the basic structural unit of these polymeric derivatives, which was confirmed by X-ray studies.[31] Later, Redemann and Lucas[32] deduced that the 21 molecules of 2,5,8-triamino-tris-*s*-triazine, that is, $C_{126}H_{21}N_{175}$ may be the oligomeric condensation product of carbon nitride, which was earlier described by Franklin. Based on these findings, it can be concluded that it is not possible to assign a single structure to melon, as it is a mixture of molecules of different sizes and nanostructures.

This melon-based CNs were forgotten for a long time as an unproven species, owning to chemical inertness and poor solubility. Surprisingly, interest in CNs was revived in 1989, as it was theoretically predicted that by replacing Si with C in β-Si_3N_4, the sp^3-bonded C_3N_4 phase (β-C_3N_4) exhibited extremely high bulk modulus and hardness values, which could compare with, even exceed that of diamond.[33] Later, theoretical investigations conducted by Teter and Hemley further confirmed this prediction. Meanwhile, five different phases of CNs were predicted, including α-C_3N_4, β-C_3N_4, cubic C_3N_4, pseudocubic C_3N_4 and graphitic C_3N_4 (g-C_3N_4).[34] These interesting results not only motivated experimental preparation of the hypothetical phase, but also stimulated further theoretical studies on CNs. However, the preparation of single-phase β-C_3N_4 was proved to be extremely challenging due to its low thermodynamic stability.[35] Further theoretical research confirmed that g-C_3N_4, with a graphite-like layered structure, is the most stable allotrope under ambient conditions.[36–38] However, the characterization of g-C_3N_4 is a challenging task due to its low crystallinity and high degree of disorder. Owing to the lack of experimental data, discussions about the actual existence of ideal g-C_3N_4 and its possible molecular structure are prevalent. It has been pointed out that the two basic structural units for the construction of g-C_3N_4 isomers are the triazine (C_3N_3) and tri-*s*-triazine/heptazine (C_6N_7) rings, respectively (Fig. 1b and c).[36,38–41] Moreover, the heptazine rings was energetically favorable over the triazine-based units.[42,43] The heptazine rings were interconnected through bridging imide bonds (Fig. 1c), and recent studies have demonstrated that the pyrolysis of cyanamide, dicyandiamide, or melamine yields a melon polymer composed of melem subunits,[42–52] indicating that this unit is the most robust and stable building block. Therefore, the heptazine-based g-C_3N_4

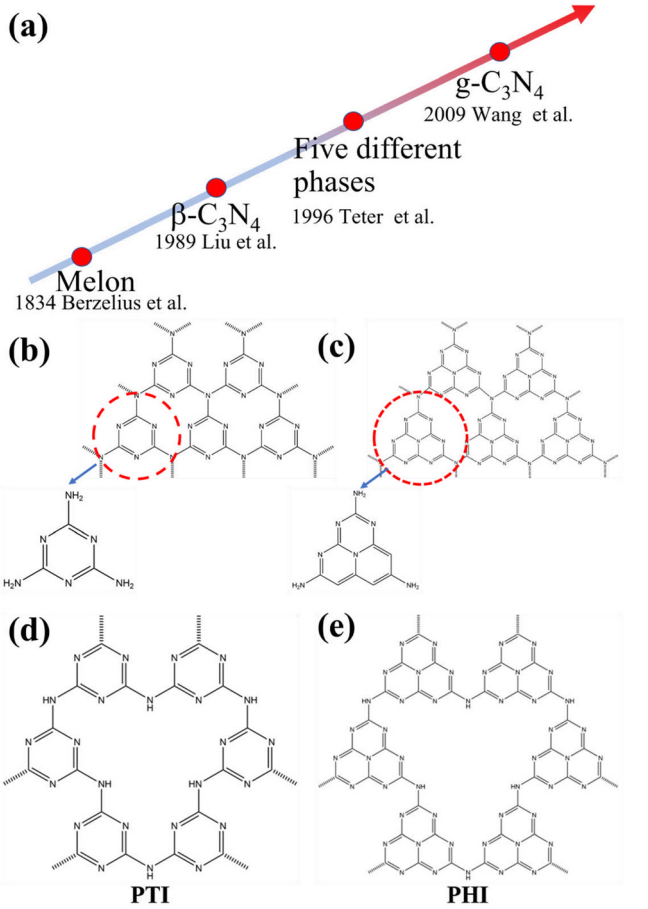

Fig. 1 (a) The roadmap of the development of carbon nitrides. (b) Triazine and (c) tri-*s*-triazine (heptazine) structures of g-C_3N_4. (d) Structures of poly(triazine imide) (PTI) and (e) poly(heptazine imide) (PHI).

Shaowen Cao

Shaowen Cao received his BS degree in Geochemistry in 2005 from University of Science and Technology of China, and his PhD degree in Materials Chemistry & Physics in 2010 from Shanghai Institute of Ceramics, Chinese Academy of Sciences. Then he was a Research Fellow at Nanyang Technological University until Feb 2014. From Mar 2018 to Feb 2020, he was a Visiting Scientist at Max Planck Institute of Colloids and Interfaces. He is now a professor at Wuhan University of Technology. His-current research interests include the design and fabrication of photocatalytic materials for energy and environmental applications.

has been extensively investigated in many fields, particularly in catalysis,[53,54] where the discovery of melon-based carbon nitride as a metal-free polymeric photocatalyst for water splitting was first proposed by Wang *et al.* in 2009.[16] Since then, the research on g-C_3N_4 as a metal-free polymeric conjugated photocatalyst has been nothing short of explosive. However, the pristine CN prepared by the traditional thermal polymerization method is a melon-based structure, which is amorphous or semi-crystalline and exhibits moderate photocatalytic activity.

In principle, increasing the crystallinity of the photocatalysts not only enhances the mobility of charge carriers and reduce recombination centers, but also extends the π-conjugated system and improves the light absorption capacity, thus enhancing the photocatalytic performance. Therefore, various approaches have been developed to synthesize CCNs. The actual crystal structure of CCNs were further confirmed because of their high crystallinity. Then, their crystal structure (Fig. 1d and e) was proposed and confirmed by density functional theory (DFT) calculations and experimental results. Kawaguchi *et al.* proposed a PTI-based CCNs structure (Fig. 1d), consisting of a two-dimensional (2D) plane framework of triazine units connected through NH groups.[39] While the PTI-based CCNs synthesized by molten salt method contains metal ions embedded in the interlayer or void. Schnick and co-workers presented the crystal structure of the PHI-based CCNs (Fig. 1e), which was composed of six heptazine subunits arranged in a hexagonal configuration and bridged by imide-bonds.[55] This connection scheme introduced a large pore space in the planner network compared with g-C_3N_4. Similarly, the alkali metal ions in the framework of PHI-based CCNs are generally located in the voids formed by the six heptazine units during the molten salt process. Moreover, the advantages of CCNs are summarized as follows: (1) the high crystallinity of CCNs could decrease the number of defects, thereby reducing the recombination centers of charge carriers. (2) The high crystallinity of CCNs could narrow the band gap due to the extended π-conjugated system. (3) The high crystallinity of CCNs could decresae the interlayer distance, which enhances interlayer exciton dissociation and improves the charge transport (conductivity).

3. Properties of CNs and CCNs

3.1. Thermal stability

Thermal gravimetric analysis (TGA) of the CN proved that the CN can remain stable up to 600 °C and above.[45] A significant endothermal peak is observed at 630 °C, as well as a continuous weight loss due to the breakdown of CN. The complete decomposition of CNs at 750 °C confirmed its high thermal stability.[16,56] The decomposition temperature of the CN could vary slightly depending on the different preparation procedures in literature,[39,45,57,58] probably due to the different degrees of polycondensation.

3.2. Chemical stability

The strong van der Waals force between the CN layers makes them prone to agglomerate and therefore insoluble in most solvents. No detectable dissolubility or reactivity of CNs was observed in conventional solvents, including H_2O, C_2H_5OH, DMF, THF, diethyl ether, and toluene.[58] To investigate the stability and durability of CNs in different solvents, CNs powder was dispersed in H_2O, acetone, ethanol, pyridine, acetonitrile, dichloromethane, DMF, acetic acid, and 0.1 M sodium hydroxide aqueous solution for 30 days. After that, the dispersed CNs were dried at 80 °C for 10 hours. Subsequently, the FTIR spectra of the impregnated CNs were measured and showed almost no change compared with the fresh ones, indicating their good chemical stability and excellent durability. In addition, CNs treated with a certain concentration of acid could form a colloidal dispersion or a true solution,[59,60] which however is reversible. The photochemical stability of CCNs was considered to be high in most previous studies. Nevertheless, Zou and co-workers reported that the photocatalytic performance of CCN nanotube was decreased because of the loss of K, Na, and Cl ions.[61] Rcently, Hou and co-workers proposed that the PHI-based CCN was unstable during the photocatalytic process due to the Na^+ loss.[62] Interestingly, the addition of NaCl could improve the stability. Therefore, it is reasonable to assume that the CCNs are suitable for photocatalytic reactions in seawater. In short, the photochemical stability of CCNs needs to be further investigated and the focus could be the relationship between the leaching of metal ions and the stability of photocatalytic activity.

3.3. Optical and electronic properties

The optical properties of CNs were tested by UV-vis diffuse reflectance spectroscopy and photoluminescence. As revealed by the theoretical calculation, the CNs are an n-type semiconductor featuring a bandgap up to 5 eV, depending mainly on the structural or geometrical diversity.[63] In fact, conventional CNs exhibit strong bandgap adsorption around 420 nm, which is in accordance with the light yellow color. Preparation approaches, including various precursors and polymerization temperature, may marginally affect the absorption edge of CNs, mainly due to different crystallinity, crystal structures, packing, particle size and defects.[16,56,64,65] Generally, the pristine CNs exhibits blue luminescence at room temperature. The photoluminescence (PL) was observed between 430 nm and 550 nm, with a peak around 470 nm. Time-resolved photoluminescence (TRPL) was used to investigate the charge transfer dynamics, exhibiting an average lifetime of ~5 ns.[66]

As revealed by the UV-vis diffuse reflectance spectroscopy, the CN possesses a bandgap of *ca.* 2.7 eV. While the conductive band (CB) and valence band (VB) are positioned at *ca.* −1.1 eV (*vs.* normal hydrogen electrodes) and *ca.* +1.6 eV (*vs.* normal hydrogen electrodes), respectively. This appropriate electronic band structure makes CNs a promising candidate for applications in solar energy conversion.

4. Synthesis and characterization of CCNs

Despite the in-depth research on the structure of CNs, the preparation of CCNs is still challenging. As we all know, the kinetic hindrance is the predominant issue during the

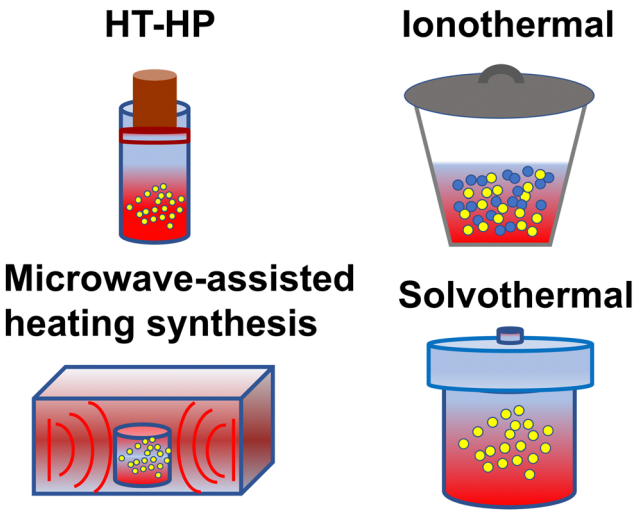

Fig. 2 Schematic diagram of synthesis method: high temperature-high pressure method, ionothermal route, microwave-assisted heating synthesis, and solvothermal approach.

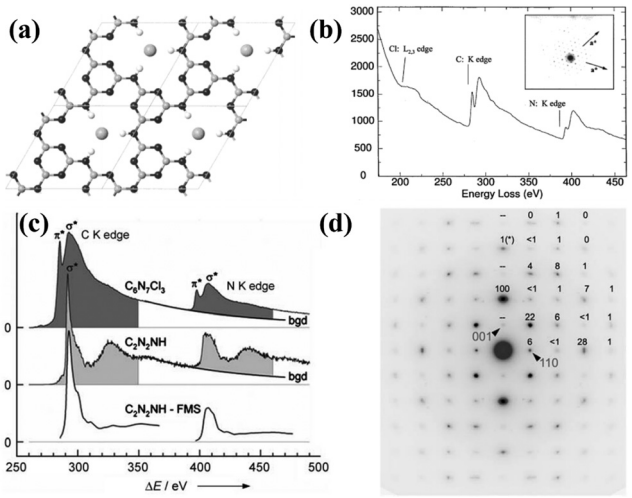

Fig. 3 (a) Proposed molecular structure of $C_6N_9H_3$·HCl. (b) EELS spectrum of $C_6N_9H_3$·HCl and the corresponding electron diffraction pattern (inset). Reproduced with permission.[73] Copyright 2001, American Chemical Society. (c) EELS spectrum of C and N K edges of the $C_6N_7Cl_3$ and C_2N_2(NH). (d) SAED pattern along the [$\bar{1}$10] zone of the orthorhombic cell of dwur-C_2N_2(NH). Reproduced with permission.[75] Copyright 2007, Wiley-VCH.

condensation process, which results in incomplete polymerization. To solve this problem, many strategies have been developed to promote the mass and heat transfer. Early attempts to prepare CCNs were based on thin film growth techniques using various physical and chemical vapor deposition approaches.[67–71] Considering that most photocatalysts are powder-based, in this review, the synthesis methods of CCNs are focused on bulk synthesis, as shown in Fig. 2.

4.1. High temperature-high pressure method

Inspired by the high-pressure synthesis of diamond from graphite, early attempts to prepare CCNs adopted the same approach. Weill and co-workers reported a new model of graphitic C_3N_4 with different carbon vacancies and layered structures.[72] The CCN was synthesized in a belt-type apparatus at 3 GPa and 800 °C using melamine as the precursor and hydrazine as the nitriding solvent. The XRD pattern of the sample indicates that it was an orthorhombic structure that could not be indexed according to the model proposed by Teter and Hemley.[34] Moreover, all the expected peaks of orthorhombic symmetry were absent and the relative intensities did not agree with the calculated results, mainly due to the effect of the internal pressure, which may lead to reorientation of the specimens. Wolf and co-workers reported another significant research for the preparation of CCN by the high temperature and high pressure (HT–HP) approach.[73] This novel CCN, containing stoichiometric amounts of HCl, was prepared through a solid-state reaction at 1.0–1.5 GPa and 500–550 °C using melamine and cyanuric chloride as precursors. This product had a two-dimensional $C_6N_9H_3$ framework belonging to the hexagonal space group ($P6_3/m$), which was similar to the structure proposed by Kouvetakis *et al.*,[74] but lacking one-third of the triazine rings (Fig. 3a). The vacancy was occupied by Cl^- ions and the N atoms in the framework were protonated to maintain charge balance. The electron energy-loss spectroscopy (EELS) revealed that both the C and N atoms were sp^2-hybridized (Fig. 3b). The electron diffraction pattern confirmed the hexagonal symmetry. Riedel and co-workers obtained a novel CCN phase with a well-defined structure and chemical composition by the HT–HP method.[75] In this study, $C_2N_4H_4$ was used as the single-source precursor, and the synthesis was performed at 1700–2300 °C and above 27 GPa. The electron energy-loss spectroscopy (EELS) indicates that the C atoms and N atoms were sp^3-hybridized (Fig. 3c). The as prepared CCN featured a 3D carbon nitride network and exhibited a defective wurtzite-type structure, which was confirmed by the electron-diffraction results (Fig. 3d) and DFT studies. In summary, even with some shortcomings like high temperature nitrogen loss, the HT–HP strategy is still an efficient approach to synthesize CCNs. More importantly, some precursors were proved to contribute to the synthesis of CCNs, but the application of CCNs synthesized by the HT–HP approach requires further research.

4.2. Ionothermal (molten salt) method

Kinetic barriers are a major problem in solid-state reactions, while a liquid environment would be more conducive to heat and mass transfer. Motivated by the application of the eutectic salt mixtures in organic syntheses and electrochemical processes, Thomas and co-workers first used ionothermal approach to synthesize CCN.[46] LiCl and KCl (45 : 55 wt%) were utilized as a good solvent because of its high-temperature stability, non-corrosiveness, good solvation of precursors and intermediates, and more importantly its melting point below the polycondensation point of s-heptazine. The XRD pattern (Fig. 4a) of CCN shows two sharp peaks at 12.1 and 26.5°, which was different from the melon-based CN synthesized by the traditional bulk condensation method. The obtained CCN had a hexagonal prism morphology due to the preferential growth in the *z*-direction,

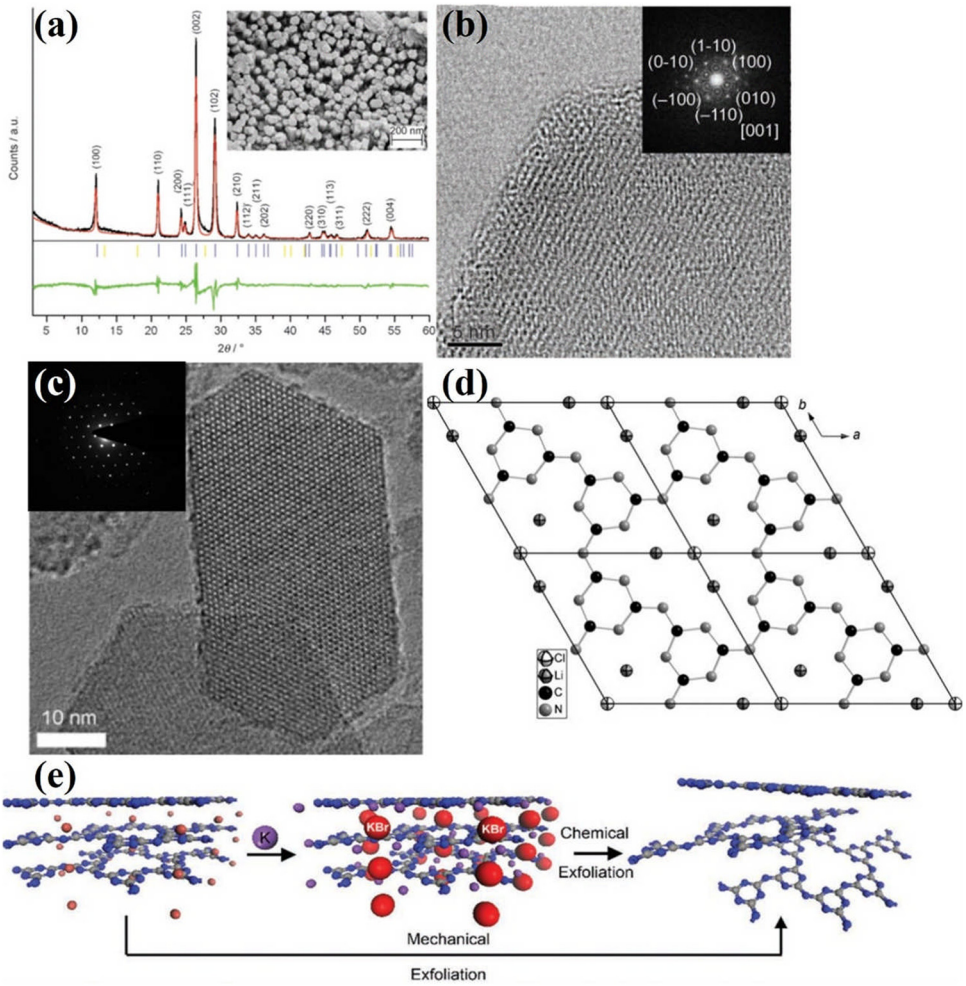

Fig. 4 (a) XRD pattern of CCN and SEM image of CCN (inset). (b) HRTEM image along the [001] axis and the corresponding SAED (inset). Reproduced with permission.[46] Copyright 2008, Wiley-VCH. (c) HRTEM image of PTI/Li^+Cl^- and the corresponding SAED pattern of the hk0 plane (inset). (d) Projection of the structure of single-layer PTI/Li^+Cl^- along the *c* axis. Reproduced with permission.[76] Copyright 2011, Wiley-VCH. (e) Schematic diagram of the preparation approach from PTI/Br to PTI nanosheet. Reproduced with permission.[79] Copyright 2013, Wiley-VCH.

confirming the single crystal property (Fig. 4a). The high crystallinity was further determined by high resolution transmission electron microscopy (HRTEM) image, the lattice fringes were clearly observed (Fig. 4b) and the crystal plane spacing measured by selected area electron diffraction (SAED) was consistent with the XRD results. However, the location of the residual chloride ions was unclear, which needs further investigation. Schnick and co-workers conducted a detailed structural characterization of CCN synthesized by ionothermal method using LiCl/KCl as solvent.[76] The solid-state nuclear magnetic resonance (NMR) spectroscopy, FTIR spectrum, and ^{15}N cross-polarization with polarization inversion (CPPI) experiments confirmed that the CCN was a 2D network constructed from imide-bridged triazine units rather than heptazine building blocks. Thus, the CCN was identified as poly(triazine imide) (PTI). The reason for this CCN consisting of triazine is probably because the molten salt destabilizes or even decomposes the heptazine units at higher temperatures, since the use of heptazine-based precursors, such as melem, also results in the formation of PTI at 600 °C. Several strong X-ray reflections of PTI suggest that the salt melting method leads to its high crystallinity. Interestingly, the interlayer spacing of 0.336 nm determined by the XRD result was significantly larger than that of other graphite-like CN condensation products, such as melon,[77] PHI[55] and $C_6N_9H_3{\cdot}HCl$.[73] This broadening of the interlayer spacing could be attributed to the incorporation of Cl ions. The HRTEM and SAED results (Fig. 4c) revealed the hexagonal symmetry and graphite-like stacking. The Cl^- ions were located at the in-plane voids and intercalated between the layers, while Li^+ ions also occupied the in-plane vacancy and were distributed around chloride ions for charge compensation. Hence, the CCN was also known as PTI/Li^+Cl^- due to the molecular structure and chemical composition (Fig. 4d).

Considering that interlayer distance and electronic properties can be modified by ionic intercalation, Bojdys and co-workers prepared CCN with adjustable interlayer distances by changing the eutectic melt.[78] Compared with the PTI/Li^+Cl^- (0.338 nm) prepared in KCl/LiCl eutectic mixture, the as-synthesized

poly(triazine imide) intercalated by bromide ions exhibited an expanded interlayer distance (0.352 nm). While the PTI/F showed a reduced gallery height due to smaller anions. Similar to the processing of bulk graphite into graphene, the bulk PTI could be mechanically and chemically exfoliated into thin sheets. According to this hypothesis, Bojdys and co-workers acquired a thin nanosheet from the PTI/Br by Scotch-tape exfoliation (Fig. 4e).[79] The thickness of the obtained nanosheet was determined by the AFM analysis, corresponding to the stacking of 10–100 layers. The PTI/Br could also be exfoliated by gas-phase metal potassium treatment. Once the K(PTI/Br) encountered water, K would react with water and generate H_2, which was released between the layers, thus promoting the exfoliation process. XRD and SAED patterns show that the obtained nanosheet are predominantly crystalline.

Overall, the ionothermal route is a facile, eco-friendly and powerful approach for the synthesis of CCNs. Moreover, the CCNs synthesized by ionothermal approach generally contained alkali metal ions and exhibited distinct properties and high activity for photocatalysis. However, the underlying formation mechanism of CCNs in molten salt is still not well understood.

4.3. Solvothermal method

Considering the easy loss of nitrogen during high-temperature synthesis, the solvothermal route, which was generally performed at intermediate temperatures, had gained much attention.[80–88] Bai and co-workers synthesized graphite-like CCN by reacting CCl_4 with NH_4Cl at 400 °C through the solvothermal route.[81] From the sharp peak of the XRD pattern (Fig. 5a), which was consistent with the theoretical results, it could be confirmed that the sample was graphite-like C_3N_4 with high crystallinity, which was further proved by the clear diffraction spots (Fig. 5b) in the SAED pattern. Zhu and co-workers reported a solvothermal route for the synthesis of CCN using the $C_3N_3Cl_3$ and Li_3N as precursors in benzene at 355 °C for 12 h.[82] The high intensity peaks of α-C_3N_4 and β-C_3N_4 appeared in the XRD pattern (Fig. 5c), indicating that the CCN consisted mainly of crystalline a-C_3N_4 and β-C_3N_4. The EELS (Fig. 5d) revealed that the carbon atom was mainly sp^3 bonded in the sample, further confirming the formation of α-C_3N_4 and β-C_3N_4 crystalline phases. Moreover, benzene could effectively dissolve and disperse $C_3N_3Cl_3$ and activate Li_3N, which facilitated the crystallization of CN under supercritical conditions. In the same year, Xie and co-workers prepared well-crystallized graphitic CN *via* a benzene-thermal method by reacting $C_3N_3Cl_3$ with $NaNH_2$ at 180–220 °C for 8–12 h.[83] The sharp (002) peak in the XRD pattern (Fig. 5e) proved the good crystallinity of CN. Moreover, the XPS result further confirmed that the atomic N/C ratio was in good agreement with the C_3N_4 stoichiometry. The SAED results (Fig. 5f) indicate that the diffraction ring can be indexed to (002) reflection, which corresponds to the graphitic structure of polycrystalline feature, proving the successful preparation of CCN. Cao and co-workers developed an acetonitrile-promoted solvothermal route for the synthesis of CCN with cyano and carboxyl groups.[88]

In summary, the solvothermal method is a convenient way for the large-scale synthesis of novel nanostructured CCNs.

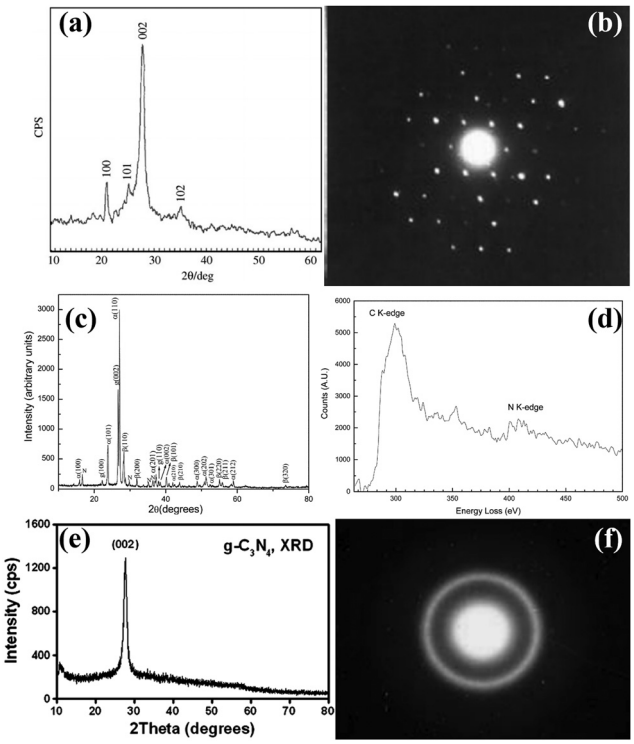

Fig. 5 (a) XRD pattern of g-C_3N_4 nanocrystals. (b) The SAED of g-C_3N_4 single crystal. Reproduced with permission.[81] Copyright 2003, Elsevier. (c) XRD pattern of the CCN. (d) EELS spectrum of C and N K-edges of CCN. Reproduced with permission.[82] Copyright 2003, The Royal Society of Chemistry. (e) XRD pattern of g-C_3N_4 nanocrystallites. (f) The SAED pattern of g-C_3N_4 nanocrystallites. Reproduced with permission.[83] Copyright 2003, Elsevier.

Note that the solvothermal methods sometimes require high temperture and harsh chemicals, which could be further optimized. In addition, the synthesis mechanism of this novel nanostructured CCN prepared by solvothermal method deserves further investigation.

4.4. Microwave (MW)-assisted heating synthesis

Although there are numerous publications on the synthesis of CCNs, the synthetic methods usually required high temperature and long reaction time (several hours). Therefore, an effective synthetic strategy for the rapid synthesis of CCN is highly desirable. Xue and co-workers developed a rapid synthesis strategy known as ''microwave-assisted heating synthesis'', enabling the preparation of CCN within minutes.[89] In this approach, CuO was utilized as the microwave (MW) absorber, which intensively absorbed MW and induced rapid heating within few minutes. Evidently, the peak intensities of the obtained product (Fig. 6a) were higher than those of the pristine CN, confirming the enhanced crystallinity, which was further confirmed by the HRTEM image. Very distinct lattice fringes with a distance of 0.33 nm, corresponding to (002) facets, were observed (Fig. 6b). It is well known that a supramolecular preorganization is a self-templating approach where a preorganized network formed by hydrogen bonding, ensuring the perfect alignment of CN during the polymerization process. Motivated by

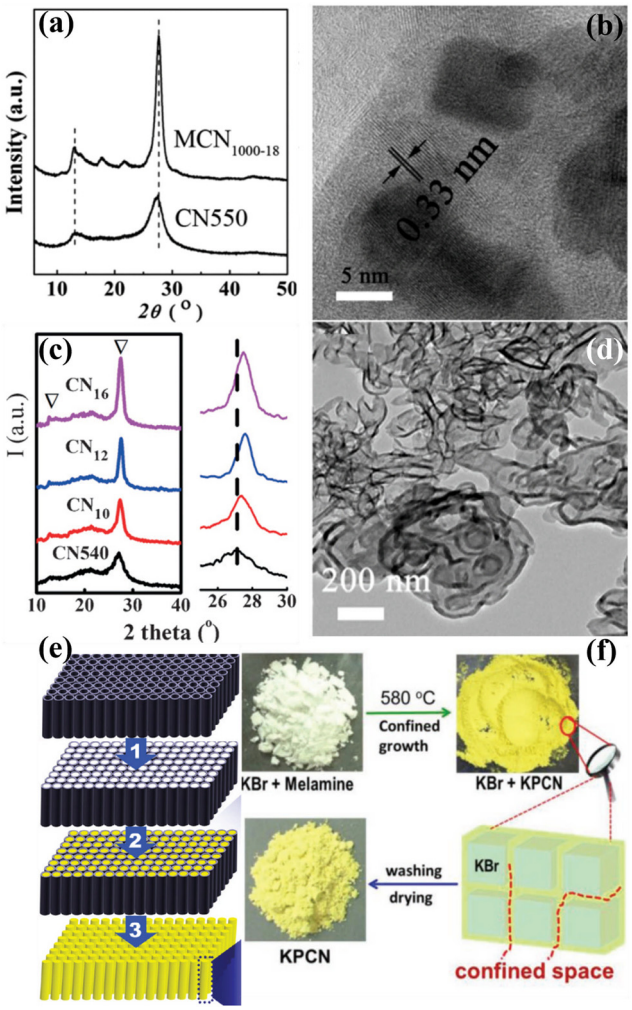

Fig. 6 (a) XRD patterns of the $MCN_{1000\text{-}18}$ and CN550. (b) HRTEM image of the $MCN_{1000\text{-}18}$. Reproduced with permission.[89] Copyright 2014, The Royal Society of Chemistry. (c) XRD patterns of CN_t (t = 10, 12, and 16) and CN540. (d) TEM image of CN_{16}.[90] Copyright 2016, Wiley-VCH. (e) Schematic representation of the synthesis of CCN nanorods through nanoconfinement method. Reproduced with permission.[92] Copyright 2011, American Chemical Society. (f) Schematic diagram of the preparation of KPCN from KBr confined growth. Reproduced with permission.[95] Copyright 2019, Wiley-VCH.

this idea, Yuan and co-workers designed a rapid and facile strategy for the preparation of highly crystalline CN with decreased structural defects by combining the microwave-assisted thermolysis strategy with a supramolecular preorganization approach.[90] In contrast to the broad and weak XRD pattern of the CN540 sample, an intense and narrow diffraction peak was observed in CN_{10}, suggesting the improved crystallinity (Fig. 6c). Moreover, the peak at 27.5° was moved to a higher angle as the reaction time was extended (Fig. 6c, right), indicating a decrease of the interlayer distance, confirming that the polycondensation was enhanced by the microwave-assisted thermolysis route. More importantly, the lifetime of the charge carriers in CN_{10} was reduced due to the rapid charge transfer, further confirming the improved crystallinity (Fig. 6d). Overall, the MW-assisted heating route is a facile, rapid, and robust approach for the synthesis of CCNs. It has several advantages. First of all, it is a time and energy saving method. The preparation process can be shortened to 15 minutes. Secondly, this is a general approach which can be applied to other nitrogen-rich organic precursors.

For comparison, the advantages and disadvantages of different methods for synthesizing CCNs are summarized in Table 1.

4.5. Other methods

Yin *et al.* developed a distinct method to synthesize the single-crystal β-C_3N_4 nanorods through mechano-chemical reaction and subsequent thermal annealing under NH_3 gas flow.[91] Li and co-workers synthesized high crystalline CN nanorods through a nanofabrication strategy which could overcome the kinetic restrictions of bulk polycondensation (Fig. 6e).[92] The nanoconfinement strategy was achieved by thermal polymerization of cyanamide within the nanochannels of anodic alumni oxide (AAO) template, resulting in improved orientation and crystallinity. Zhang and co-workers developed a simple approach to prepare CCN through protonating specific intermediates during the thermal condensation process, which could promote the solid-state polymerization kinetics.[93] Hu and co-workers prepared CCN nanosheets through an alternating cooling and heating strategy.[94] Su and co-workers fabricated K cations intercalated CCN *via* a salt-template-confined growth route (Fig. 6f).[95] The solid KBr could act as a solid template and provide a confined space, thus leading to the confined growth of CCN within the KBr crystal to achieve the crystalline structure. Similarly, KCl and NaCl were used as a template to provide a confined space between the salt crystals to effectively guide the growth of CCN.[96,97] Huang and co-workers proposed a new approach of engineering hydrogen bonding interactions within the CN framework of melons (doping-induced) to promote the crystallinity of CN.[98] This conception was realized by the removal of some amino groups and the use of co-doped B and F atoms to connect the melons *via* sodium fluoroborate-assisted heat polymerization. Moreover, the CCN quantum dots could be prepared by a solid-phase reaction strategy[99] or "dry hydrothermal" method.[100] The ground mixture of urea and sodium citrate was thermally treated in an autoclave at 180 °C for 1 h or 140 °C for 3 h to synthesize CCN quantum dots.

Table 1 The advantages and disadvantages of different synthesis methods

Method	Advantages	Disadvantages
HT–HP	Adjustable carbon/nitrogen ratio	Expensive equipment; high temperature; high pressure
Ionothermal (molten salt)	Cheap equipment; easy operation; large-scale preparation	Complicated procedure for washing samples
Solvothermal	Cheap equipment; easy operation	Harsh feedstock; high pressure
Microwave (MW)-assisted heating	Large-scale preparation; easy operation; time and energy saving	Uncontrollable temperature

4.6. Characterization of CCNs

Generally, the conventional characterization methods for the crystal structure of CCNs are XRD and HRTEM analyses. Due to the different building blocks of CNNs, the XRD patterns could distinguish different crystal structure of CCNs. The (100) peak of PTI-based CCN is located at ~12°, corresponding to the in-plane pores. While the (100) peak of PHI-based CCN is located at ~8.1°, which corresponds to a larger in-plane spacing. Moreover, as revealed by the HRTEM images, the lattice fringes of PTI-based CCN is around 0.73 nm, while the lattice spacing of PHI-based CCN is approximately 1.1 nm. Overall, the XRD and HRTEM analyses could only provide the average structural information. In recent years, solid-state NMR spectroscopy[101] and neutron diffraction[102] have provided the structure information of local and light element of CCNs. However, real-space details and atomic resolution imaging of the local configuration of CCNs is still challenging. Very recently, integrated differential phase contrast scanning transmission electron microscopy (iDPC-STEM) is an emerging phase imaging technique based on center of mass shift of the convergent beam electron diffraction patterns by utilizing the four-quadrant detector.[103] Through analyzing the scattered electrons, the x and y components of offset vectors of DPC image were obtained.[104] Through two-dimensional integration, the iDPC image was obtained, enabling us to realize the low dose imageing of the light element beam-sensitive materials with atomic resolution and high signal-to-noise ratio.[105] Therefore, the atomic-resolution imaging of the true spatial structure of CCNs was directly visualized by the iDPC-STEM.[106–108] For example, He and co-workers revealed the atomic structure (including the light elements) and atomic electric field of the PTI crystal with the low dose imaging by the DPC-STEM technique.[107] As displayed in the iDPC images (Fig. 7a and b), the six triazine units with highly ordered atomic structures were interconnected to build the 2D honeycomb network and chloride ions occupied the central triangular pore. Moreover, the location of Li and H atoms with three configurations could be determined by the iDPC-STEM and corresponding simulated images (Fig. 7c–f). The H atoms were surrounded by bridging N atoms and the lithium ions were used to balance the charge of bridged imide groups. Furthermore, the atomic coupling electric field between the Li and neighboring atoms was directly visualized by the atomic electric field imaging (Fig. 7g and h). Meanwhile, the DFT calculations confirmed that the Li–N ionic bonds were formed, which not only extended the π-conjugated electronic structure, but also created an additional charge transfer channel to facilitate in-plane charge migration (Fig. 7i). Therefore, the charge migration route was schematically presented in Fig. 7i. Besides, the Li ions could be intercalated into the layers, which also confirmed by the NMR and XPS results.

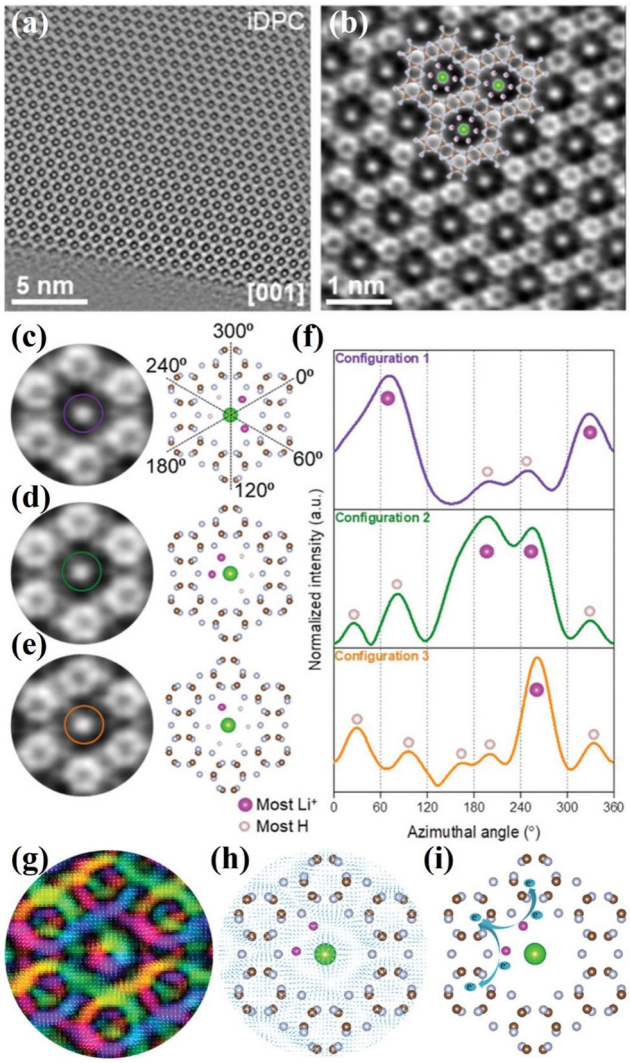

Fig. 7 (a) iDPC image of PTI along the [001] zone axis. (b) Enlarged iDPC image. (c)–(e) Three Li/H configurations in the intralayer cavities detected in iDPC and the corresponding atomic structure models. (f) Intensity profiles following the defined circles in (c)–(e). Dashed lines in (c) guide the azimuthal angles of intensity profile in (f). (g) Magnified color map with the arrow vector. (h) The arrow vector map overlapped with the atomic structure of PTI. (i) Schematic diagram of the migration of photoexcited electrons between lithium ions and the triazine units. Reproduced with permission.[107] Copyright 2021, Wiley-VCH.

5. Design of CCNs-based photocatalysts

5.1. Nanostructure design

Considering that the photocatalytic process is an interfacial reaction, the photocatalytic activity largely depends on the shape, size and nanostructure of CCNs. The nanostructure of CCNs can be designed to obtain high specific surface area, enhanced electron transport property, reduced migration distance and abundant surface active sites, all of which are beneficial to improve the photocatalytic activity. Until now, various nanostructures of CCNs such as nanosheets, nanotubes, nanorods and nanofibers have been prepared by many ingenious approaches. The following is a detailed description of various strategies for designing nanostructures of CCNs.

5.1.1. Exfoliation of bulk CCNs. Recently, CCNs nanosheet has attracted great attention because of their abundant exposed active sites due to the large specific surface area, and low electron–hole pair recombination rate owing to the short charge migration

distance. Motivated by the graphene exfoliated from graphite, graphite-like bulk CCNs have the potential to be exfoliated into 2D CCNs nanosheets, especially ultrathin 2D CCNs nanosheets. CCNs nanosheets could be acquired through different approaches, including ultrasonication-assisted liquid exfoliation, framework charging, spontaneous dissolution, thermal oxidation exfoliation, and alkaline metal ion intercalation.[65,79,94,109–114] Inspired by the advances in graphene oxide (GO), CCNs nanosheets have been fabricated through the liquid exfoliation strategy. For example, Lotsch and co-workers obtained CCN nanosheets from bulk PTI by sonication-assisted liquid-exfoliation in water.[65] Atomic force microscopy (AFM) image shows that the obtained triazine-based CCN nanosheets had a height of 1–2 nm (Fig. 8a). TEM image further confirms that the high crystallinity remained unchanged after exfoliation (Fig. 8b). Compared with bulk PTI, the PTI nanosheets exhibited significantly enhanced (by a factor of 18) photocatalytic performance under visible-light irradiation due to their larger specific surface area and more active sites. Although the above study demonstrated that the triazine-based CCNs had photocatalytic hydrogen production activity, the tri-*s*-triazine-based CCNs is expected to have higher photocatalytic activity because of the extended π-system, which facilitated light-harvesting and charge carriers transportation.[115] Hence, Wang and co-workers prepared the heptazine-based CCN nanosheets by liquid-exfoliation through an ultrasonic approach in isopropanol (IPA).[112] The XRD pattern of the CCN nanosheets was similar with that of the bulk CCN, suggesting that the crystal structure was preserved after exfoliation. As revealed by the TEM, the as obtained CCN nanosheets possessed a silk veil-like shape, which implied the successful exfoliation of bulk CCN (Fig. 8c). The thickness of the obtained nanosheets was between 3 and 4 nm, which corresponded to a stacking of ten layers (Fig. 8d). The thickness of the CCN nanosheets was further evaluated by the AFM and determined to be 3.6 nm. In addition, the photocurrent of the CCN nanosheets was significantly enhanced compared with the bulk CCN, confirming the improved charge separation. The PL spectra of the CCN nanosheets further demonstrated this, as a much weaker PL intensity was observed after exfoliation, which corresponded to improved separation of electron and holes. As a result, the heptazine-based CCN nanosheets showed significantly enhanced photocatalytic hydrogen generation activity under visible light irradiation compared to bulk CCN, mainly due to their high crystallinity, high charge carrier separation and transfer rate, and enlarged specific surface area.

McMillan and co-workers demonstrated that the 3D bulk PTI-based CCN was delaminated into a defect-free, hexagonal two-dimensional nanosheets by a thermodynamically driven dissolution process without any chemical or physical intervention (Fig. 8e).[109] The bulk CCN spontaneously dissolved in select polar aprotic solvents due to the free energy gain from the solvent coordination effect. Interestingly, the obtained nanosheet are stacked in several layers rather than monolayer, suggesting that the interlayer interactions are energetically comparable to those between the solvent and nanosheet surfaces. Mattevi and co-workers reported a framework charging route for

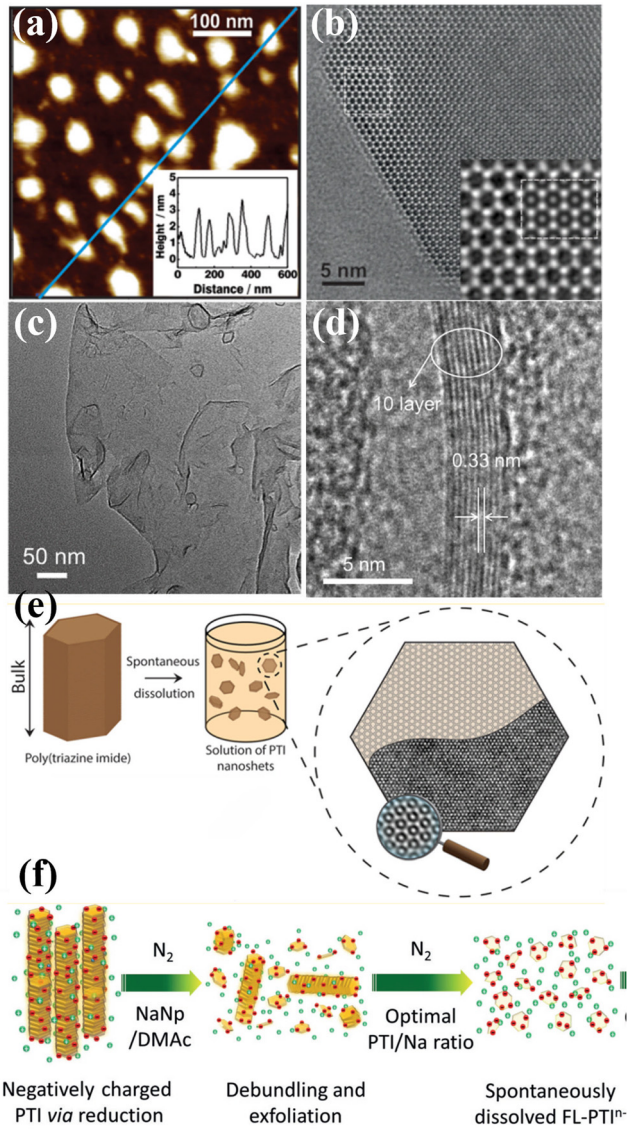

Fig. 8 (a) AFM image of the PTI nanosheets and corresponding height image (inset). (b) HRTEM image of PTI nanosheet and simulation (inset). Reproduced with permission.[65] Copyright 2014, American Chemical Society. (c) TEM image of the CCN nanosheets. (d) HRTEM image of CCN nanosheets. Reproduced with permission.[112] Copyright 2017, Wiley-VCH. (e) Schematic illustration of the PTI nanosheet prepared by spontaneous dissolution. Reproduced with permission.[109] Copyright 2017, American Chemical Society. (f) Schematic illustration of charging and exfoliation of PTI. Reproduced with permission.[110] Copyright 2018, Wiley-VCH.

the fast and high yield preparation of PTI nanosheets through sodium naphthalide (NaNp)/DMAc reduction (Fig. 8f).[110] NaNp was used as an electron charge transfer agent, while DMAc was expected to be an excellent room-temperature solvent for anionic monolayer/few-layer CCNs. The negative charge from NaNp could be rapidly transferred to PTI, leading to short-range Coulombic repulsion, which resulted in the exfoliation of PTI into solvated few-layer sheets. Agrawal and co-workers prepared monolayer PTI-based CCN nanosheets in anhydrous dimethylacetamide (DMAc) by a simple solvent exfoliation route.[111] The DMAc played an

essential role in exfoliation due to the strong interaction of carbonyl oxygen of DMAc with Li^+, which weakened the interlayer interaction.

Despite there are numerous research publications related to the liquid exfoliation of bulk CCN, this process requires a long sonication processing time (10–16 h). To address these bottlenecks concerning the exfoliation of bulk CCN, thermal exfoliation has emerged as a fast and effective strategy.[113,116] For example, Zhang and co-workers proposed a simple but effective strategy for the high-yield synthesis of CCN nanosheets with a specific surface area of up to 34 $m^2 g^{-1}$ by two-step calcination.[113] The structure of the nanosheet was confirmed by the TEM image, and a clear crystal lattice with a distance of 3.30 Å is observed in the HRTEM image, indicating its high crystallinity. The electrochemical impedance spectra (EIS) analysis indicates that the electron-transfer resistance of CCN nanosheets was lower than that of bulk CN. Also, an obvious enhancement of photocurrent was observed for CCN nanosheets compared with bulk CN, which indicated the effective separation of charge carriers and enhanced photoinduced charge mobility in the CCN nanosheets. Moreover, the TRPL spectra shows a prolonged lifetime of charge carriers, indicating a higher electron mobility. Thus, the prepared CCN nanosheets showed outstanding photocatalytic performance, with a hydrogen generation rate of 9577.6 μmol $h^{-1} g^{-1}$, 15.5 times that of bulk CN.

In summary, the preparation of CCN nanosheets has been achieved by various exfoliation strategies. The superiority of the CCN nanosheets could be attributed to the increased specific surface area, enhanced electron transfer capability, prolonged lifetime of charge carriers, and improved charge separation efficiency.

5.1.2. Hard-template approach. The hard-template strategy, which uses inorganic or organic matrices as templates, is a controllable and effective approach for fabricating nanostructured CCN materials.[117–120] Chen and co-workers developed a template-assisted approach to prepare highly crystalline g-C_3N_4 nanosheets by adopting nickel foam as the hard template and dicyandiamide as the precursor (Fig. 9a).[117] The Ni-foam was not only used as a template for depositing CCN nanosheets to prevent stacking, but also as a catalyst to boost the polymerization and crystallization of g-C_3N_4, resulting in CN nanosheets with high crystallinity. HRTEM image shows well-defined lattice fringe with a distance of 0.33 nm, suggesting better crystallization under Ni catalysis (Fig. 9b). The as-prepared CCN nanosheets had a larger specific surface area of 39.24 $m^2 g^{-1}$, confirmed by the nitrogen adsorption–desorption isotherms, which was much larger than that of CN (7.73 $m^2 g^{-1}$). The CCN nanosheets showed superior photocatalytic activity for H_2 evolution, which was attributed to the high crystallinity, large specific surface area and efficient separation of photoinduced charge carriers. Takanabe and co-workers reported using spherical KCC-1 silica particles as a support (without its removal) to produce dendritic tip CCN by combining molten salt with supermolecule strategy (Fig. 9c and d).[118] CCN fibers with a thickness of 20–30 nm could project outward from the sphere and assemble in an organized manner, resulting in an uniformly sized nanosphere with dendritic fibers. Owning to the high crystallinity, highly dispersed cocatalysts and slow charge carrier recombination rate, the Pt/CN/KCC-1 showed a remarkable apparent quantum efficiency (AQE) of 22.1 ± 3% in the solar hydrogen evolution reaction at 400 nm.

In addition, mesoporous photocatalysts can be designed to improve the photocatalytic performance by increasing the specific surface and abundant active sites, as well as promoting the separation of photogenerated carriers. Recently, Yu and co-workers fabricated highly ordered and porous CCN through a one-step template-mediated strategy, that is, a bifunctional $NaHCO_3$ template-mediated approach.[119] Specifically, $NaHCO_3$ served as a gaseous template to promote the creation of the porous structures, while the resulting Na_2CO_3 could act as high-temperature solvent to facilitate the crystallization of porous CCN. Besides the porous structure and high crystallinity, the cyano groups were also introduced to the surface of porous CCN, which could serve as effective active sites for H_2 generation. As a result, the specific surface area of the porous CCN could be up to 15.34 $m^2 g^{-1}$, which was 3.5 times larger than that of bulk CN. Moreover, the clear lattice fringe with a distance of 0.32 nm was observed in the HRTEM image, confirming its high crystallinity. Owning to the great crystallinity, cyano-group defects and porous structures, the porous CCN exhibited a remarkably increased H_2 evolution rate, which was more than two times higher than that of bulk CN.

In the process of preparing CCN by salt-assisted synthesis strategy, the salt could be used as a template. Zou and co-workers fabricated an intercalated CCN nanotube through the molten salt route.[61] In general, these salts could be used as templates as their crystals have cubic morphology. Before the temperature reached the melting point of the mixed salt, thermal polymerization had occurred, and the polymerization intermediate had grown on the interface of the cubic chloride crystals, thus forming the nanotubes. By intercalating the alkali metal ions into the layers of CN, the migration and separation of photoinduced carriers was dramatically improved. Accordingly, the intercalated CCN nanotubes showed high photocatalytic hydrogen production activity, reaching 0.346 mmol h^{-1} within the first hour, 34.6 times higher than that of the bulk CN. Wang and co-workers fabricated the CCN nanosheets by a solid-salt-assisted growth strategy (Fig. 9e).[96] The solid salt acted as a structure-directing template to steer the orderly growth of CCN within the restricted space of the KCl crystals. Therefore, the exfoliation of bulk CCN was achieved due to the confinement effect of salt and the interaction of K^+ ions. As expected, the CCN nanosheets exhibited significantly improved photocatalytic activity compared with bulk CN. This improved activity could be ascribed to the high crystallinity and shortened interlayer distance, which could improve the light harvesting capability and boost the transfer of photoexcited carriers. Quan and co-workers synthesized (3D) branched CCN nanoneedles by combining a post-synthesis ionothermal approach with a quenching method.[121] The melted eutectic salts were used as an induction reagent to enhance the crystallinity and created 3D structures. Interestingly, the prepared nanoneedle with sharp curvature could evoke a nanoscale lightning rod-like effect to accelerate directional charge transfer, thus suppressing the

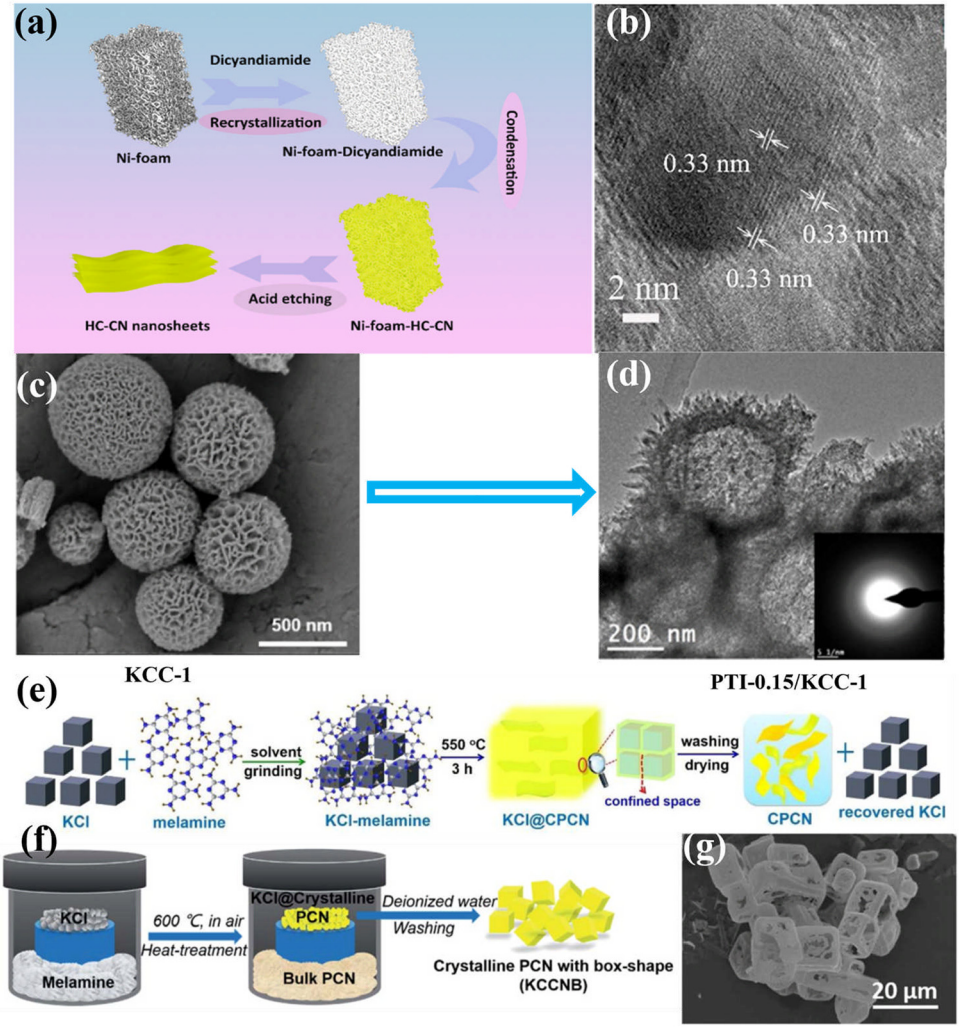

Fig. 9 (a) Schematic diagram of the fabrication of HC–CN photocatalyst. (b) HRTEM image of HC–CN. Reproduced with permission.[117] Copyright 2018, American Chemical Society. (c) SEM image of KCC-1. (d) TEM image of PTI-0.15/KCC-1. Reproduced with permission.[118] Copyright 2015, American Chemical Society. (e) Schematic diagram of the synthesis of CCN nanosheet by the solid salt confinement method. Reproduced with permission.[96] Copyright 2019, Elsevier. (f) Schematic diagram of the vapor-deposition strategy. (g) SEM image of KCCNB-30.[122] Copyright 2020, Royal Society of Chemistry.

recombination of photoexcited charge carriers. As expected, the 3D branched CCN nanoneedles showed outstanding photocatalytic activity for both H_2 generation (0.27 mmol h^{-1}) and H_2O_2 production (0.33 mmol h^{-1}), which was 85 and 23 times than that of the pristine CN, respectively. Shu and co-workers fabricated K^+ doped heptazine-based CCN with box-shape through vapor-deposition approach using KCl as a template (Fig. 9f).[122] The obtained K^+ doped CCN box had a diameter of *ca.* 10 μm, with a wall thickness of several hundred nanometers, which was confirmed by the SEM image (Fig. 9g). Due to the special box shape, the incident visible light could be reflected and absorbed multiple times, thus improving the light utilization. As a result, the K^+ doped CCN showed an improved photocatalytic H_2 generation performance, which was 33 times than that of bulk CN. This enhanced performance could be ascribed to the improved light absorption in the box shape, and the effective charge separation and transfer due to the doping of K and high crystallinity.

5.1.3. Supramolecular assembly route. In contrast to the hard template preparation technique described above, the supramolecular assembly route is a self-templating approach that forms stable aggregates with well-organized morphology and architecture through noncovalent interactions with no external template. Recently, the supramolecular strategy has emerged as an attractive approach to tune the morphological, optical, and electronic properties of CCNs.[123–125] A case in point, Fang and co-workers fabricated highly crystalline holey g-C_3N_4 nanosheets by combining hydrothermal pretreatment and microwave-assisted heating strategy.[123] The first hydrothermal process was to form melamine-cyanaurate complex (MCA) to prepare thin nanosheets with micro/mesoporous structure, while the microwave polymerization process could improve the crystallinity. As a consequence, the CCN nanosheets displayed a much larger specific surface area (*ca.* 31.64 m^2 g^{-1}) than that of the bulk CN (*ca.* 6.84 m^2 g^{-1}). Also, the SAED image confirms the increased crystallinity, which

showsd a bright diffraction ring. Benefitting from the high crystallinity, improved visible absorption utilization and increased surface active sites, the as-obtained sample displayed a relatively high photocatalytic performance. Zhu and co-workers reported a bottom-up supramolecular self-assembly approach for the synthesis of three-dimensional porous CCN nanosheet (Fig. 10a).[124] The clear lattice fringes appeared in the HRTEM image, indicating the high crystallinity of 3D nanosheet (Fig. 10b). The thickness of the nanosheet confirmed by the AFM image (Fig. 10c) was about 2.3 nm, which corresponded to the stacking of 5 layers. Moreover, the specific surface area of 3D CCN nanosheets was significantly increased to 130.00 $m^2 g^{-1}$ (Fig. 10d), providing more active sites and enhancing the light absorption. Therefore, owning to the open-framework of the 3D porous interconnection and the fast charge carrier transport, the 3D CCN nanosheets achieved efficient overall water splitting (OWS) performance under visible light with H_2 and O_2 generation rates of 101.4 and 49.1 μmol g^{-1} h^{-1}, respectively (Fig. 10e).

5.1.4. Other routes. Sun and co-workers developed an alternated cooling and heating treatment method for the rapid fabrication of highly crystalline few-layered CN nanosheets.[94] The obtained mesoporous ultrathin nanosheets showed high crystallinity, increased large surface area (88.59 $m^2 g^{-1}$), narrowed bandgap and improved electron transfer capacity. As a consequence, the CCN nanosheets showed a significant enhancement of photocatalytic performance.

To sum up, nanostructure design is one of the promising strategies to modulate the physical and chemical features of CCNs. Various morphologies of CCN from 1D to 2D, 3D nanoarchitectures were prepared by different synthesis

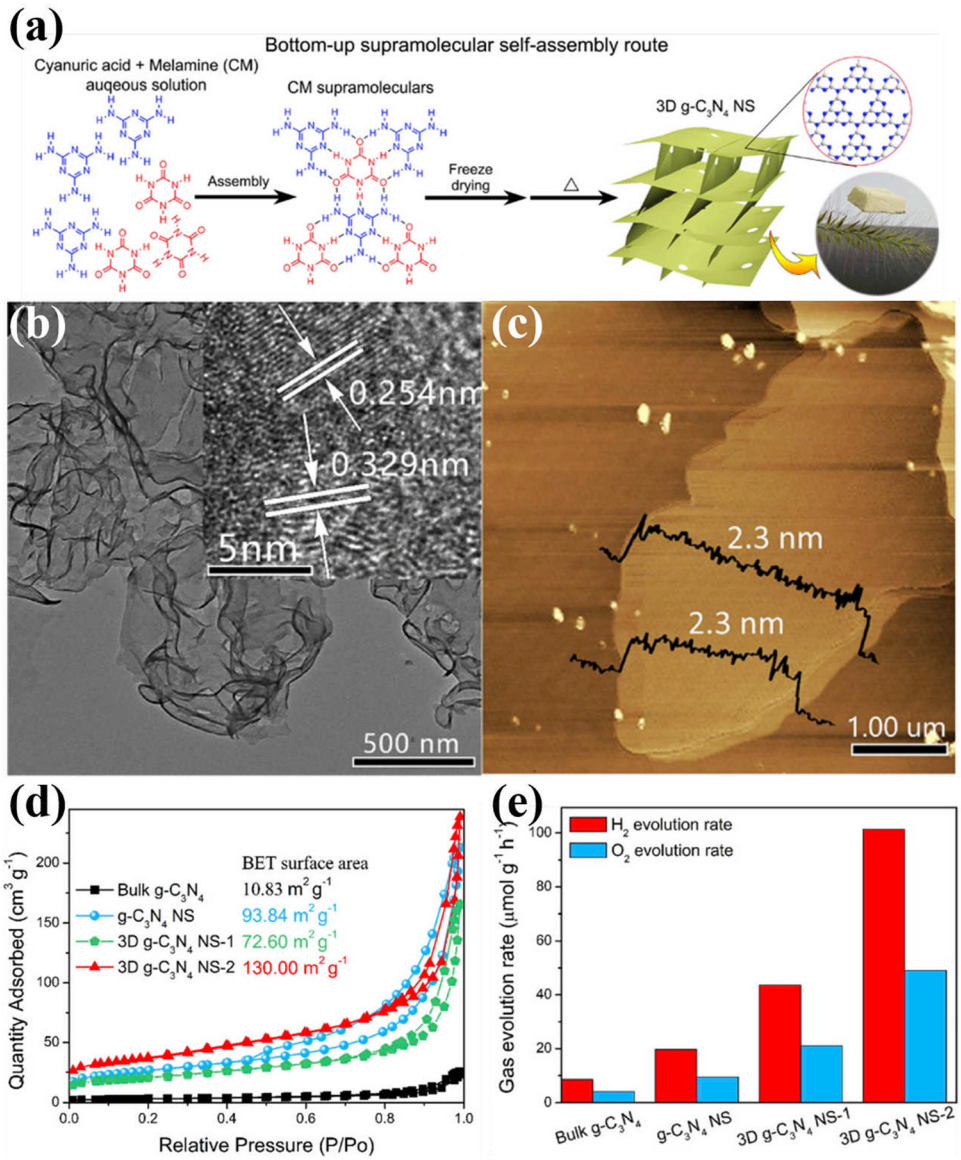

Fig. 10 (a) Schematic diagram of the fabrication of 3D g-C_3N_4 NS through the bottom-up supramolecular self-assembly strategy. (b) TEM image (HRTEM image inset) and (c) AFM image of 3D g-C_3N_4 NS-2. (d) N_2 adsorption–desorption isotherms of the samples. (e) Photocatalytic OWS activity over bulk g-C_3N_4, g-C_3N_4 NS, and 3D g-C_3N_4 NS. Reproduced with permission.[124] Copyright 2019, Elsevier.

methods. These nanostructured CCNs offer great advantages in terms of charge transfer, light absorption, and abundant active sites. For CCN with hollow structure, improved light absorption was achieved, which could improve the light utilization. In addition, 3D nanostructures of CCN have a large specific surface area which provided an additional pathway for electron transport. More importantly, combining supramolecular self-assembly strategies with solvothermal methods is highly desirable in the design and development of nanostructured CCNs.

5.2. Molecular structure engineering

5.2.1. Elemental doping of CCNs. Recently, numerous studies have shown that elemental doping is a feasible approach to regulate the electronic band structure of CCNs. Generally, there are two predominant types of element doping based on the type of impurities, namely, non-metal doping and metal doping. More specifically, the non-metal doping preferentially replaced the C or N atom, thus affecting the positions of conduction band and valence band,[126] while the metal doping is realized by inserting ions into the cavity or interlayer, thus creating both in-plane and interlayer charge transport channels.[127] For example, Dai and co-workers fabricated highly crystalline sulfur-doped CN through the self-assembly of melamine and tri-thiocyanuric acid, followed by calcination.[128] As a result of S doping, the bandgap was reduced, thereby expanding the light absorption range. The S doped CCN exhibited an excellent H_2 production rate of 1511.2 μmol g^{-1} h^{-1}, which was about 11 times higher than that of the pristine CN. Such an enhanced performance could be ascribed to the increased specific surface, high crystallinity, efficient charge separation and transfer rate. Although the light absorption was enhanced, the CCN with near-infrared activity was still challenging but highly desirable. Therefore, Li and co-workers developed O-doped CCN (MC-CN) with near-infrared response through a molten salt strategy using carbohydrazide as the precursor.[129] Compared with CN, the absorption edge of MC-CN was significantly red-shifted and extended to the near-infrared region, attributed to the O doping, while the absorption shoulder assigned to the π–π* transition exhibited higher intensity, indicating the high crystallinity (Fig. 11a). Thus, the bandbap of MC-CN was determined to be 1.42 eV (inset in Fig. 11a). Meanwhile, the MC-CN exhibited a hierarchical nanoflower morphology consisting of nanorods, enhancing the light absorption and providing more active sites (Fig. 11b). Moreover, the DFT calculations indicates the generation of internal electric field because of the O doping, which boosted the charge separation and transport. Owning to the improved optical absorption and charge migration, the MC-CN presented remarkably enhanced photocatalytic H_2 evolution activity under visible-light irradiation and achieved a photocatalytic activity even in the near-infrared region (Fig. 11c). In addition to nonmetal doping, metal doping was also designed by Zhong and co-workers.[130] The Zn doped CCNs was fabricated by a two-step thermal polycondensation method in a molten salts bath. The diffraction peaks of Zn-CCN in the XRD pattern became lankier and sharper, indicating that the Zn doping did not change its high crystallinity, which was further confirmed by the clear lattice fringes in the HRTEM image. The XPS analysis demonstrated the successful incorporation of Zn doping. Moreover, the doping of Zn enhanced the electron delocalization and accelerated the charge transfer. As a result, the Zn-CCN showed superior hydrogen production activity (*ca.* 75 μmol h^{-1}), which was 41 times higher than that of pristine CN (1.8 μmol h^{-1}). Apart from transition metal doping, alkali metal doping was also reported. In particular, Su and co-workers designed a solid-template induced growth strategy to prepare highly crystalline K-cation intercalated CCN (KPCN).[95] XRD and XPS analysis provided evidence of K ions insertion into the melon chains or layers of PCN. The doping of K could narrow the bandgap and thereby improved the light absorption properties of KPCN (Fig. 11d). Besides, HRTEM image shows clear lattice fringes, confirming the high crystallinity of KPCN (Fig. 11e). As expected, the KPCN exhibited significantly enhanced photocatalytic performance, 18 times higher than that of the bulk PCN. This improved photocatalytic performance could be ascribed to the high crystallinity and K doping, which promoted the separation and transfer of photoexcited carriers and inhibited recombination, thereby increasing the lifetime of the carriers. Very recently, Mi and co-workers proposed an n-type doping approach that replaced monovalent K^+ ions with divalent alkaline earth metal ions for visible and near-infrared photocatalytic H_2 evolution.[131] The n-type doping could dramatically enhance the electron densities and activate the n → π* transitions, leading to near-infrared light absorption (Fig. 11f). Moreover, the n-type doping not only improved the conductivity, but also regulated the effective mass of carriers as well as the valence band state, facilitating the charge carriers transport and separation. Benefiting from the efficient charge transport and separation, the as-synthesized Ca^{2+} doped crystalline K^+ implanted CN (CKCN) showed a remarkable AQE of 31.2% at 420 nm (Fig. 11g). Beyond single element doping, He and co-workers prepared C and K co-doped red polymeric carbon nitride (RPCN) through a salt-template approach.[132] The uniform and high doping of C and K could dramatically reduce the bandgap of CN (1.7 eV) and inhibited the recombination of photogenerated electrons and holes. As a consequence, the RPCN exhibited high near-infrared photocatalytic H_2 generation performance (140 μmol h^{-1} g^{-1}), with an AQE of up to 0.84% at 700 ± 10 nm. Sun and co-workers developed a K and S co-doped CCN for photoreforming of biomass coupled with CO_2 reduction through a salt-template-assisted incorporation approach.[133]

Besides heteroatom doping, self-doping has also been developed by recent works.[134–136] For example, our group developed an acetonitrile-promoted solvothermal route for the synthesis of CCN with cyano and carboxyl groups.[88] The high crystallinity was confirmed by the HRTEM image (Fig. 11h). The NMR studies revealed that the defects were most likely located at the structural terminations of the CCN framework (Fig. 11i). Moreover, the introduction of surface defects not only improved visible light absorption, but also increased CO_2 binding affinity and improved charge transfer and electron storage. Therefore, the as-prepared CCN with surface defects showed superior photocatalytic CO_2 reduction performance and selectivity in the gas phase. Wang and co-workers found that the CCN with defects achieved a better charge separation because of the built-in electric field.[134]

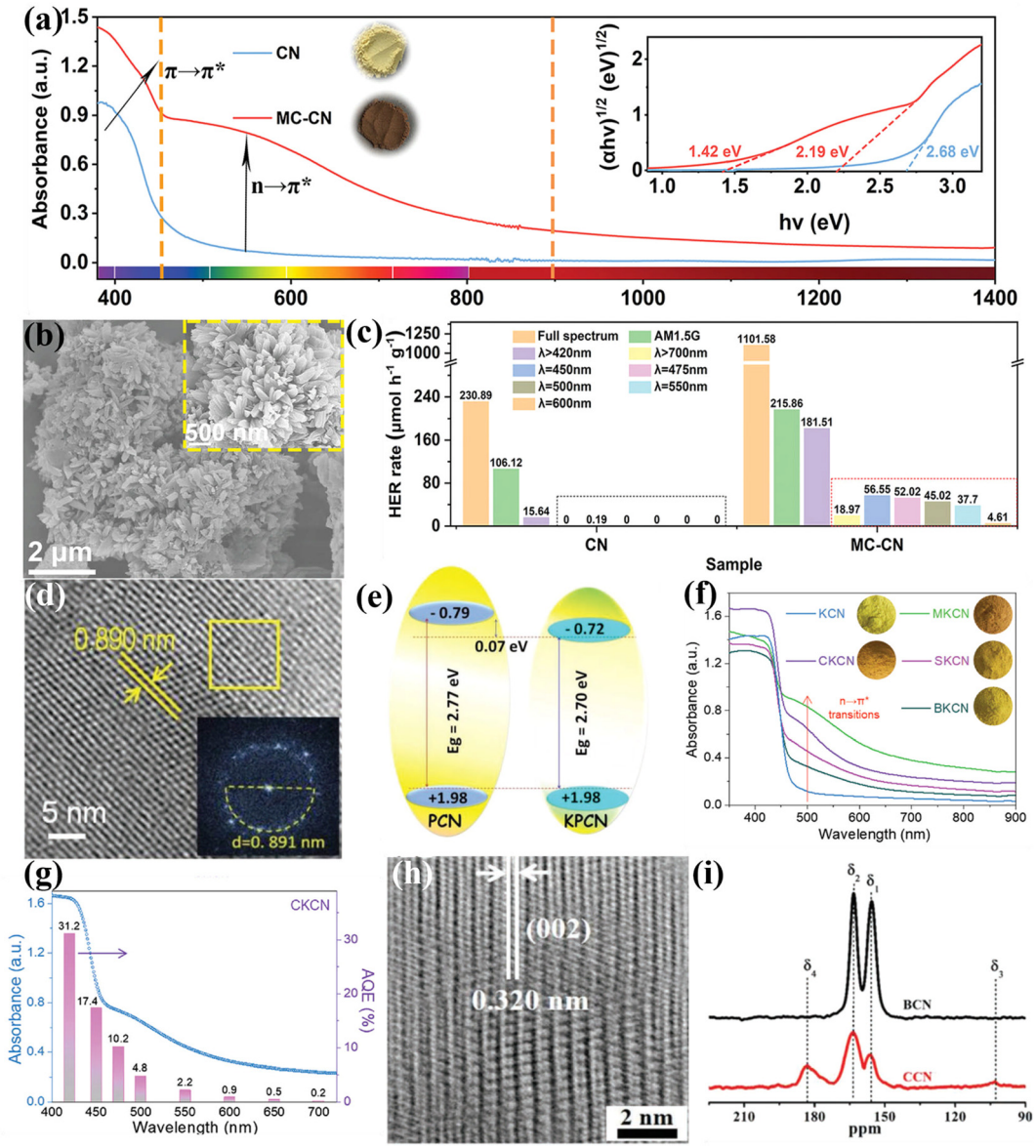

Fig. 11 (a) UV-vis diffuse reflectance spectra (DRS) of CN and MC-CN and the corresponding Kudelka–Munk plots (inset). (b) SEM and high magnification SEM images (inset) of MC-CN. (c) Wavelength dependence of the photocatalytic H_2 generation rate of CN and MC-CN. Reproduced with permission.[129] Copyright 2022, Wiley-VCH. (d) HRTEM image and FFT pattern (inset) of KPCN. (e) Schematic representation of the band structures of PCN and KPCN. Reproduced with permission.[95] Copyright 2019, Wiley-VCH. (f) UV-vis-NIR DRS spectra of KCN, MKCN, CKCN, SKCN, and BKCN samples. (g) Wavelength dependence of AQE of CKCN. Reproduced with permission.[131] Copyright 2022, Wiley-VCH. (h) HRTEM image of CCN. (i) ^{13}C NMR of BCN and CCN. Reproduced with permission.[88] Copyright 2019, Wiley-VCH.

In conclusion, elemental doping plays a key role in modulating the band structure of CCNs. In most cases, elemental doping not only narrowed the bandgap, but also improved the separation of charge carriers because of the built-in electric field, thereby improving the photocatalytic activity. Although many studies on heteroatom-doped CCNs have been successfully developed, there is still an urgent need to control the distribution and concentration of doping, such as gradient doping.

5.2.2. Molecular doping of CCNs. As a cross-linked conjugated polymer semiconductor, the photocatalytic activity of CN originates from the π-conjugated aromatic structure. However, the aromatic π-conjugated system of CN generally suffers from intrinsic drawbacks, such as insufficient absorption and utilization of sunlight and rapid recombination of charge carriers, which limit its potential applications. Hence, it is desirable to modulate the intrinsic π-conjugated system and electronic structure by delocalizing π electrons.[137–139] The molecular doping strategy, copolymerization of another similar aromatic structural unit with CN precursors during the polymerization process, is regarded as an essential approach for extending the π electrons conjugation of the aromatic system and tuning the band structure. A case in point, Takanabe and co-workers incorporated a 2,4,6-triaminopyrimidine (TAP) monomer into the conjugated CN structures by copolymerizing

melamine and TAP, combined with supramolecular preorganization and ionothermal methods (Fig. 12a).[140] The absorption edge of the sample was red-shifted to 700 nm (Fig. 12b and c) because of the introduction of pyrimidine moieties. Moreover, the PTI-0.13 exhibited a remarkably improved hydrogen evolution performance because of the improved high crystallinity and increased π-electron delocalization. Another representative research on molecular doping within the PHI framework was presented by Zhang and co-workers.[141] The PHI-based CCN (CN-OA-m) was synthesized by copolymerization of urea and oxamide in molten salts. As evidenced by the XRD pattern, the as-synthesized CN-OA-m exhibited larger interplanar stacking distance and shorter interlayer stacking distance compared to bulk CN, probably due to the well-condensed structure. The HRTEM image further confirms the decreased interlayer distance and high crystallinity (Fig. 12d). As a result of molecular doping, the absorption edge of CN-OA-m was moved to about 700 nm, which would contribute to the photocatalytic performance (Fig. 12e). Moreover, the EIS and photocurrent curve confirmed the improved charge transport, which could be ascribed to the molecular doping and high crystallinity. The CN-OA-m showed superior photoactivity, even irradiated with green LEDs (Fig. 12f), because of the enhanced optical absorption and improved exciton dissociation. Despite the enhanced visible light absorption, the potential of CB and VB was reduced and increased, respectively, which dramatically lowered the reduction and oxidation abilities. To overcome this limitation, the same group prepared a new allotrope of CN with internal heterostructures by copolymerization of aminotetrazole with adenine in NaCl/KCl molten salts.[142] Therefore, the excellent oxidation and reduction abilities were confirmed by valence band XPS and Mott–Schottky results, respectively (Fig. 12g). The charge distribution of the D–A structure was demonstrated by the large interplanar spacing of 1.65 nm ($d1 + d2$). Moreover, the efficient charge transport at the interface caused by the heterostructure was confirmed by the large photocurrent (Fig. 12h). Furthermore, the as-prepared sample showed excellent photo-redox activity due to the local donor–accepter (D–A) heterojunction which enhanced light absorption and promoted charge separation. The AQE measured at 420 nm was 9.6% using ethanol as the sacrificial agent. Although the efficient charge separation has been achieved within the photocatalyst, the interfacial electron transfer between the sacrificial electron donor and photocatalyst is an important but neglected factor. Therefore, Lotsch and co-workers designed surface covalently modified PHI with melamine as the terminal unit (Mel-PHI) to modulate the interface of electron donner and photocatalyst to improve the photocatalytic H_2 generation performance (Fig. 12i).[143] The successful surface functionalization was demonstrated by the solid-state NMR results. Moreover, the quantum–chemical calculations revealed that the terminal melamine was not surrounded by H_2O molecules, suggesting the hydrophobic properties (Fig. 12j). Meanwhile, the result also implied that the water and TEOA interacted well with both melamine and the adjacent heptazine moiety *via* hydrogen bonding (Fig. 12k). Thus, the established catalyst–solution interface could facilitate electron transfer from the sacrificial agent to adjacent exciton, suppressing the charge recombination. Benefiting from the modified electronic structure and improved interfacial interactions, the Mel-PHI exhibited a photocatalytic H_2 generation rate of up to 5570 μmol h^{-1} g^{-1}, superior to most other CNs photocatalysts.

Overall, molecular doping not only modulated the bandgap of CCNs, but also delocalized the π electrons. Doping with a very small amounts of organic additives could significantly modulate the bandgap and electronic structures. However, the doping sites of organic monomer were still obscured, which need further investigation.

5.2.3. Defects modification. In addition to molecular doping, the introduction of defects such as vacancies in the CCN framework has been shown to significantly enhance the photocatalytic performance due to it improves charge separation, provides more active sites and enhanced light absorption ability. For example, Li and co-workers proposed the preparation of CCN (CN-NVs-CTe) with rich nitrogen vacancies *via* alkali-assisted salt molten method.[144] The HRTEM image shows clear lattice fringes of CN-NVs-CTe, indicating the high crystallinity. The existence of nitrogen vacancies was confirmed by the XPS, elemental analysis and electron paramagnetic resonance (EPR) spectra. Benefitting from the synergistic effect of high crystallinity and N vacancies, CN-NVs-CTe showed excellent hydrogen evolution activity, due to the enhanced charge separation efficiency, improved light absorption ability and charge mobility.

5.2.4. Crystal facet engineering. The engineering of crystal facet to control the reactive surface has been proven to be an efficient method to improve photocatalytic performance.[145] Recent researches have indicated that the photoinduced electrons and holes could be driven to different crystal facets because of the surface heterojunction.[13,146] Therefore, certain facets of a semiconductor tend to favor reduction reaction, while other crystal planes favor oxidation reaction. However, these findings mainly focused on inorganic photocatalysts, Wang and co-workers identified the reactive facets of PTI intercalated with LiCl (PTI/Li^+Cl^-) single crystals for photocatalytic OWS *via* loading appropriate co-catalysts.[106] The highly crystalline PTI/Li^+Cl^- was fabricated by ionothermal method. SEM image (Fig. 13a) reveals the prominent prismatic profile of PTI, which was different from the bulk CN prepared by traditional thermal polycondensation, indicating that the PTI/Li^+Cl^- was completely crystallized. According to the symmetry of PTI/Li^+Cl^-, the two flat hexagonal surfaces must be (0001) facets and the six rectangular surfaces are $(10\bar{1}0)$ facets, as schematically illustrated in Fig. 13b. The high-resolution aberration-corrected integrated differential phase contrast (AC-iDPC) image (Fig. 13c and d) further confirms the high degree of atomic ordering of the PTI/Li^+Cl^-. Furthermore, C, N, and Cl atoms could be distinctly distinguished without tedious image simulation. Therefore, the atomic structure of PTI/Li^+Cl^- crystals was presented and confirmed. The reactive facets were identified by photodeposition of co-catalysts, which could be used as a probe. Interestingly, both the photoexcited electrons and holes accumulated on the {1010} facets, confirming by the selective photodeposition of the Pt or Co. Therefore, increasing the

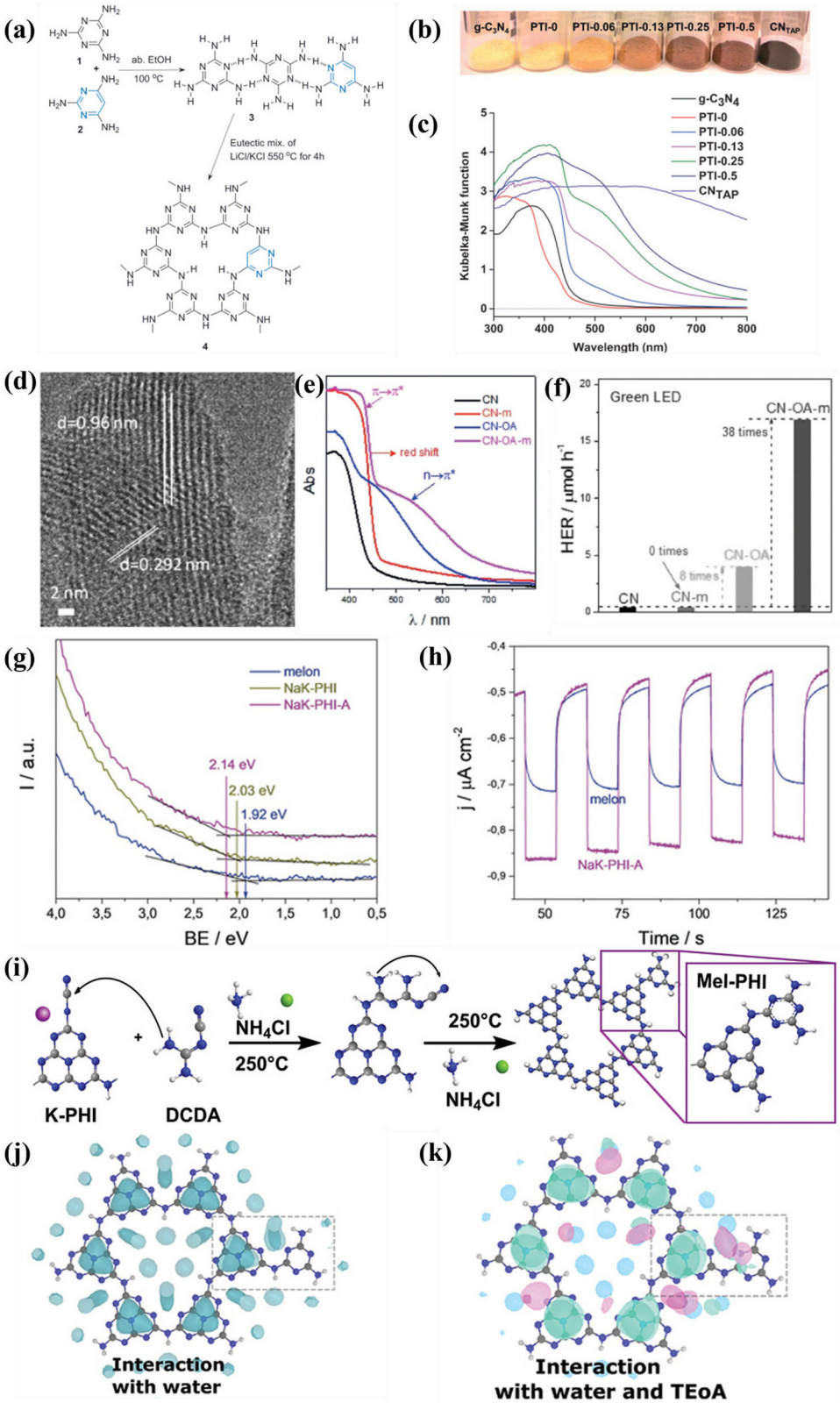

Fig. 12 (a) Schematic illustration of the synthesis of TAP-incorporated PTI. (b) Color and (c) UV-vis DRS of the as-obtained samples. Reproduced with permission.[140] Copyright 2014, Wiley-VCH. (d) HRTEM image of CN-OA-m. (e) UV-vis DRS of the as-prepared samples. (f) Photocatalytic H_2 generation rates of the samples irradiated with green LED. Reproduced with permission.[141] Copyright 2017, Wiley-VCH. (g) UPS spectra of melon, NaK-PHI, and NaK-PHI-A. (h) Photocurrent curves of melon and NaK-PHI-A. Reproduced with permission.[142] Copyright 2019, Wiley-VCH. (i) Schematic illustration for the preparation of Mel-PHI. (j) Interaction of the Mel-PHI with H_2O molecules. (k) Interaction of Mel-PHI with TEOA and H_2O. Reproduced with permission.[143] Copyright 2021, Wiley-VCH.

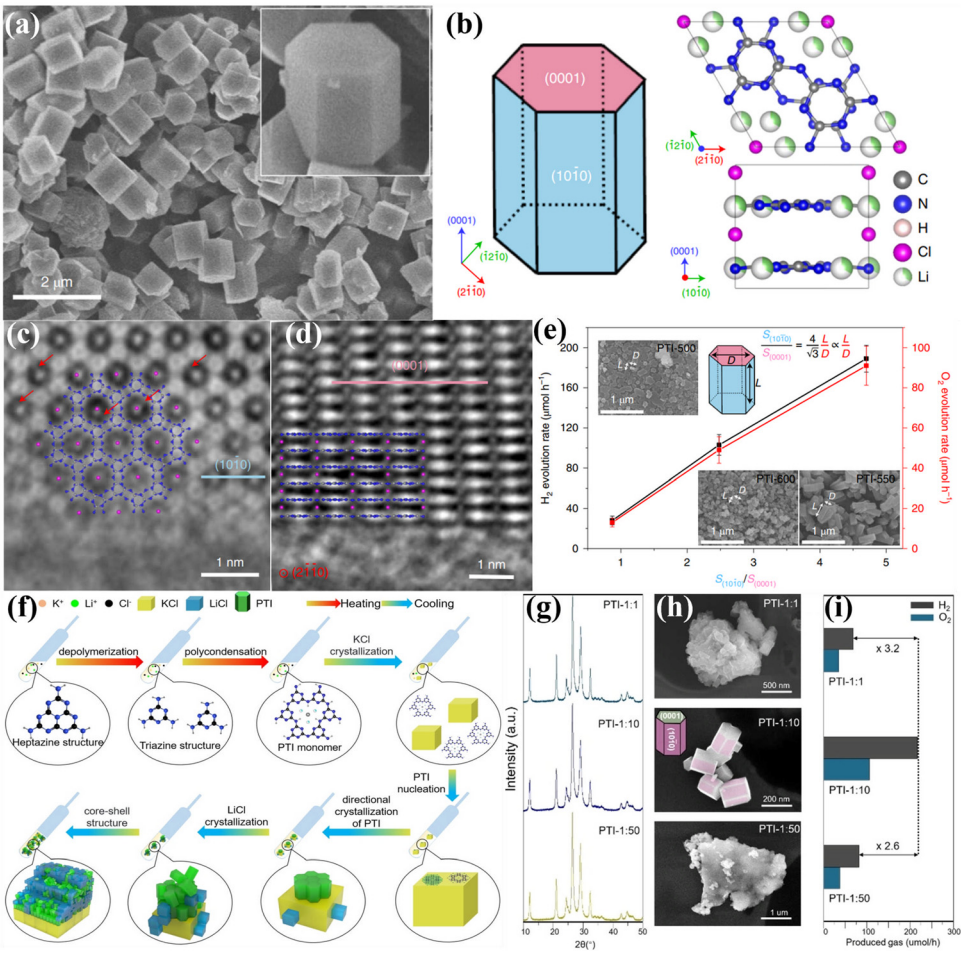

Fig. 13 (a) SEM image of PTI/Li^+Cl^- and the magnified view of the crystal (inset). (b) Schematic representation of the PTI/Li^+Cl^- crystals and the atomic structure of PTI/Li^+Cl^-. (c) AC-iDPC image of PTI/Li^+Cl^- crystal aligned along the [0001] direction. (d) AC-iDPC image of PTI/Li^+Cl^- along the [2$\bar{1}\bar{1}$0] zone axis. (e) The photocatalytic activities on different ratio of {10$\bar{1}$0} and {0001} of the samples prepared at different temperatures. Reproduced with permission.[106] Copyright 2020, Springer Nature. (f) Schematic representation of the molecular conjugation and directional crystallization mechanism of PTI crystals during molten salt process. (g) XRD patterns, (h) SEM images and (i) photocatalytic OWS activities of PTI samples synthesized by tailoring the weight ratio of precursor and salt. Reproduced with permission.[147] Copyright 2023, Wiley-VCH.

prismatic surface areas (reactive facets) could dramatically improve the activity of photocatalytic OWS (Fig. 13e). Notably, the apparent quantum yield (AQY) of PTI-550 reached 8% at 365 nm. Although crystal facet engineering had been achieved, the intrinsic mechanisms of the molecular structure, nucleation and crystallization of PTI-based CCN during the ionothermal process remain unclear. Therefore, the same group used microscopic characterization techniques to reveal the molecular conjugation and crystal growth processes from mesoscale to nanoscale by various sample processing methods.[147] Combining various characterization techniques, the crystallization mechanism of PTI at the molecular scale in molten salts was proposed in Fig. 13f. The heptazine precursors were depolymerized into triazine units, and subsequently PTI-based frameworks was constructed by introducing Li^+ and Cl^- ions. During the crystal precipitation process, the KCl cubes served as a nucleation center and template to guide the orientation and orderly stacking of PTI monomers, thereby producing agglomerated PTI crystals. More importantly, it was found that the aggregation of PTI crystals decreased the exposed area of the active center, which should result in a significant decrease in photocatalytic activity. Therefore, to optimize the photocatalytic performance, it is highly desirable to prevent aggregation and enhance the dispersity by controlling the crystallization fronts, that is, the weight proportion of precursor and salt (Fig. 13g–i). Consequently, when the weight ratio of salt to precursor was 1 : 10, the best photocatalytic activity was realized due to the large exposed reactive facet and good dispersibility (Fig. 13i).

5.3. Development of CCNs-based heterojunctions photocatalysts

Construction of CCNs-based heterojunction has become an attractive strategy to improve the photocatalytic performance of CCNs by boosting the separation of photoexcited electrons and holes. The CCNs-based heterojunction can be classified into isotype heterojunction, semiconductor/CCN heterojunction, carbon/CCN heterojunction and metal/CCN heterojunction. The isotype heterojunction constructed between two different crystalline

phases of the same substance (known as crystal-phase heterojunctions) was an useful approach to enhance the photocatalytic performance,[148–150] which in this section was categorized as amorphous/crystalline CN heterojunction[151–155] and heptazine/triazine-based CCN heterojunction.[156–161]

5.3.1. Amorphous/crystalline CN heterojunction. Considering the obviously different band structures of amorphous CN (ACN) and CCN, the construction of an isotype heterojunction is an efficient strategy to accelerate interfacial charge transfer and improve photocatalytic activity.[153,154] For instance, Yang and co-workers obtained melon-based ACN and triazine-based CCN heterojunction through a simple thermal treatment of graphitic CN with LiCl.[151] HRTEM analysis confirmed the establishment of isotype heterojunction (Fig. 14a), where the phase junction was constructed by (002) plane of triazine-based CCN and ACN. The optimized sample displayed better photocatalytic performance for degradation of RhB than mono-component ACN and CCN (Fig. 14b). Such an enhanced photocatalytic performance could be ascribed to the effective separation and transfer of photoexcited electrons and holes caused by the isotype heterojunction. Similarly, Yang and co-workers constructed an amorphous/crystalline CN heterojunction *via* two-step polymerization of melemon, using CCN nanosheets as seeds to achieve efficient photocatalytic hydrogen evolution.[152] Jiang and co-workers designed an amorphous/crystalline lateral heterojunction through a multi-step chemical vapor deposition (CVD) method.[152] The isotype heterojunction was edge-epitaxially grown at 650 °C using CCN as seeds. The heterojunction interface was clear between the crystalline and amorphous CN (Fig. 14c). The amorphous/crystalline CN showed improved photocatalytic activity over crystalline and amorphous CN (Fig. 14d) because of the efficient charge separation across the heterointerfaces at the isotype heterojunction.

5.3.2. Different building blocks-based CCNs heterojunctions (phase heterojunctions). Taking into account the different band structures of the building units in the CN framework, it is desirable to build a CCN heterojunction based on different building blocks, which could facilitate the orientation transfer of interfacial electronics and inhibit the recombination of charge carriers. Chen and co-workers prepared a triazine/heptazine-based CCN isotype heterojunction by microwave-assisted thermolysis approach in KCl/LiCl salts (Fig. 15a).[156] The XRD result showed two sets of diffraction peaks, which assigned to the triazine-based and heptazine-based CCNs, respectively (Fig. 15b). Furthermore, the flat band potentials of the triazine-based CCN and heptazine-based CCN estimated from the Mott–Schottky plots were −0.90 V and −1.22 V, respectively, confirming different electronic band structures and the construction of the isotype heterojunction. The as-obtained sample showed high photocatalytic hydrogen evolution activity, which could be attributed to the effective separation of photoexcited electron–hole pairs because of the isotype triazine/heptazine heterojunction (Fig. 15c).

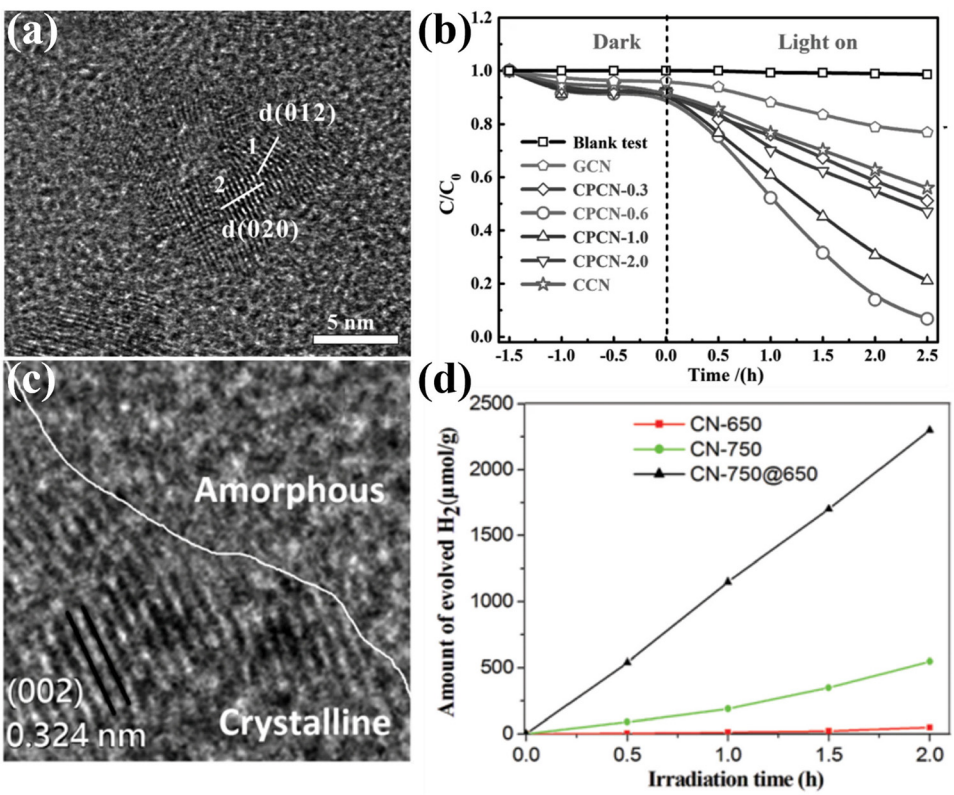

Fig. 14 (a) HRTEM image of CPCN. (b) Photocatalytic degradation performance of the samples. Reproduced with permission.[151] Copyright 2017, Wiley-VCH. (c) TEM image of CN-750@650. (d) Photocatalytic H_2 generation rates of the samples under visible light ($\lambda > 420$ nm). Reproduced with permission.[155] Copyright 2019, Royal Society of Chemistry.

Although the above studies had confirmed the triazine-/heptazine-based isotype heterojunction, they did not provide a clear interface for phase heterojunctions. Quan and co-workers developed a secondary growth method for the preparation of CCN phase heterojunction (triazine/heptazine), in which the triazine-based CCN was vertically aligned on heptazine-based CCN.[158] The XRD pattern confirmed the coexistence of triazine-based CCN and heptazine-based CCN. The HRTEM analysis further demonstrated the phase heterojunction, which consisted of well-matched lattice fringes between (002) plane of heptazine-based and triazine-based CCN, respectively. Owning to the increased crystallinity and accelerated charge separation, the triazine-/heptazine-based CCN exhibited higher photocatalytic performance than that of PTI and melon-based CN. Wang and co-workers fabricated a triazine/heptazine-based CCN with D–A heterostructure in eutectic salts (NaCl/KCl).[159] This NaCl/KCl mixture had a much higher melting point of 652 °C compared with the formerly used KCl/LiCl mixture, which resulted in the CN solids being only partial "dissolution" and forming triazine-based PTI. The high-resolution XPS displayed a significant increase in the peak of a more electron-poor N atom during the molten salt treatment process, suggesting the co-existence of triazine and heptazine building blocks (Fig. 15d). The clear lattice fringes demonstrated the high crystallinity, confirming that the post-condensation in appropriate salt mixtures could modulate the polycondensation process (Fig. 15e). Despite the reduced crystallinity, the CCN still exhibited excellent hydrogen production performance because the well-designed D–A structure accelerated the transfer of charge carriers at the interface. In another study, Xiang and co-workers prepared a crystalline isotype heptazine-/triazine-based heterojunction through molten salt approach using preheated melamine as the precursor.[161] The heterojunction structure and interfacial interactions were first confirmed by first principle calculations. Due to the high crystallinity and heterojunction structure, the optimized sample showed an excellent photocatalytic hydrogen generation rate of 890 μmol h^{-1} g^{-1}, and an AQY of 26.7% at 420 nm.

Recently, Wang and co-workers synthesized PHI/PTI heterojunction with a semi-coherent interface by a simple two-step

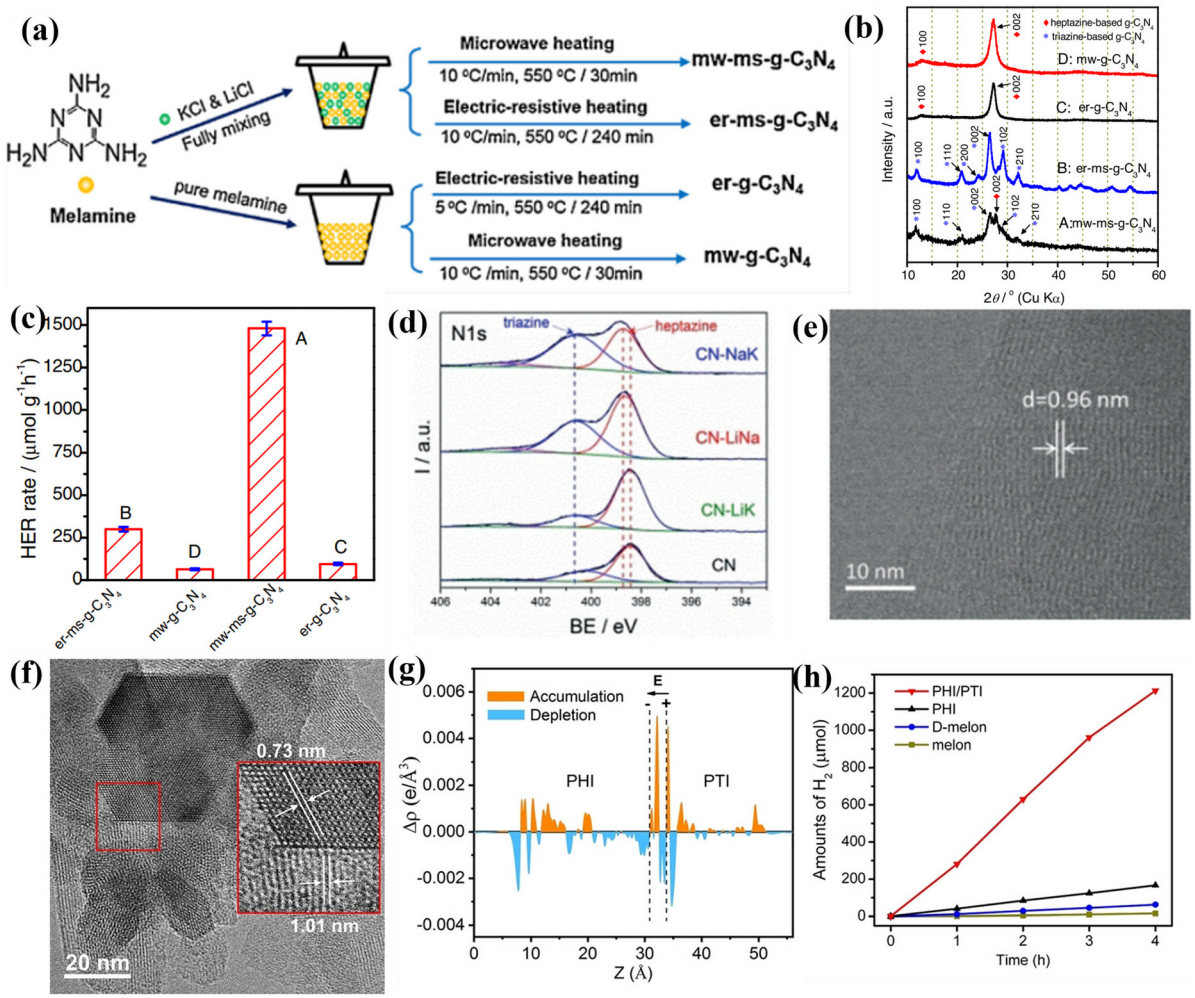

Fig. 15 (a) Schematic illustration of the synthesis of g-C_3N_4 photocatalysts. (b) XRD patterns of the samples. (c) Photocatalytic H_2 production rates of the samples. Reproduced with permission.[156] Copyright 2017, Elsevier. (d) High-resolution N1s XPS spectra of CN, CN-LiNa, CN-LiK, and CN-NaK. (e) HRTEM image of CN-NaK. Reproduced with permission.[159] Copyright 2018, Wiley-VCH. (f) HRTEM image of PHI/PTI. (g) The average charge density difference over the PHI/PTI heterojunction. (h) Photocatalytic H_2 production performances of the samples. Reproduced with permission.[162] Copyright 2022, Wiley-VCH.

molten salt method.[162] The HRTEM image demonstrates that the semi-coherent interface was constructed by two lattice fringes with spacing of 1.01 and 0.73 nm, which corresponded to the (10–10) plane of PHI and PTI, respectively (Fig. 15f). Moreover, the DFT calculations demonstrates that the electrons redistribution was observed across the semi-coherent interface, thereby establishing an intrinsic electric field and regulating the charge flow transport from PHI to PTI (Fig. 15g). As a result, the PHI/PTI presented a remarkably enhanced photocatalytic H_2 generation performance of 348.5 μmol h^{-1} because of the promoted charge separation and transfer (Fig. 15h).

5.3.3. Semiconductor/CCN heterojunctions. The design of semiconductor heterojunctions by hybridizing two different semiconductors with appropriate VB and CB potentials is an effective strategy to promote charge transfer and separation.[22,163] Until now, a large number of semiconductors have been coupled with CCNs to construct CCNs-semiconductor heterojunction photocatalysts, including ZnO,[164,165] $ZnIn_2S_4$,[166] TiO_2,[167] WO_X,[168,169] CdS,[170] Ti-based metal–organic framework,[171] CoP.[172] Sun and co-workers synthesized a PTI/ZnO composite photocatalyst by a facile one-step ionothermal approach.[164] The ZnO quantum dots (QDs) were well distributed on the surface of PTI nanosheets with close contact interfaces, thereby enhancing the photocatalytic activity. Jiang and co-workers synthesized WO_x/CCN layered heterojunction photocatalyst *via* a hydrothermal method.[168] The WO_x nanobelts were horizontally grown on ultrathin CCN nanosheets, thus forming a layered-heterojunction. Upon illumination, the photoexcited electrons tended to transfer from the CB of $W_{18}O_{49}$ to CCN, which could effectively promote the charge separation and inhibit the recombination of charge carriers. This spatial separation of photoexcited charge carriers could greatly improve the photocatalytic hydrogen production of the WO_x/CCN layered heterostructure. Yu and co-workers fabricated $Ba_xSr_{1-x}TiO_3$ (B_xST)/K-PHI composite photocatalysts *via* a facile electrostatic self-assembly approach.[173] The HRTEM image confirms that the K-PHI nanosheets were distributed on the surface of $B_{0.8}$ST with clear and intimate contact interface, promoting the separation and transport of photoinduced carriers (Fig. 16a). Moreover, the K^+ cations in the K-PHI could construct a charge-transfer channel to facilitate charge migration. As a consequence, the 5% K-PHI/$B_{0.8}$ST exhibited remarkably enhanced photocatalytic H_2 production performance, reaching 1087.4 μmol h^{-1} g^{-1} (Fig. 16b). Very recently, Xiang and co-workers reported that atomically Co-doped CeO_2 was coupled with crystalline PTI to construct a S-scheme Co-doped CeO_2/PTI (CeCo-PTI) composites for the selective production of CH_4.[174] The aberration-corrected high-angle annular dark-field scanning transmission electron microscopy (HAADF-STEM) image demonstrates the formation of a distinct interface between Co-doped CeO_2 and crystalline PTI (Fig. 16c and d). Moreover, the lattice distance of 0.33 nm corresponded to the (002) facets of graphitic CN (Fig. 16c). Furthermore, the wavelet transform (WT) contour plots revealed that a main peak at 1.5 Å was observed in the CeCo-PTI, assigned to the Co-O bonds, suggesting that the single-atomic Co was coordinated with the O atoms (Fig. 16e). Notably, the CeCo-PTI presented remarkably enhanced photocatalytic activity with CH_4 and CO production rates of 45.4 and 24.0 μmol g^{-1} h^{-1}, respectively, which was much larger than those of Co-PTI and PTI (Fig. 16f). Such remarkably improved photocatalytic performance could be ascribed to the excellent single-atom Co modulation as well as the S-scheme heterojunction, which provided the driving force for the directional charge transport.

5.3.4. Carbon/CCN heterojunctions. Carbon nanomaterials with π-conjugated structures, including graphene, are considered as promising support or reduction cocatalyst due to their extraordinary structural and electronic properties, which could prevent the recombination of the photoexcited electron–hole pairs. A case in point, our group designed a 1D/2D heterojunction of CCN nanoarrays (CNNA) aligned on 2D graphene nanosheet through an ionothermal method (Fig. 17a).[175] The HRTEM image shows clear lattice fringes of 1.12 nm, indicating the high crystallinity (Fig. 17b). Moreover, another noteworthy finding was the greatly improved adsorption capacity of CO_2 due to the heterojunction effect and ordered 1D structure. This was further confirmed by the isosteric heat (Q_{st}), in which the Q_{st} of CNNA/rGO was increased to 55.2 kJ mol^{-1}, which was larger than the value reported for many specialized CO_2 capture materials, indicating that the CO_2 molecules were strongly chemically adsorbed on the surface of CNNA/rGO. Thus, the CNNA/rGO showed high CO_2 photoreduction selectivity (87%), with an overall CO_2 conversion of 12.63 μmol h^{-1} g^{-1}, which could outperform other optimized CN-based photocatalysts (Fig. 17c).

5.3.5. Metal/CCN heterojunctions. Decoration of metal nanoparticles on CN surface has proven to be an effective approach to inhibit photogenerated electron–hole recombination and improve light utilization efficiency. It is well known that the size of metal cocatalyst is an essential factor affecting the catalytic performance.[176,177] In particular, reducing the particle size of the cocatalyst could dramatically improve the atom utilization and provide more active sites. Single atom photocatalysts, which contains single metal atoms anchored to photocatalysts, have attracted increasing attention due to their maximum atom utilization efficiency, uniform coordination environment, and the unique electronic structure.[178–183] Xiang and co-workers prepared a single Cu atom/CCN photocatalyst (Cu–CCN) by molten salt and reflux approach.[184] The XRD pattern of the Cu–CCN showed a decreased interlayer distance, confirming the successful incorporation of single Cu atoms. In addition, HAADF-STEM image demonstrates the existence of single Cu atoms, which were randomly distributed on Cu–CCN (Fig. 17d). The extended X-ray absorption fine structure (FT-EXAFS) spectroscopy and wavelet transform revealed the presence of Cu–N bond with a coordination number of 6, while no Cu–Cu bond was observed in the Cu–CCN, confirming that almost all Cu atoms existed as isolated single atoms (Fig. 17e). Notably, the introduction of single Cu atoms could serve as the adsorption and active sites for CO_2 reduction, thereby improving the adsorption ability of CO_2. DFT calculation demonstrated that the CO_2 to CO reaction is an energetically favorable process compared with the reduction of CO_2 to CH_4. Therefore, the Cu–CCN displayed improved photocatalytic CO_2 reduction activity and high selectivity (nearly 100%) for the conversion of CO_2 to CO.

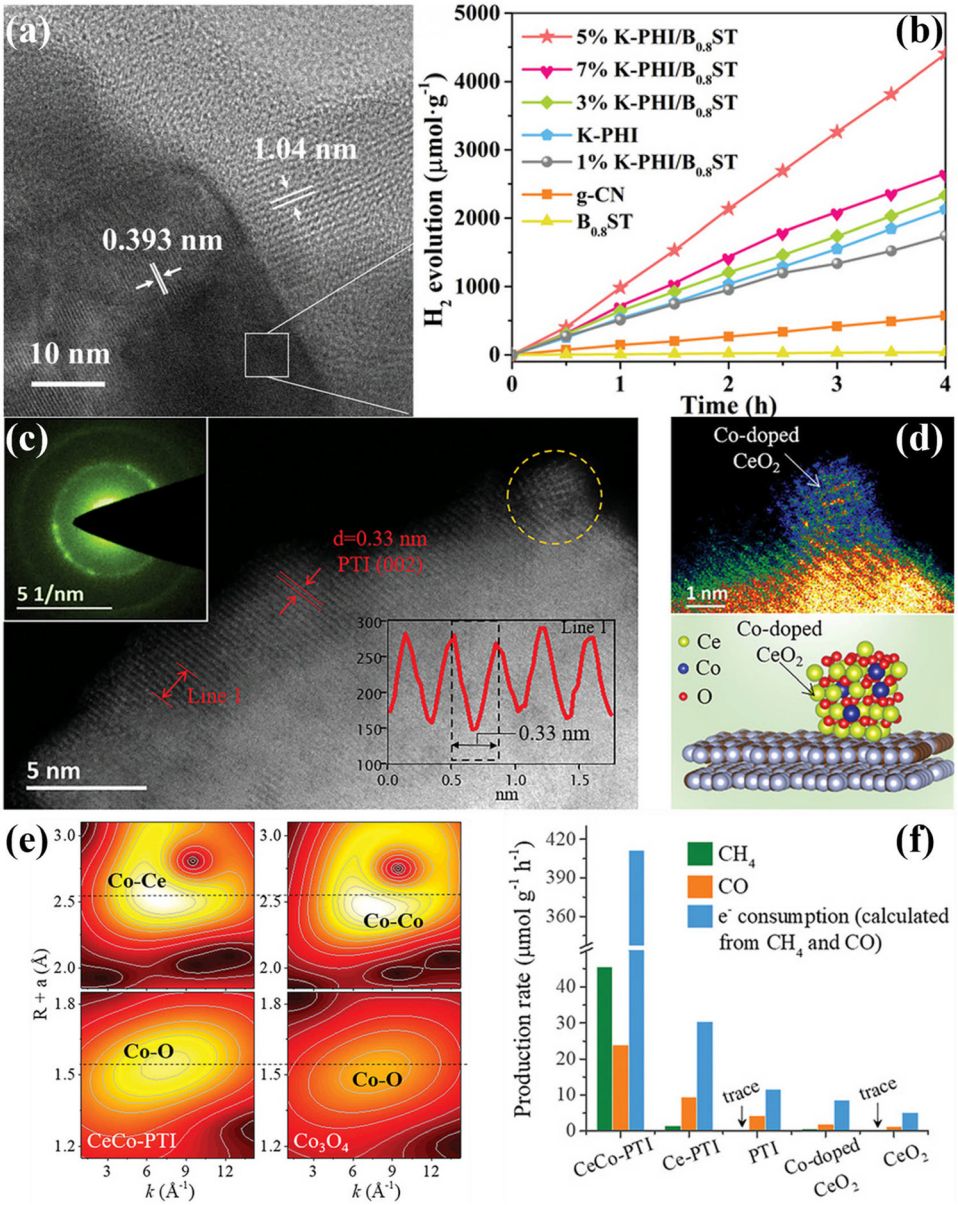

Fig. 16 (a) HRTEM image of 5% K-PHI/$B_{0.8}$ST. (b) Photocatalyitc H_2 production rates of the samples irradiated with visible-light (λ > 420 nm). Reproduced with permission.[173] Copyright 2022, Wiley-VCH. (c) and (d) AC HAADF-STEM image of CeCo-PTI. The structure model of CeCo-PTI is displayed at the bottom right. (e) Wavelet transform (WT) contour plots of CeCo-PTI (left) and Co_3O_4 (right). (f) CH_4 and CO production rate of the samples, as well as the equivalent electron consumption. Reproduced with permission.[174] Copyright 2022, Wiley-VCH.

6. Application of CCNs-based photocatalysts

In this section, we will focus on recent progress of CCNs-based photocatalysts for photocatalytic applications such as photocatalytic water splitting, photocatalytic CO_2 reduction, photocatalytic degradation of pollutants, selective organic syntheses and H_2O_2 production. In the following subsections, various photocatalytic applications of CCNs-based photocatalysts are briefly outlined. Some selected examples are described based on the latest findings.

6.1. Photocatalytic water splitting

Direct water splitting for H_2 generation using photocatalysts and sunlight is a sustainable technology that conversion of solar energy into valuable hydrogen energy. Theoretically, for CCNs photocatalyst, overall water splitting could be achieved on account of suitable CB and VB positions.[106,124,185–188] For example, Wang and co-workers achieved overall water splitting by using crystalline PTI as photocatalyst without sacrificial reagents.[185] The *in situ* photodeposition of Pt/Co on the PTI not only improved the photocatalytic performance, but also adjusted the ratio of H_2 and O_2 to 2 : 1 by tuning the amount of

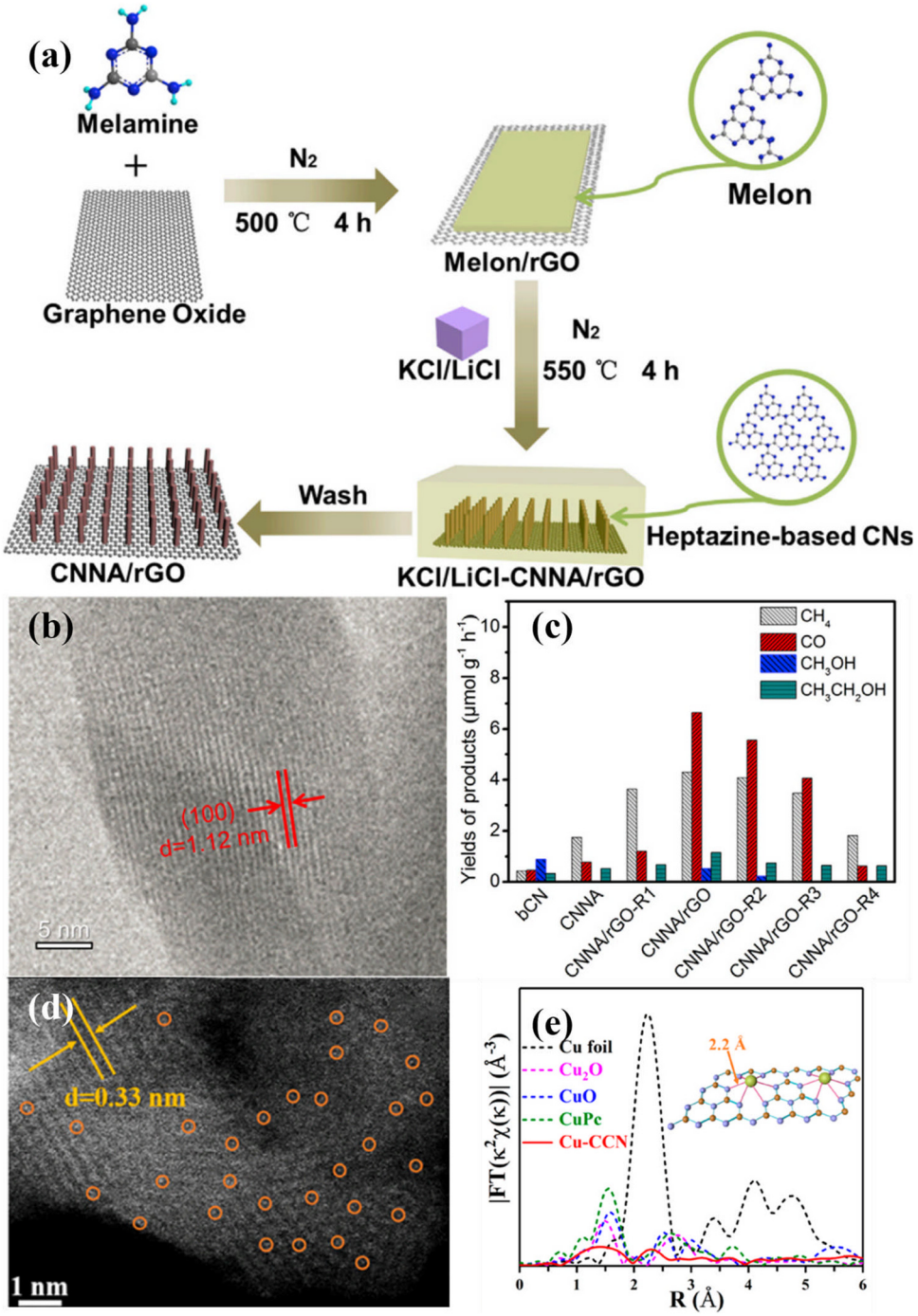

Fig. 17 (a) Schematical illustration of the preparation of CNNA/rGO. (b) HRTEM image of CN nanorod in CNNA/rGO. (c) Photocatalytic CO_2 reduction activities of bCN, CNNA, CNNA/rGO-R4, and CNNA/rGO. Reproduced with permission.[175] Copyright 2019, Elsevier. (d) HAADF-STEM image of Cu–CCN. (e) FT-EXAFS of the samples.[184] Copyright 2020, American Chemical Society.

Co cocatalyst. The AQY at 380 nm was calculated to be 2.1%. The low efficiency of overall water splitting is presumably because of the kinetic restriction of the oxygen evolution reaction. Motivated by this work, the same group further investigated the photoactivity of overall water splitting by using Co and Pt cocatalysts to identify the reactive facets of single crystal PTI/Li^+Cl^-.[106] It was found that both the reduction and oxidation reactions preferred to occur on the same {1010} crystal plane, which was distinct from the spatial separation of reduction and oxidation reactions for $BiVO_4$ and TiO_2 photocatalyst. Based on this finding, increasing the prismatic surface area (reactive facets) could dramatically improve the activity of photocatalytic overall water splitting. Moreover, it was demonstrated that the lower defect densities could lead to superior photocatalytic performance. Motivated by this research, the same group developed a fully condensed poly (triazine imide) photocatalysts with

expanded π-conjugated system and low density structural defects through a mild ionothermal strategy with LiCl/NaCl.[189] The melting point of LiCl/NaCl is about 552 °C, closing to the polymerization temperature, thereby providing moderate reaction condition and preventing the depolymerization of triazine monomer. The binding energies of C–N=C in PTI-LiNa showed a positive shift of 0.35 eV, implying that the completely condensed nitrogen species were formed (Fig. 18a). The PTI-LiNa displayed the best photocatalytic overall water splitting performance with the H_2 and O_2 generation rate of 273 and 135 μmol h^{-1} because of the effective exciton dissociation and the promotion of the transfer and migration of photogenerated charge carrier (Fig. 18b).

Recently, the use of CCNs-based photocatalysts for hydrogen production half reaction has been intensively investigated, as this is a less difficult reaction than photocatalytic overall water splitting. However, low efficiency still hinders its practical application. Therefore, several modification strategies of pristine CCNs, including nanostructure design, molecular structure engineering and heterojunction construction have been systematically studied to optimize the photocatalytic activity. The latest progress using CCNs-based photocatalysts for photocatalytic H_2 generation are summarized in Table 2 without detailed discussion. It is demonstrated that CCNs prepared from various precursors[64,140,141,190] and molten salts[61,64,115,191,192] exhibited different photocatalytic activities due to different crystal structures of the products. In general, the specific morphology and microstructure of CCNs could promote charge separation and transfer, as well as provide more active sites, thereby enhancing the photocatalytic hydrogen evolution activity. For example, numerous CCNs nanosheet[65,94,112–114,123,124] have been proven to be effective in enhancing the photocatalytic H_2 production performance. Moreover, Lotsch and co-workers investigated how particle size and surface functional groups affect the photocatalytic performance.[193] The particle size and surface defects were systematically modulated by ultrasonication approach. It was demonstrated that optimal amount of defect not only accelerated the charge separation, but also facilitated the loading of Pt and reduced its size, thus boosting the photocatalytic H_2 production activity. Apart from the nanostructure design, the defect engineering and molecular doping could narrow the bandgap and boost charge separation, thereby improving the photocatalytic hydrogen production performance, as detailed in Section 4.2. For instance, Zhang and co-workers proposed the doping of oxamide molecular into the PHI-based CCN to enhance the photocatalytic H_2 production performance, which was 38 times higher than that of CN under green LED light irradiation.[141] Lotsch and co-workers investigated the influence of ionic conductivity on photocatalytic activity by adjusting various counterions in the PHI framework.[194] It was indicated that the ions influenced the stacking of 2D layers, thereby affecting the ionic conductivity, which was the bottleneck of electron stabilization and extraction. Benefiting from the highest ionic conductivity, the Na-PHI exhibited the best photocatalytic H_2 production performance. Apart from the molecular structure engineering, construction of CCNs-based heterojunctions is another effective approach for improving the photocatalytic performance by accelerating the separation and transfer of charge carriers. For instance, Wang and co-workers fabricated a triazine/heptazine-based CCN with D–A heterostructure to improve the photocatalytic H_2 production performance by promoting interfacial charge carrier transfer.[159]

However, the conventional H_2 production half-reaction is achieved by using various sacrificial reagents, which increases cost and wastes the energy of holes. To address this issue, the coupling of organic synthesis with H_2 evolution reaction has emerged as an appealing strategy, which not only makes full use of photoexcited electron and hole to realize sustainability targets, but also enhances the performance of photocatalytic H_2 production. Recently, some organic substrates coupled with H_2 evolution have been reported on CCNs-based photocatalysts, including bisphenol A[195] and cellulose.[196]

In addition to the hydrogen production reaction, the half reaction of O_2 produced from water oxidation is a complex multi-electron transfer process requiring a large overpotential. The CCN has also been shown as a promising catalyst for photocatalytic water oxidation. In a recent work, Wang and co-workers developed a van der Waals homojunction of Zn-PHI/PHI for photocatalytic O_2 evolution through a ternary molten salt approach.[197] The Zn doped PHI generated during the calcination process contributed to the formation of homojunction, which created an hole migration channels and promoted charge separation. Consequently, the AQY of the optimized photocatalyst reached up to 3.6% at 420 nm.

6.2. Photocatalytic CO_2 reduction

With the rapid industrialization and economic development, the concentration of greenhouse gases, *i.e.*, carbon dioxide in the atmosphere, is increasing. Therefore, it is desirable to reduce its concentration through capture or conversion. Inspired by the photosynthesis of natural green plants, artificial photosynthesis, photocatalytic conversion of CO_2 into hydrocarbon fuels has been recognized as an appealing technology to mitigate greenhouse effect and address global energy shortage. The photocatalytic reduction of CO_2 is a complex multistep process, as shown in eqn (1)–(8),[223] the possible products and corresponding redox potentials (*versus* normal hydrogen electrode (NHE) at pH 7) are listed below

$$CO_2 + e^- \rightarrow CO_2^\bullet \quad E^0_{redox} = -1.9\ V \tag{1}$$

$$CO_2 + 2H^+ + 2e^- \rightarrow CO + H_2O \quad E^0_{redox} = -0.53\ V \tag{2}$$

$$CO_2 + 2H^+ + 2e^- \rightarrow HCOOH \quad E^0_{redox} = -0.61\ V \tag{3}$$

$$CO_2 + 4H^+ + 4e^- \rightarrow HCHO + H_2O \quad E^0_{redox} = -0.48\ V \tag{4}$$

$$CO_2 + 6H^+ + 6e^- \rightarrow CH_3OH + H_2O \quad E^0_{redox} = -0.38\ V \tag{5}$$

$$CO_2 + 8H^+ + 8e^- \rightarrow CH_4 + 2H_2O \quad E^0_{redox} = -0.24\ V \tag{6}$$

$$2CO_2 + 12H^+ + 12e^- \rightarrow C_2H_4 + 4H_2O \quad E^0_{redox} = -0.33\ V \tag{7}$$

$$2CO_2 + 12H^+ + 12e^- \rightarrow C_2H_5OH + 3H_2O \quad E^0_{redox} = -0.32\ V \tag{8}$$

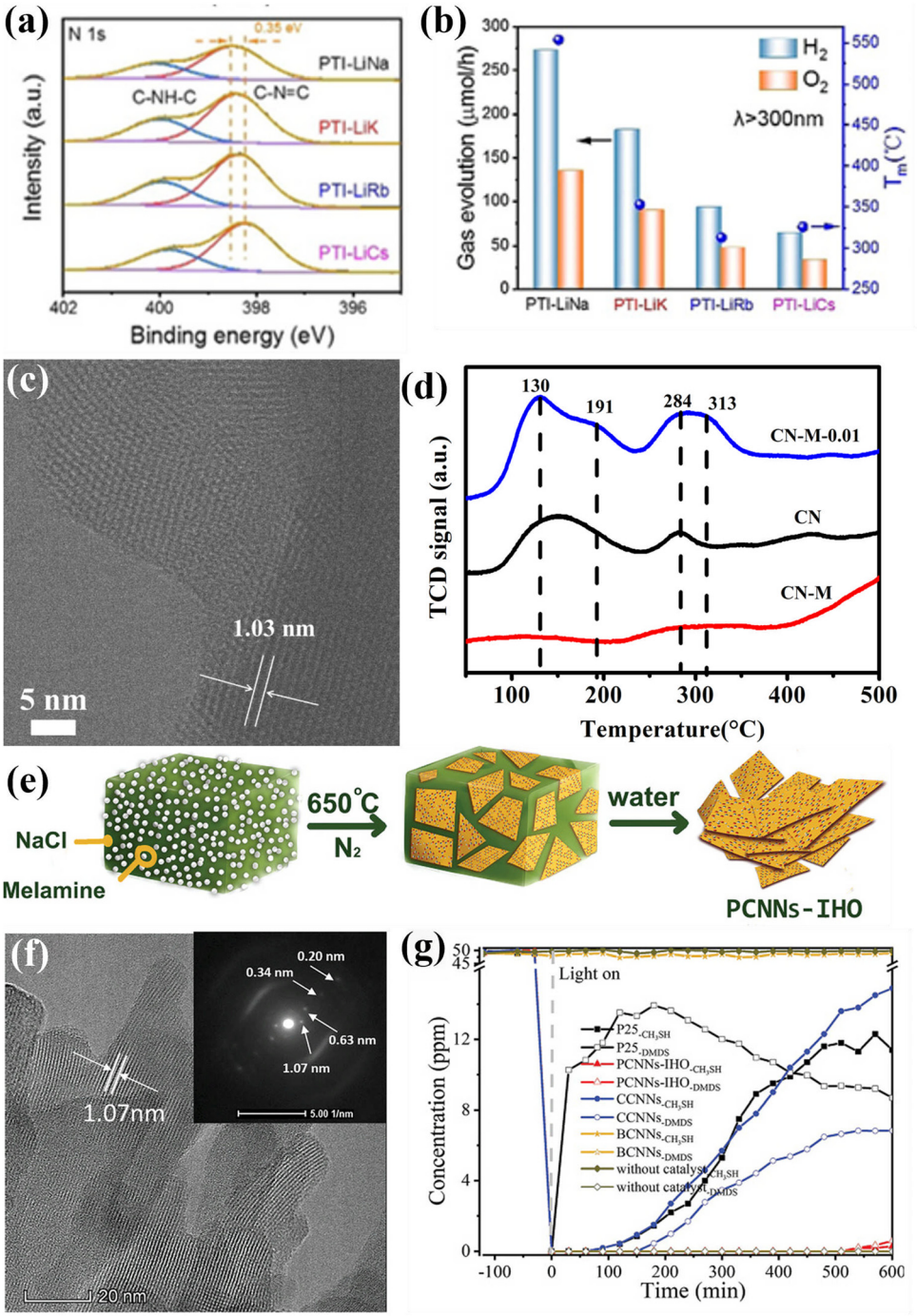

Fig. 18 (a) High-resolution N1s XPS spectra of PTI-LiNa, PTI-LiK, PTI-LiRb and PTI-LiCs. (b) Photocatalytic overall water splitting performances of PTI/Li^+Cl^- prepared in different eutectic salts along with their melting points. Reproduced with permission. Copyright 2022, Wiley-VCH. (c) HRTEM image of CN-M-0.01. (d) CO_2 TPD measurements. Reproduced with permission.[224] Copyright 2020, Royal Society of Chemistry. (e) Schematical diagram of the preparation of PCNNs-IHO through on-surface polymerization. (f) HRTEM image of PCNNs-IHO and SAED pattern of the (100) plane (inset). (g) Photocatalytic CH_3SH mineralization performance of PCNNs-IHO, CCNNs, BCNNs, and P25. Reproduced with permission.[97] Copyright 2021, Wiley-VCH.

Based on the above reaction process, the photocatalytic CO_2 reduction is a proton-assisted multi-electron reaction process, which affects the selectivity of products. Moreover, the CO_2 molecules are extremely difficult to be activated to participate in the reactions due to their stable linear structure and chemical inertness. Meanwhile, the proton donor for CO_2 reduction should be provided by H_2O. Thus, the hydrogen production *via* reducing H_2O is a competitive reaction for photocatalytic CO_2 reduction, resulting in a low selectivity and activity for CO_2 reduction. These factors make it difficult to realize high efficiency and good

Table 2 Photocatalytic H_2 generation of CCNs-based photocatalysts

Photocatalysts	Cocatalyst	Reactant solution	Light source	Activity (μmol g^{-1} h^{-1}), stability and quantum efficiency	Ref.
CCN intercalation compound	3 wt% Pt	100 mL of TEOA (10 vol%) and saturated salt solution	300 W, Xe lamp, >420 nm	5020.0, 50% decrease in activity under 20 h irradiation (5 h per run), 21.2% 420 nm	61
PTI/Li^+Cl^-	5 wt% Pt	100 mL of TEOA (10 vol%)	300 W, Xe lamp, >300 nm	800.0, N/A, N/A	64
PTI nanosheets	2.2 wt% Pt	10 ml of TEOA (10 vol%)	300 W, Xe lamp, >420 nm	1750.0, retained after 6 cycles, 1.3% 400 nm	65
PTI-0.13	3 wt% Pt	25 ml of TEOA (10 vol%)	300 W, Xe lamp, >420 nm	8160.0, N/A, 7.0% 420 nm	140
LiK-CCN	3 wt% Pt	38 mL of TEOA (10 vol%)	50 W white LED array, >410 nm	812.0, slight drop under 72 h irradiation (12 h per run), N/A	190
PTI-0.15/KCC-1	3 wt% Pt	25 mL of TEOA (10 vol%)	300 W, Xe lamp, 385–740 nm	1320.0, stable after 4 cycles (10 h per cycle), 16.9% 420 nm	118
MoS_2/PHI	N/A	38 mL of TEOA (10 vol%)	50 W white LED array, >410 nm	53.6, sustained over 65 h, 0.2% 420 nm	198
ZnO QDs/PTI	3 wt% Pt	100 mL of TEOA (10 vol%)	300 W, Xe lamp, ≥420 nm	440.0, stable after 12 h irradiation, 1.27% 420 nm	164
PHI-based CCN	3 wt% Pt	100 mL of TEOA (10 vol%) and K_2HPO_4 (0.01mol)	300 W, Xe lamp, ≥420 nm	15 400.0, high stability, 50.7% 420 nm	115
PTI/PHI-based CCN	3 wt% Pt	50 mL of TEOA (10 vol%)	300 W, Xe lamp, ≥420 nm	1480.0, no obvious decrease in activity after 3 cycles (4 h per cycle), 10.7% 420 nm	156
PHIK-0.5	3 wt% Pt	38 mL of TEOA (10 vol%)	50 W white LED array, >410 nm	656.0, N/A, N/A	199
PTI-based CCN	1 wt% Pt and 9 wt% Co	100 mL of methanol (10 vol%)	300 W, Xe lamp	649.0, N/A, 2.1% 380 nm	185
PHI-Mg	1.57 wt% Pt	TEOA	50 W white LED array	1255.0, N/A, N/A	200
CN-OA-m	3 wt% Pt	38 mL of TEOA (10 vol%)	50 W green LED light, 525 ± 1.0 nm	340.0, no evident decrease in activity after four runs, 10.0% 525 nm	141
Na-PHI	0.51wt% Pt	38 mL of TEOA (10 vol%)	50 W white LED array	1344.0, N/A, N/A	192
CCN nanorods	3 wt% Pt	100 mL of TEOA (10 vol%)	300 W, Xe lamp, >420 nm	1680.0, N/A, N/A	92
CCN nanosheets	3 wt% Pt	100 mL of methanol (10 vol%)	>420 nm	1060.0, no evident change in activity after 3 cycles (4 h per run), 8.57% 420 nm	112
PTI/PHI-based CCN	1 wt% Pt	100 mL of TEOA (10 vol%)	300 W, Xe lamp, >420 nm	4813.2, N/A, N/A	157
CCN nanosheets	3 wt% Pt	10 mL of TEOA (10 vol%)	300 W, Xe lamp, >400 nm	2570.0, no detectable decresase in activity after 4 cycles, N/A	114
Amorphous/crystalline CN	2 wt% Pt	100 mL of TEOA (10 vol%)	300 W, Xe lamp, >420 nm	1179.0, no obvious activity decay after 4 cycles (2 h per cycle), N/A	152
Amorphous/crystalline CN	N/A	80 mL of TEOA (10 vol%)	300 W, Xe lamp, >420 nm	310.0, stable after 3 cycles, 1.86% 420 nm	154
CCN	0.5 wt% Pt	10 mL of TEOA (15 vol%)	300 W, Xe lamp, >420 nm	2000.0, no obvious activity decay after 4 cycles (3 h per cycle), 5.6% 420 nm	89
CCN-ATZ-NaK	3 wt% Pt	38 mL of TEOA (10 vol%) and 0.01mol K_2HPO_4	50 W white LED light, >420 nm	13 000.0, no evident decrease in activity, 65.0% 420 nm	201
PTI/PHI-based CCN	3 wt% Pt	38 mL of TEOA (10 vol%) and NaCl 3 wt%	50 W white LED light, >420 nm	11 720.0, no evident decrease in activity after 4 runs (4 h per run), 60% 420 nm	159
CCN nanosheets	3 wt% Pt	300 mL of TEOA (10 vol%)	300 W, Xe lamp, >400 nm	808.5, no obvious activity decay after 4 runs (4 h per run), 6.17% 420 nm	117
CCN	3 wt% Pt	100 mL of methanol (10 vol%)	300 W, Xe lamp, >420 nm	660.0, no obvious activity decay after 6 cycles (4 h per cycle), 6.8% 420 nm	202
PTI/PHI-based CCN	3 wt% Pt	100 mL of TEOA (10 vol%)	300 W, Xe lamp, >420 nm	2880.0, no obvious activity decay after 4 cycles (4 h per cycle), 12.9% 420 nm	158
S-doped CCN	1 wt% Pt	80 mL of TEOA (20 vol%)	300 W, Xe lamp, >420 nm	1511.2, no obvious activity decay after 5 cycles (3 h per cycle), 3.9% 420 nm	128
Holey CCN nanosheets	0.2 wt% Pt	100 mL of TEOA (10 vol%)	300 W, Xe lamp, >420 nm	1631.6, no obvious activity decay after 4 cycles (4 h per cycle), 2.1% 420 ± 15 nm	123
CCN nanosheets	3 wt% Pt	100 mL of TEOA (10 vol%)	300 W, Xe lamp AM1.5 G	9577.6, retained in 5 cycles (2.5 h per cycle), 9.01% 420 nm	113
Single crystalline melem	1 wt% Pt	80 mL of TEOA (10 vol%)	300 W, Xe lamp, >400 nm	74.6, N/A, N/A	203
NaK-PHI-A	3 wt% Pt	38 mL of TEOA (10 vol%)	100 W white LED light	6840.0, almost no change in activity after 4 runs (4 h per run), N/A	142
CCN	3 wt% Pt	20 mL of TEOA (5 vol%)	Blue LED lamp (450 nm)	2100.0, N/A, 13.0% 450 nm	204
Defect-CCN	3 wt% Pt	100 mL of TEOA (10 vol%)	300 W, Xe lamp, ≥455 nm	1280.0, no significant activity decay after 4 cycles (4 h per cycle), 3.5% 420 nm	134

Table 2 (*continued*)

Photocatalysts	Cocatalyst	Reactant solution	Light source	Activity (μmol g^{-1} h^{-1}), stability and quantum efficiency	Ref.
3D porous CCN	1 wt% Pt and 3 wt% IrO_2	100 ml distilled water	300 W, Xe lamp, ≥420 nm	101.4, no notable activity decay after 100 h reaction, 1.4% 420 nm	124
CCN	1 wt% Pt	50 mL of TEOA (10 vol%)	300 W, Xe lamp, 420–780 nm	1356.0, no significant variation after 5 cycles (3 h per cycle), 11.4% 420 nm	96
Zn-doped PHI-based CCN	3 wt% Pt	100 mL of methanol (10 vol%)	300 W, Xe lamp, >420 nm	1500.0, retained in 4 cycles (4 h per cycle), 12.6% 420 nm	130
N-GQDs /PTI/ZnO-QDs	3 wt% Pt	100 mL of TEOA (10 vol%)	300 W, Xe lamp, ≥420 nm	1360.0, maintained for 4 cycles (3 h per cycle), 3.37% 420 nm	165
Cyanamide defect-CCN	3 wt% Pt	80 mL of TEOA (10 vol%)	300 W, Xe lamp, ≥420 nm	2690.0, maintained for 4 cycles (5 h per cycle), 42.0% 420 nm	135
Defective CCN/$ZnIn_2S_4$	1 wt% Pt	100 mL of TEOA (20 vol%)	300 W, Xe lamp, ≥420 nm	1650.0, retained in 3 runs (6 h per run), 18.2% 420 nm	166
Nitrogen vacancy modified CCN	2 wt% Pd	100 mL of methanol (10 vol%)	300 W, Xe lamp, >420 nm	552.7, no significant decrease in activity after 5 cycles (3 h per cycle), N/A	144
WOx/CCN	N/A	100 mL of TEOA (10 vol%)	300 W, Xe lamp, >420 nm	2180.0, remained basically stable after 4 cycles (3 h per cycle), N/A	168
CCN nanosheets	0.5 wt% Pt	20 mL of TEOA (10 vol%)	300 W, Xe lamp, >420 nm	830.0, slight decrease in activity after 4 cycles (4 h per cycle), N/A	205
CCN	1 wt% Pd/SiO_2	5 mol L^{-1} of ethanol, 3 mol L^{-1} of lactic acid	1000 W, Xe lamp, >400 nm	520.0, N/A, 22% 405 nm	206
CCN	3 wt% Pt	80 mL of TEOA (10 vol%)	350 W, Xe lamp	683.54, no obvious decrease in activity after 4 cycles (3 h per cycle), 6.6% 420 nm	207
CCN	0.5 wt% Pt	20 mL of TEOA (15 vol%)	300 W, Xe lamp, ≥420 nm	2025.0, N/A, N/A	90
Heptazine-/triazine-based CCN	3 wt% Pt	80 mL of TEOA (10 vol%)	350 W, Xe lamp	890.0, no obvious activity decay after 4 cycles (3 h per cycle), 26.7% 420 nm	161
KPCN	1 wt% Pt	150 mL of TEOA (10 vol%)	300 W, Xe lamp, 420–780 nm	1188.0, slightly decrease in activity after 4 cycles (3 h per cycle), 8.6% 420 ± 5 nm	208
CCN	3 wt% Pt	100 mL of TEOA (10 vol%)	300 W, Xe lamp, >420 nm	339.4, no significant decrease in activity after 5 cycles (4 h per cycle), 3.8% 420 nm	209
CCN nanosheet	3 wt% Pt	100 mL of TEOA (10 vol%)	300 W, Xe lamp, >420 nm	4060.0, almost no change in activity after 4 runs (4 h per run), N/A	116
CCN with box-shape	1mL $H_2PtCl_6 \cdot 6H_2O$ solution	100 mL of TEOA (10 vol%)	300 W, Xe lamp	1948.0, no noticeable decrease in activity after 3 cycles (4 h per cycle), 2.09% 420 nm	122
Porous CCN	1 wt% Pt	80 mL of lactic acid (10 vol%)	four LED lights 3 W 420 nm	1010.0, highly stable during the 4 cycles (2 h per cycle), 1.56% 420 nm	119
K^+ and cyano-group co-doped CCN	3 wt% Pt	50 ml of TEOA (10 vol%)	300 W, Xe lamp, >420 nm	4125.0, no significant change in activity after 3 cycles (4 h per cycle), N/A	210
PTI/Li^+Cl^-	1 wt% Pt 0.5 wt% Co	100 ml deionized water	300 W, Xe lamp, >300 nm	1890.0, stable after 96 h reaction, 8.0% 365 nm	106
Cyano-group modified CCN	1 wt% Pt	80 mL of lactic acid (10 vol%)	Four LED lights 3 W 420 nm	758.8, stable during cycle tests, 1.17% 420 nm	120
CCN hollow spheres	3 wt% Pt	80 mL of bisphenol A (10 mg L^{-1})	350 W, Xe lamp	151.2, no significant decrease in activity after 4 cycles (3 h per cycle), 1.53% 420 nm	125
O and K co-doped CCN	3 wt% Pt	50 mL of TEOA (20 vol%)	300 W, Xe lamp, >420 nm	7844.0, no obvious decrease in activity after 6 cycles (5 h per cycle), 20.5% 420 nm	211
K-doped CCN	3 wt% Pt	50 mL of TEOA (20 vol%)	300 W, Xe lamp, >420 nm	5238.0, 8.4% decrease in activity after 5 cycles (2 h per cycle), 25.7% 420 nm	212
Nanostructured K-PHI	3 wt% Pt	100 mL of TEOA (10 vol%)	300 W, Xe lamp	2161.0, stable in initial 2 cycles but significantly decrese in the third cycle, 2.32% 420 nm	213
Ultrathin CCN with D–A structure	3 wt% Pt	100 mL of TEOA (20 vol%)	300 W, Xe lamp, >420 nm	5442.74, no obvious change in activity after 8 runs within 40 h, 23.3% 420 nm	214
Na-PHI	8 wt% Pt	10 mL of methanol (10 vol%)	300 W, Xe lamp AM1.5 G	2400 ± 100, N/A, N/A	194
Hierarchical CCN arrays	3 wt% Pt	50 mL of TEOA (20 vol%)	300 W, Xe lamp, >420 nm	758.8, stable during 5 cycles (5 h per cycle), 60.0% 420 nm	215
K-PHI/$B_{0.8}$ST	1 wt% Pt	100 mL of TEOA (20 vol%)	300 W, Xe lamp, >420 nm	1087.4, no obvious decay in activity after 4 cycles (4 h per cycle), 8.05% 420 nm	173

Table 2 (*continued*)

Photocatalysts	Cocatalyst	Reactant solution	Light source	Activity (μmol g^{-1} h^{-1}), stability and quantum efficiency	Ref.
CCN homojunction	3 wt% Pt	100 mL of TEOA (10 vol%)	300 W, Xe lamp, >420 nm	3550.2, no significant decrease in activity after 4 cycles (3 h per cycle), 25.0% 420 nm	216
K^+ implanted CCN	3 wt% Pt	50 ml of TEOA (10 vol%)	300 W, Xe lamp, 420–780 nm	4008.0, 11% decrease in activity after 5 cycles (2 h per cycle), 26.1% 420 nm	217
Single atom Co loaded on CCN	1 wt% Pt	20 ml of lactic acid (20 vol%)	300 W, Xe lamp, ≥420 nm	32 100.0, slight decrease in activity after 12 h reaction, 49.5% 420 nm	218
Carbon fiber/CCN	1 wt% Pt	100 mL of TEOA (10 vol%)	3 W LED light, 420 nm	6398.0, slight decrease in activity after 4 cycles (2 h per cycle), 3.88% 420 nm	219
single-atom Co coordinated CCN/PTI	1 wt% Pt	30 mL of TEOA (10 vol%)	300 W, Xe lamp, >420 nm	3538.0, no obvious change in activity after 8 cycles (3 h per cycle), 20.88% 430 nm	220
Red CCN nanosheet	1.1 wt% Pt	33 mL of TEOA (10 vol%)	300 W, Xe lamp, >420 nm	14 665.0, N/A, N/A	221
ReS_2/CCN	3 wt% Pt	100 mL of TEOA (10 vol%)	300 W, Xe lamp, >420 nm	3460.0, slightly decrease in activity after 3 cycles (5 h per cycle), 5.42% 400 nm	222
MC-CN	3 wt% Pt	100 mL of TEOA (10 vol%)	300 W, Xe lamp, >420 nm	181.51, no apparent activity decay after 5 cycles (3 h per cycle), 3.26% 400 nm	129
Ca and K co-doped CCN	3 wt% Pt	50 mL of TEOA (10 vol%)	300 W, Xe lamp, >420 nm	5190.0, 9.7% decrease in activity after 4 cycles (5 h per cycle), 31.2% 420 nm	131
PHI/PTI	3 wt% Pt	100 mL of TEOA (10 vol%)	300 W, Xe lamp, >420 nm	6970.0, slight decrease in activity after 12 runs (4 h per run), 42.0% 420 nm	162

selectivity for photocatalytic CO_2 reduction. In order to deal with these challenges, some key factors need to be considered, such as light absorption, CO_2 adsorption and activation, separation and transfer of charges, and products desorption.

It is well known that improving light absorption is essential for enhancing photocatalytic performance. Wang and co-workers synthesized PHI-based CCN through the molten salt approach using a new stable monomer with high nitrogen content (5-aminotetrazole).[201] The molten salt method could modulate the crystallinity, grain boundary structure and chemical property to improve the light absorption. Due to the well-constructed PHI structure, improved light absorption and optimized electronic properties, the CCN exhibited excellent photocatalytic performance.

From the viewpoint of thermodynamics, transferring the first electron to the CO_2 molecule to activate CO_2 is indeed unfavorable due to a very negative reduction potential of 1.9 V (see eqn (1)). Therefore, improving the CO_2 activation ability of CCNs is an efficient approach to enhance the photocatalytic activity.[88,184,224] Based on the above discussion, our group designed a defect-modified CCN to improve the performance of photocatalytic CO_2 reduction.[224] As shown in Fig. 18c, HRTEM image reveals clear lattice fringes with a d spacing of 1.03 nm, confirming the high crystallinity, suggesting that the crystallinity was well maintained by KOH treatment. The CO_2 temperature-programmed desorption measurement (Fig. 18d) showed that the desorption peak shifted to a higher temperature, suggesting that the defect was beneficial to the adsorption and activation of CO_2, thus lowering the activation energy barrier. The defect-modified CCN exhibited better photocatalytic performance than CCN due to the high crystallinity and optimal activation sites.

The selectivity of the CO_2 photoreduction reaction products is influenced by CO_2 adsorption. For example, our group found that the cyano and carboxyl groups not only greatly enhanced the adsorption and activation of CO_2, but also improved the charge transfer.[88] Due to the strong chemisorption of CO_2, the defective CCN exhibited good photocatalytic CO_2 reduction performance with a total generation rate of 12.07 μmol h^{-1} g^{-1} and selectivity (91.5%), which was better than most previously reported CN photocatalysts. Xiang and co-workers prepared a single Cu atom/CCN photocatalyst (Cu–CCN) by molten salt and reflux approach.[184] The introduction of single Cu atoms served as reaction centers for CO_2 adsorption and activation. DFT calculation revealed that the reduction of CO_2 to CO is an energy favorable reaction compared with the CO_2 reduction to CH_4. Consequently, the Cu–CCN presented improved photocatalytic CO_2 reduction activity and high selectivity (nearly 100%) for the conversion of CO_2 to CO. Taking advantage of CO_2 adsorption and charge transfer, Liu and co-workers developed tungsten doped CCN by solvothermal method for CO_2 conversion.[225] Owning to the synergetic modulation of photogenerated electron capture and enrichment, as well as the adsorption and activation of CO_2 and CO intermediates, the W-doped CCN showed excellent photocatalytic CO_2 reduction performance and high selectivity for hydrocarbons.

The effective separation of photoexcited charge carriers is beneficial to improve the photocatalytic CO_2 reduction activity.[226]

Furthermore, considering that the CO_2 reduction is a multi-electron involved process, coupling the cocatalyst, such as graphene, and single atom to promote the transfer and collection of electrons is an efficient strategy to improve the CO_2 reduction performance. For instance, our group constructed a 1D/2D heterojunction (CNNA/rGO) of CCN nanoarrays (CNNA) aligned on 2D graphene sheet through an ionothermal method.[175] Due to the heterojunction effect and ordered 1D structure, the CNNA/rGO exhibited greatly improved CO_2 adsorption capacity. Moreover, the charge transfer and accumulation were greatly improved after the introduction of rGO. The CNNA/rGO exhibited efficient photocatalytic reduction performance due to the selective CO_2 binding, improved charge transport, enhanced light absorption as well as promoted exciton splitting. Xiang and co-workers designed dual-single-atoms of Pt–Cu on N-vacancy-rich CCN for efficient and selective CO_2 reduction.[227] The dual single atoms not only integrated the advantages of platinum and copper atoms, but also promoted the charge transfer and migration.

The conventional reaction system discussed above usually couples CO_2 reduction half-reaction with pure water oxidation half-reaction. However, the water oxidation half-reaction suffers from sluggish kinetics and large overpotential, resulting in low catalytic efficiency. Therefore, replacing the H_2O oxidation half-reaction with a thermodynamically favorable organic synthesis to simultaneously produce two valuable chemicals is an attractive approach compared with the conventional CO_2 reduction system. For instance, Sun and co-workers proposed the co-doping of K and S into CCN through a salt-template-assisted incorporation approach for simultaneous photoreforming of biomass and CO_2 reduction.[133] The K and S co-doping could improve the visible-light absorption and accelerate the charge transport and separation. Consequently, the K and S co-doped CCN presented superior photocatalytic performance with a CO generation rate of 16.27 $\mu mol\ g^{-1}\ h^{-1}$ and lactic acid yield (78.07%).

6.3. Photocatalytic degradation of pollutants

With the rapid development of industrialization and population growth, a large amount of toxic and hazardous pollutants has been released into the environment, posing a great threat to human health and the ecological environment. In order to achieve the sustainable development of human society, photocatalytic degradation of pollutants has been demonstrated to be a promising green approach to address the environmental problems. The mechanism of photocatalytic degradation is as follows. Under light irradiation, photogenerated electrons could reduce the O_2 adsorbed on the surface of photocatalyst to generate superoxide radicals ($^{\bullet}O_2^-$), which would contribute to the formation of $^{\bullet}OH$ radicals, $^1O_2$, and H_2O_2. Meanwhile, in some cases, the photoexcited holes may react with OH^- on the surface to generate $^{\bullet}OH$ radicals. These main active species (e^-, h^+, $^{\bullet}O_2^-$, $^1O_2$, H_2O_2, $^{\bullet}OH$) in the above process could oxidize organic pollutants into CO_2 and H_2O.

Recently, the CCNs-based photocatalysts have been proved to be effective in degrading various pollutants, including rhodamine B (RhB),[151,152,168,171,228–232] methylene blue (MB),[160,229,233] methyl orange (MO),[98] phenol,[98,229] tetracycline,[172,234] pharmaceuticals and personal care products,[235] 17α-ethinylestradiol,[236] soluble U(VI).[237] For instance, Liang and co-workers reported that the tetragonal CCN hollow tubes exhibited efficient photocatalytic activity in degrading methylene blue and phenol, which could be attributed to the high crystallinity, unique one-dimensional hollow structure and large specific surface area.[229] Li and co-workers investigated the photocatalytic degradation of pharmaceuticals and personal care products (PPCPs) by CCN.[235] They proposed the route of direct two-electron reduction on the CCN surface to produce H_2O_2 and subsequent conversion to $^{\bullet}OH$ radicals, rather than the conventional single-electron reduction reaction on bulk CN. Due to the improved charge separation and electron transfer ability, the CCN exhibited superior photocatalytic activity towards PPCPs-type pollutants. To obtain an effective charge separation ability, Guo and co-workers fabricated a CoP/CCN composite photocatalyst *via* a facile solvothermal approach for the photodegradation of tetracycline.[172] HRTEM image confirms the high crystallinity, suggesting reduced structural defects. Furthermore, CoP acted as the cocatalyst to accelerate the separation of the charge carriers. As a result, the designed composites showed superior photocatalytic performance. The photocatalytic reduction of soluble U(VI) around the clock was achieved by using K^+ and cyano group co-modified PHI.[237] The K^+ could stabilize the electrons and generate long-lived radicals, enabling the photocatalytic reduction of U(VI) in the dark. Besides the photocatalytic degradation of pollutants in the liquid phase, CCN have also been intensively investigated for the photocatalytic removal of gas phase pollutants, including NO[238,239] and CH_3SH.[97] For instance, Wang and co-workers prepared in-plane highly ordered CCN nanosheets (PCNNs-IHO) through on-surface polymerization approach for the mineralization of CH_3SH (Fig. 18e).[97] As revealed by the HRTEM image, a clear lattice spacing of 1.07 nm corresponding to the in-plane stacking was observed, suggesting the enhanced in-plane ordering (Fig. 18f). Moreover, the NaCl not only acted as unique support to guide the assembly of two-dimension nanosheets, but also served as a reactant to afford Na^+ incorporation to obtain structural base sites. Owning to the structural basicity, the PCNNs-IHO showed excellent photocatalytic performance for the mineralization of CH_3SH to SO_4^{2-} (Fig. 18g).

The aforementioned work demonstrated that the CCNs-based photocatalysts presented outstanding photocatalytic degradation performance since their high crystallinity could effectively separate and transfer the charge carriers.

6.4. Photocatalytic organic synthesis

Solar-driven organic transformation is a promising technology for the synthesis of many important compounds. Recently, CCNs-based photocatalysts for selective organic synthesis under mild conditions have been intensively investigated. For example, Huang and co-workers demonstrated that a conversion rate of 5.81% from cyclohexane to cyclohexanone and a selectivity over 99.9% could be achieved by using the PTI as a photocatalyst without any other oxidants, initiators or solvents.[240] Wang and co-workers reported that the conversion of benzyl alcohol to

benzaldehyde with 90% selectivity was achieved using CCN as a photocatalyst to activate O_2.[241] This enhanced photocatalytic activity could be ascribed to the synergistic effect of effective electron–hole separation and increased surface reaction kinetics. Su and co-workers reported the selective deuteration of alkenes and alkynes by the *in situ* generated D-species in heavy water splitting using Pd nanoparticles modified KPCN.[95] Pieber and co-workers coupled Ni catalyst with CN-OA-m photocatalyst for selective C–O cross-couplings of carboxylic acids with aryl halides.[242] As a continuation of the above research, the same group further extended this method to dual nickel/photocatalytic C–O coupling.[243] Hu and co-workers designed CCN with surface nitrogen vacancies and cyano groups for isomerization of glucose to fructose with a selectivity of 60%.[244] Wang and co-workers reported the preparation of Fe-PHI with atomically dispersed Fe–N_4C active center by ion exchange method for selective C–H bond oxidation to valuable carbonyl compounds.[245] Savateev and co-workers reported a series of research proving the efficient photocatalytic organic conversion on K-PHI photocatalysts, including the selective oxidation of benzyl alcohol to benzaldehyde and 1,4-dihydropyridines to pyridines,[246] oxidative cyclization *N*-acylhydrazones to 1,3,4-oxadiazoles,[247] photocatalytic Kindler reaction,[248] oxidative C–H thiolation of toluenes to dibenzyldisulfanes,[249] cyclodimerization of the chalcones to cyclopentanoles,[250] halogenation of aromatic hydrocarbons,[251] tetrahydroisoquinoline and chalcones to polyaromatic heterocycles,[252] [3+2]-cycloadditions reaction,[253] chromoselective synthesis of sulfonyl chlorides and sulfonamides,[254] and so on. It was found that the conversion and selectivity of benzyl alcohol to benzaldehyde were excellent under relatively mild reaction conditions when elemental sulfur (S_8) and K-PHI were used as sacrificial electron acceptor and photocatalyst, respectively.[246] Recently, Savateev and co-workers described a cascade of energy-transfer reactions for the preparation of various oxadiazoles-1,2,4 and isoxazoles *via* dipolar [3+2]-cycloaddition.[253] The crystal structure of the potassium poly(heptazine imide) (K-PHI) was refined by the XRD data and TEM image (Fig. 19a and b). The high crystallinity was confirmed by the HRTEM image (Fig. 19c). Interestingly, once excited with visible light, the K-PHI could undergo crossover between singlet–triplet intersystem, thereby providing a reasonably long-lived triplet excited state. Then, the triplet excited states could sensitize singlet oxygen ($^1O_2$), and, in turn, employ $^1O_2$ as a starting point for the preparation of up to 25 different N-rich heterocycles (Fig. 19d). Moreover, the same group reported the selective synthesis of three different products (arylchlorides, sulfonyl chlorides and diaryldisulfides) from S-arylthioacetates by changing the excitation light, using K-PHI as the catalyst (Fig. 19e).[254] The mechanism of the chromoselective oxidation reaction is presented in Fig. 19f. Specifically, the diaryldisulfides was produced by the green or red light irradiation, which was not sufficient to separate excitons and only participated in the energy transfer to O_2. The formation of sulfenyl chloride was achieved by the blue light irradiation, enabling electron transfer to O_2 and thioacetate. When irradiated with 365 or 410 nm light, the two-electron oxidation of Cl^- occurred and resulted in the over-chlorination of sulfenyl chloride, which was unstable and decomposed to chlorobenzene.

6.5. Photocatalytic hydrogen peroxide (H_2O_2) production

H_2O_2 is a valuable and mild oxidizing chemical extensively used in paper bleaching, environmental remediation, sterilization, energy conversion/storage, and fine chemical synthesis.[255,256] The conventional and prevailing method for industrial production of hydrogen peroxide is the anthraquinone process, which requires intense energy consumption and produces hazardous waste. Therefore, it is highly desirable to develop an eco-friendly and sustainable route for H_2O_2 synthesis. Photocatalytic production of H_2O_2 from H_2O and O_2 is a green and attractive approach because it requires only renewable sunlight as the energy input. The process of artificial photosynthesis of H_2O_2 could be divided into the five main routes[257–261] (Fig. 20): (I) The direct two-electron O_2 reduction process, (II) sequential single-electron O_2 reduction route, (III) sequential electrons and holes transfer pathway, (IV) the direct two-electron H_2O oxidation reaction, (V) sequential single-electron H_2O oxidation pathway. Therefore, the possible intermediates and corresponding redox potentials (*versus* normal hydrogen electrode (NHE) at pH = 0) for the production of H_2O_2 *via* different pathways are presented in eqn (9)–(14).[262]

$$O_2 + e^- \rightarrow {}^\bullet O_2^- \quad E^0_{redox} = -0.33\ V \tag{9}$$

$${}^\bullet O_2^- + 2H^+ + e^- \rightarrow H_2O_2 \quad E^0_{redox} = +1.44\ V \tag{10}$$

$${}^\bullet O_2^- + h^+ \rightarrow {}^1O_2 \quad E^0_{redox} = +0.34\ V \tag{11}$$

$$O_2 + 2H^+ + 2e^- \rightarrow H_2O_2 \quad E^0_{redox} = +0.68\ V \tag{12}$$

$$H_2O + 2h^+ \rightarrow H^+ + {}^\bullet OH \quad E^0_{redox} = +2.73\ V \tag{13}$$

$$2H_2O + 2h^+ \rightarrow H_2O_2 + 2H^+ \quad E^0_{redox} = -1.76\ V \tag{14}$$

Recently, CCNs-based photocatalysts have emerged as a candidate for efficient artificial photosynthesis of H_2O_2.[263–265] For instance, Yu and co-workers fabricated ion-intercalated CCN (CN-KCl/KI) through a facile ionothermal approach for photosynthesis of H_2O_2.[266] The ionothermal method not only enhanced the crystallinity of CN, but also resulted in the intercalation of K^+ and I^-. The doping of I^- reduces the band gap and improves the light absorption. While the intercalation of K^+ not only accelerates the interlayer carrier transport and separation, but also enhances the selectivity for the two-electron O_2 reduction pathway. Benefiting from the synergistic effect of crystallinity tuning and dual doping engineering, the CN-KCl/KI shows an excellent H_2O_2 generation rate of 13.1 mmol g^{-1} h^{-1} at 400 nm with the AQY of 23.6%.

7. Conclusion and outlook

In conclusion, CCNs have been a popular research topic in photocatalysis due to their extraordinary features such as high photogenerated carrier transfer capacity, improved light absorption ability and low electron–hole pair recombination rate. In this review, we summarized the recent developments of CCNs and

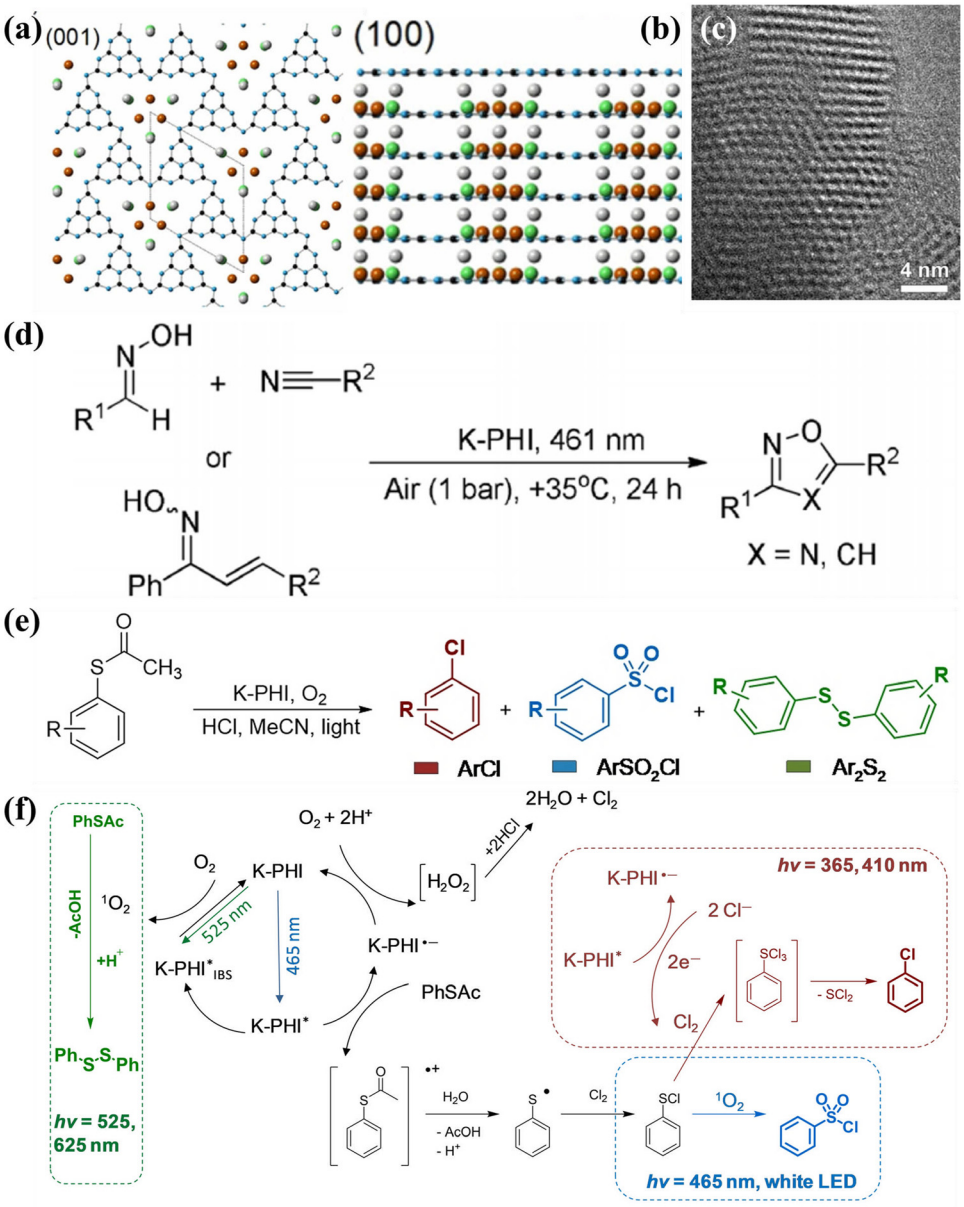

Fig. 19 (a) and (b) Crystal structure of KPHI revealed by the XRD data. (c) HRTEM image of K-PHI. (d) Photocatalytic synthesis of oxadiazoles-1,2,4 and isoxazoles. Reproduced with permission.[253] Copyright 2020, Wiley-VCH. (e) Three possible products of S-arylthioacetates oxidation by K-PHI. (f) The chromoselective oxidation mechanism for the production of sulfonyl chlorides, arylchlorides, and disulfides from thio-derivatives. Reproduced with permission.[254] Copyright 2021, Wiley-VCH.

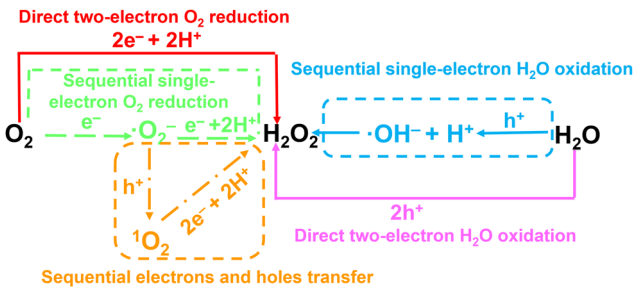

Fig. 20 Reaction pathways of the photosynthesis of H_2O_2 through the O_2 reduction or H_2O oxidation reaction.

CCNs-based photocatalysts, focusing on the preparation methods and design of such photocatalysts with remarkably improved photocatalytic performance and high photogenerated carrier separation capability. This review discusses the preparation of CCNs based on high-temperature and high-pressure routes, simple ionothermal (molten salt) approach, solvothermal method and microwave-assisted heating synthesis. The applications of CCNs-based photocatalysts in the field of solar energy conversion, such as photocatalytic water splitting, photocatalytic CO_2 reduction, photocatalytic pollutant degradation, photocatalytic organic synthesis and photocatalytic H_2O_2 production, are introduced. Despite the above significant progress in CCNs-based

photocatalysts, there are still several important challenges to be addressed:

(1) During the synthesis of CCNs by ionothermal (molten salt) method, ions could be used as a ''template'' to induce different morphologies, but the deep mechanism is still unclear and more experiments and discussions should be conducted.

(2) The applications of CCN prepared by the solvothermal and microwave-assisted thermal synthesis route are relatively isolated.

(3) Although the crystallinity and visible light utilization have been significantly improved, the specific surface area of CCN is low and the exposed active sites are limited.

(4) More attention should be paid to the template, supramolecular chemistry strategy and solvothermal approach to tune the morphology and microstructure. There is an urgent need to develop more supramolecular precursors to synthesize CCN with various nanostructures.

(5) Even though the performance of CCNs-based photocatalysts has been greatly improved, the enhancement mechanism is not deep and specific enough. Some characterization techniques and DFT calculations should be applied in this field, such as surface photo-voltage microscopy (SPVM), Kelvin probe force microscopy (KPFM) and calculation of built-in electric field.

(6) The surface functionalization of CCNs needs to be further explored to optimize photocatalytic performance.

(7) To further advance the performance of photocatalytic reduction of CO_2, a more comprehensive understanding of the reaction process is necessary. From this perspective, *in situ*/*operando* techniques would be extremely useful tools to investigate the reaction process and intermediates. For instance, *in situ* Fourier transform infrared spectroscopy (FTIR) and operando Raman can uncover the intermediates of the reaction.

(8) Although the ionothermal (molten salt) method is an effective approach for large-scale production of CCNs, other efficient synthesis methods need to be further explored. Moreover, compared with metal-based photocatalysts, the CCNs would be suitable for photocatalytic reactions in seawater, including the production of H_2 and H_2O_2 in seawater.

Conflicts of interest

The authors declare no conflict of interest.

Acknowledgements

This work was financially supported by the National Key R&D Program of China (2022YFE0114800), and the National Natural Science Foundation of China (22278324 and 52073223).

References

1 A. Fujishima and K. Honda, *Nature*, 1972, **238**, 37–38.
2 Y. Fang, Y. Zheng, T. Fang, Y. Chen, Y. Zhu, Q. Liang, H. Sheng, Z. Li, C. Chen and X. Wang, *Sci. China: Chem.*, 2020, **63**, 149–181.
3 P. Kuang, M. Sayed, J. Fan, B. Cheng and J. Yu, *Adv. Energy Mater.*, 2020, **10**, 1903802.
4 Z. Wang, C. Li and K. Domen, *Chem. Soc. Rev.*, 2019, **48**, 2109–2125.
5 M. L. Marin, L. Santos-Juanes, A. Arques, A. M. Amat and M. A. Miranda, *Chem. Rev.*, 2012, **112**, 1710–1750.
6 C. Yang, B. Cheng, J. Xu, J. Yu and S. Cao, *EnergyChem*, 2023, DOI: 10.1016/j.enchem.2023.100116.
7 Y. Ma, X. Wang, Y. Jia, X. Chen, H. Han and C. Li, *Chem. Rev.*, 2014, **114**, 9987–10043.
8 A. Meng, L. Zhang, B. Cheng and J. Yu, *Adv. Mater.*, 2019, **31**, 1807660.
9 H. Li, Q. Song, S. Wan, C.-W. Tung, C. Liu, Y. Pan, G. Luo, H. M. Chen, S. Cao, J. Yu and L. Zhang, *Small*, 2023, **19**, 2301711.
10 X. Zhou, Q. Xu, W. Lei, T. Zhang, X. Qi, G. Liu, K. Deng and J. Yu, *Small*, 2014, **10**, 674–679.
11 E. S. Jang, J.-H. Won, S.-J. Hwang and J.-H. Choy, *Adv. Mater.*, 2006, **18**, 3309–3312.
12 S. Cao, B. Shen, T. Tong, J. Fu and J. Yu, *Adv. Funct. Mater.*, 2018, **28**, 1800136.
13 R. Li, F. Zhang, D. Wang, J. Yang, M. Li, J. Zhu, X. Zhou, H. Han and C. Li, *Nat. Commun.*, 2013, **4**, 1432.
14 C. Bie, B. Zhu, F. Xu, L. Zhang and J. Yu, *Adv. Mater.*, 2019, **31**, 1902868.
15 T. Di, Q. Xu, W. Ho, H. Tang, Q. Xiang and J. Yu, *ChemCatChem*, 2019, **11**, 1394–1411.
16 X. Wang, K. Maeda, A. Thomas, K. Takanabe, G. Xin, J. M. Carlsson, K. Domen and M. Antonietti, *Nat. Mater.*, 2009, **8**, 76–80.
17 W.-J. Ong, L.-L. Tan, Y. H. Ng, S.-T. Yong and S.-P. Chai, *Chem. Rev.*, 2016, **116**, 7159–7329.
18 Y. Zheng, L. Lin, B. Wang and X. Wang, *Angew. Chem., Int. Ed.*, 2015, **54**, 12868–12884.
19 Y. Fang and X. Wang, *Chem. Commun.*, 2018, **54**, 5674–5687.
20 J. Fu, J. Yu, C. Jiang and B. Cheng, *Adv. Energy Mater.*, 2018, **8**, 1701503.
21 A. Savateev, I. Ghosh, B. Koenig and M. Antonietti, *Angew. Chem., Int. Ed.*, 2018, **57**, 15936–15947.
22 H. Li, S. Tao, S. Wan, G. Qiu, Q. Long, J. Yu and S. Cao, *Chin. J. Catal.*, 2023, **46**, 167–176.
23 L. Lin, Z. Yu and X. Wang, *Angew. Chem., Int. Ed.*, 2019, **58**, 6164–6175.
24 Z. Zhou, Y. Zhang, Y. Shen, S. Liu and Y. Zhang, *Chem. Soc. Rev.*, 2018, **47**, 2298–2321.
25 G. Liao, Y. Gong, L. Zhang, H. Gao, G.-J. Yang and B. Fang, *Energy Environ. Sci.*, 2019, **12**, 2080–2147.
26 Y. Wang, S. Z. F. Phua, G. Dong, X. Liu, B. He, Q. Zhai, Y. Li, C. Zheng, H. Quan, Z. Li and Y. Zhao, *Chem*, 2019, **5**, 2775–2813.
27 A. Savateev and M. Antonietti, *ChemCatChem*, 2019, **11**, 6166–6176.
28 B. Yan, Z. Chen and Y. Xu, *Chem. – Asian J.*, 2020, **15**, 2329–2340.
29 J. Liebig, *Ann. Pharm.*, 1834, **10**, 1–47.

30 E. C. Franklin, *J. Am. Chem. Soc.*, 1922, **44**, 486–509.
31 L. Pauling and J. H. Sturdivant, *Proc. Natl. Acad. Sci. U. S. A.*, 1937, **23**, 615–620.
32 C. E. Redemann and H. J. Lucas, *J. Am. Chem. Soc.*, 1940, **62**, 842–846.
33 A. Y. Liu and M. L. Cohen, *Science*, 1989, **245**, 841–842.
34 D. M. Teter and R. J. Hemley, *Science*, 1996, **271**, 53–55.
35 D. C. Nesting and J. V. Badding, *Chem. Mater.*, 1996, **8**, 1535–1539.
36 A. Y. Liu and R. M. Wentzcovitch, *Phys. Rev. B: Condens. Matter Mater. Phys.*, 1994, **50**, 10362–10365.
37 J. Ortega and O. F. Sankey, *Phys. Rev. B: Condens. Matter Mater. Phys.*, 1995, **51**, 2624–2627.
38 J. E. Lowther, *Phys. Rev. B: Condens. Matter Mater. Phys.*, 1999, **59**, 11683–11686.
39 M. Kawaguchi and K. Nozaki, *Chem. Mater.*, 1995, **7**, 257–264.
40 Y. Wang, X. Wang and M. Antonietti, *Angew. Chem., Int. Ed.*, 2012, **51**, 68–89.
41 X. Wang, S. Blechert and M. Antonietti, *ACS Catal.*, 2012, **2**, 1596–1606.
42 E. Kroke, M. Schwarz, E. Horath-Bordon, P. Kroll, B. Noll and A. D. Norman, *New J. Chem.*, 2002, **26**, 508–512.
43 J. Sehnert, K. Baerwinkel and J. Senker, *J. Phys. Chem. B*, 2007, **111**, 10671–10680.
44 E. Horvath-Bordon, E. Kroke, I. Svoboda, H. Fuess and R. Riedel, *New J. Chem.*, 2005, **29**, 693–699.
45 T. Komatsu and T. Nakamura, *J. Mater. Chem.*, 2001, **11**, 474–478.
46 M. J. Bojdys, J.-O. Mueller, M. Antonietti and A. Thomas, *Chem. – Eur. J.*, 2008, **14**, 8177–8182.
47 B. Jurgens, E. Irran, J. Senker, P. Kroll, H. Muller and W. Schnick, *J. Am. Chem. Soc.*, 2003, **125**, 10288–10300.
48 A. Sattler, S. Pagano, M. Zeuner, A. Zurawski, D. Gunzelmann, J. Senker, K. Mueller-Buschbaum and W. Schnick, *Chem. – Eur. J.*, 2009, **15**, 13161–13170.
49 B. V. Lotsch and W. Schnick, *Chem. Mater.*, 2006, **18**, 1891–1900.
50 B. V. Lotsch and W. Schnick, *Chem. – Eur. J.*, 2007, **13**, 4956–4968.
51 T. Komatsu, *J. Mater. Chem.*, 2001, **11**, 799–801.
52 T. Komatsu, *J. Mater. Chem.*, 2001, **11**, 802–805.
53 F. Goettmann, A. Fischer, M. Antonietti and A. Thomas, *Angew. Chem., Int. Ed.*, 2006, **45**, 4467–4471.
54 F. Goettmann, A. Fischer, M. Antonietti and A. Thomas, *Chem. Commun.*, 2006, 4530–4532.
55 M. Doblinger, B. V. Lotsch, J. Wack, J. Thun, J. Senker and W. Schnick, *Chem. Commun.*, 2009, 1541–1543.
56 S. C. Yan, Z. S. Li and Z. G. Zou, *Langmuir*, 2009, **25**, 10397–10401.
57 D. R. Miller, J. J. Wang and E. G. Gillan, *J. Mater. Chem.*, 2002, **12**, 2463–2469.
58 E. G. Gillan, *Chem. Mater.*, 2000, **12**, 3906–3912.
59 Y. Zhang, A. Thomas, M. Antonietti and X. Wang, *J. Am. Chem. Soc.*, 2009, **131**, 50–51.
60 Z. Zhou, J. Wang, J. Yu, Y. Shen, Y. Li, A. Liu, S. Liu and Y. Zhang, *J. Am. Chem. Soc.*, 2015, **137**, 2179–2182.
61 H. Gao, S. Yan, J. Wang, Y. A. Huang, P. Wang, Z. Li and Z. Zou, *Phys. Chem. Chem. Phys.*, 2013, **15**, 18077–18084.
62 Q. Deng, H. Li, W. Hu and W. Hou, *Angew. Chem., Int. Ed.*, 2023, **62**, e202314213.
63 M. Deifallah, P. F. McMillan and F. Cora, *J. Phys. Chem. C*, 2008, **112**, 5447–5453.
64 Y. Ham, K. Maeda, D. Cha, K. Takanabe and K. Domen, *Chem. – Asian J.*, 2013, **8**, 218–224.
65 K. Schwinghammer, M. B. Mesch, V. Duppel, C. Ziegler, J. Senker and B. V. Lotsch, *J. Am. Chem. Soc.*, 2014, **136**, 1730–1733.
66 X. Wang, K. Maeda, X. Chen, K. Takanabe, K. Domen, Y. Hou, X. Fu and M. Antonietti, *J. Am. Chem. Soc.*, 2009, **131**, 1680–1681.
67 C. M. Niu, Y. Z. Lu and C. M. Lieber, *Science*, 1993, **261**, 334–337.
68 K. M. Yu, M. L. Cohen, E. E. Haller, W. L. Hansen, A. Y. Liu and I. C. Wu, *Phys. Rev. B: Condens. Matter Mater. Phys.*, 1994, **49**, 5034–5037.
69 Z. M. Ren, Y. C. Du, Y. X. Qiu, J. D. Nu, Z. F. Ying, X. X. Xiong and F. M. Li, *Phys. Rev. B: Condens. Matter Mater. Phys.*, 1995, **51**, 5274–5277.
70 Z. J. Zhang, S. S. Fan and C. M. Lieber, *Appl. Phys. Lett.*, 1995, **66**, 3582–3584.
71 Y. F. Zhang, Z. H. Zhou and H. L. Li, *Appl. Phys. Lett.*, 1996, **68**, 634–636.
72 I. Alves, G. Demazeau, B. Tanguy and F. Weill, *Solid State Commun.*, 1999, **109**, 697–701.
73 Z. H. Zhang, K. Leinenweber, M. Bauer, L. A. J. Garvie, P. F. McMillan and G. H. Wolf, *J. Am. Chem. Soc.*, 2001, **123**, 7788–7796.
74 J. Kouvetakis, A. Bandari, M. Todd, B. Wilkens and N. Cave, *Chem. Mater.*, 1994, **6**, 811–814.
75 E. Horvath-Bordon, R. Riedel, P. F. McMillan, P. Kroll, G. Miehe, P. A. van Aken, A. Zerr, P. Hoppe, O. Shebanova, I. McLaren, S. Lauterbach, E. Kroke and R. Boehler, *Angew. Chem., Int. Ed.*, 2007, **46**, 1476–1480.
76 E. Wirnhier, M. Doeblinger, D. Gunzelmann, J. Senker, B. V. Lotsch and W. Schnick, *Chem. – Eur. J.*, 2011, **17**, 3213–3221.
77 B. V. Lotsch, M. Doeblinger, J. Sehnert, L. Seyfarth, J. Senker, O. Oeckler and W. Schnick, *Chem. – Eur. J.*, 2007, **13**, 4969–4980.
78 S. Y. Chong, J. T. A. Jones, Y. Z. Khimyak, A. I. Cooper, A. Thomas, M. Antonietti and M. J. Bojdys, *J. Mater. Chem. A*, 2013, **1**, 1102–1107.
79 M. J. Bojdys, N. Severin, J. P. Rabe, A. I. Cooper, A. Thomas and M. Antonietti, *Macromol. Rapid. Commun.*, 2013, **34**, 850–854.
80 H. Montigaud, B. Tanguy, G. Demazeau, I. Alves and S. Courjault, *J. Mater. Sci.*, 2000, **35**, 2547–2552.
81 Y. J. Bai, B. Lu, Z. G. Liu, L. Li, D. L. Cui, X. G. Xu and Q. L. Wang, *J. Cryst. Growth*, 2003, **247**, 505–508.
82 Q. Lv, C. B. Cao, C. Li, J. T. Zhang, H. X. Zhu, X. Kong and X. F. Duan, *J. Mater. Chem.*, 2003, **13**, 1241–1243.
83 Q. X. Guo, Y. Xie, X. J. Wang, S. C. Lv, T. Hou and X. M. Liu, *Chem. Phys. Lett.*, 2003, **380**, 84–87.
84 Q. Luv, C. B. Cao, J. T. Zhang, C. Li and H. S. Zhu, *Appl. Phys. A: Mater. Sci. Process.*, 2004, **79**, 633–636.
85 Y. L. Gu, L. Y. Chen, L. Shi, J. H. Ma, Z. H. Yang and Y. T. Qian, *Carbon*, 2003, **41**, 2674–2676.

86 C. Li, X. Yang, B. Yang, Y. Yan and Y. Qian, *Mater. Chem. Phys.*, 2007, **103**, 427–432.
87 J. Zhang, W. Liu, X. Li, B. Zhan, Q. Cui and G. Zou, *Mater. Res. Bull.*, 2009, **44**, 294–297.
88 P. Xia, M. Antonietti, B. Zhu, T. Heil, J. Yu and S. Cao, *Adv. Funct. Mater.*, 2019, **29**, 1900093.
89 Y.-P. Yuan, L.-S. Yin, S.-W. Cao, L.-N. Gu, G.-S. Xu, P. Du, H. Chai, Y.-S. Liao and C. Xue, *Green Chem.*, 2014, **16**, 4663–4668.
90 Y. Guo, J. Li, Y. Yuan, L. Li, M. Zhang, C. Zhou and Z. Lin, *Angew. Chem., Int. Ed.*, 2016, **55**, 14693–14697.
91 L. W. Yin, Y. Bando, M. S. Li, Y. X. Liu and Y. X. Qi, *Adv. Mater.*, 2003, **15**, 1840–1844.
92 X.-H. Li, J. Zhang, X. Chen, A. Fischer, A. Thomas, M. Antonietti and X. Wang, *Chem. Mater.*, 2011, **23**, 4344–4348.
93 J. Wang, Y. Shen, Y. Li, S. Liu and Y. Zhang, *Chem. – Eur. J.*, 2016, **22**, 12449–12454.
94 S. Kang, L. Zhang, M. He, Y. Zheng, L. Cui, D. Sun and B. Hu, *Carbon*, 2018, **137**, 19–30.
95 C. Qiu, Y. Xu, X. Fan, D. Xu, R. Tandiana, X. Ling, Y. Jiang, C. Liu, L. Yu, W. Chen and C. Su, *Adv. Sci.*, 2019, **6**, 1801403.
96 Y. Xu, X. He, H. Zhong, D. J. Singh, L. Zhang and R. Wang, *Appl. Catal., B*, 2019, **246**, 349–355.
97 F. S. Guo, B. Hu, C. Yang, J. S. Zhang, Y. D. Hou and X. C. Wang, *Adv. Mater.*, 2021, **33**, 2101466.
98 Y.-Y. Li, B.-X. Zhou, H.-W. Zhang, S.-F. Ma, W.-Q. Huang, W. Peng, W. Hu and G.-F. Huang, *Nanoscale*, 2019, **11**, 6876–6885.
99 J. Zhou, Y. Yang and C. Y. Zhang, *Chem. Commun.*, 2013, **49**, 8605–8607.
100 Z. Xing, K. T. Dong, N. Pavlopoulos, Y. X. Chen and L. Amirav, *Angew. Chem., Int. Ed.*, 2021, **60**, 19413–19418.
101 H. Schlomberg, J. Kroger, G. Savasci, M. W. Terban, S. Bette, I. Moudrakovski, V. Duppel, F. Podjaski, R. Siegel, J. Senker, R. E. Dinnebier, C. Ochsenfeld and B. V. Lotsch, *Chem. Mater.*, 2019, **31**, 7478–7486.
102 M. Pauly, J. Kroger, V. Duppel, C. Murphey, J. Cahoon, B. V. Lotsch and P. A. Maggard, *Chem. Sci.*, 2022, **13**, 3187–3193.
103 Y. Lin, M. Zhou, X. Tai, H. Li, X. Han and J. Yu, *Matter*, 2021, **4**, 2309–2339.
104 M. Ma, X. Zhang, L. Xu, X. Chen, L. Wang, T. Cheng, F. Wei, J. Yuan and B. Shen, *Adv. Mater.*, 2023, **35**, 2300653.
105 H. Xiong, H. Wang, X. Chen and F. Wei, *ACS Catal.*, 2023, **13**, 12213–12226.
106 L. Lin, Z. Lin, J. Zhang, X. Cai, W. Lin, Z. Yu and X. Wang, *Nat. Catal.*, 2020, **3**, 649–655.
107 W. Wang, J. Cui, Z. Z. Sun, L. Xie, X. K. Mu, L. M. Huang and J. Q. He, *Adv. Mater.*, 2021, **33**, 2106359.
108 H. Y. Chi, C. L. Chen, K. N. Zhao, L. F. Villalobos, P. A. Schouwink, L. Piveteau, K. P. Marshall, Q. Liu, Y. Han and K. V. Agrawal, *Angew. Chem., Int. Ed.*, 2022, **61**, e202207457.
109 T. S. Miller, T. M. Suter, A. M. Telford, L. Picco, O. D. Payton, F. Russell-Pavier, P. L. Cullen, A. Sella, M. S. P. Shaffer, J. Nelson, V. Tileli, P. F. McMillan and C. A. Howard, *Nano Lett.*, 2017, **17**, 5891–5896.
110 J. Jia, E. R. White, A. J. Clancy, N. Rubio, T. Suter, T. S. Miller, K. McColl, P. F. McMillan, V. Brazdova, F. Cora, C. A. Howard, R. V. Law, C. Mattevi and M. S. P. Shaffer, *Angew. Chem., Int. Ed.*, 2018, **57**, 12656–12660.
111 L. F. Villalobos, M. T. Vandat, M. Khchoune, Z. Nadizadeh, M. Mensi, E. Oveisi, D. Campi, N. Marzari and K. V. Agrawal, *Sci. Adv.*, 2020, **6**, eaay9851.
112 H. Ou, L. Lin, Y. Zheng, P. Yang, Y. Fang and X. Wang, *Adv. Mater.*, 2017, **29**, 1700008.
113 W. Iqbal, B. Qiu, Q. Zhu, M. Xing and J. Zhang, *Appl. Catal., B*, 2018, **232**, 306–313.
114 Y. Wang, X. Hou, J. Zhang, T. Xu, S. Liu and B. Liu, *ChemPhotoChem*, 2018, **2**, 490–497.
115 L. Lin, H. Ou, Y. Zhang and X. Wang, *ACS Catal.*, 2016, **6**, 3921–3931.
116 X. Zhou, Y. Shi, W. Xu, Y. Wang, Y. Zhang, Y. Wang, Y. Wu, N. Wu, Y. Sun, Y. Du and W. Zhong, *J. Alloys Compd.*, 2020, **827**, 154307.
117 W. Xing, W. Tu, Z. Han, Y. Hu, Q. Meng and G. Chen, *ACS Energy Lett.*, 2018, **3**, 514–519.
118 M. K. Bhunia, S. Melissen, M. R. Parida, P. Sarawade, J.-M. Basset, D. H. Anjum, O. F. Mohammed, P. Sautet, T. Le Bahers and K. Takanabe, *Chem. Mater.*, 2015, **27**, 8237–8247.
119 X. Wu, H. Ma, W. Zhong, J. Fan and H. Yu, *Appl. Catal., B*, 2020, **271**, 118899.
120 H. Yu, H. Ma, X. Wu, X. Wang, J. Fan and J. Yu, *Sol. RRL*, 2020, **5**, 2000372.
121 Z. Zeng, X. Quan, H. Yu, S. Chen and S. Zhang, *J. Catal.*, 2019, **375**, 361–370.
122 W. Wang, Z. Shu, J. Zhou, D. Meng, Z. Zhao and T. Li, *J. Mater. Chem. A*, 2020, **8**, 6785–6794.
123 Q. Liu, X. Wang, Q. Yang, Z. Zhang and X. Fang, *Appl. Catal., B*, 2018, **225**, 22–29.
124 X. Chen, R. Shi, Q. Chen, Z. Zhang, W. Jiang, Y. Zhu and T. Zhang, *Nano Energy*, 2019, **59**, 644–650.
125 Y. Li, D. Zhang, J. Fan and Q. Xiang, *Chin. J. Catal.*, 2021, **42**, 627–636.
126 Q. Liang, Z. Li, Z.-H. Huang, F. Kang and Q.-H. Yang, *Adv. Funct. Mater.*, 2015, **25**, 6885–6892.
127 X. Xiao, Y. Gao, L. Zhang, J. Zhang, Q. Zhang, Q. Li, H. Bao, J. Zhou, S. Miao, N. Chen, J. Wang, B. Jiang, C. Tian and H. Fu, *Adv. Mater.*, 2020, **32**, 2003082.
128 H. Wang, Y. Bian, J. Hu and L. Dai, *Appl. Catal., B*, 2018, **238**, 592–598.
129 B. Y. Zhai, H. G. Li, G. Y. Gao, Y. Wang, P. Niu, S. L. Wang and L. Li, *Adv. Funct. Mater.*, 2022, **32**, 2207375.
130 Y. Wang, X. Zhou, W. Xu, Y. Sun, T. Wang, Y. Zhang, J. Dong, W. Hou, N. Wu, L. Wu, B. Zhou, Y. Wu, Y. Du and W. Zhong, *Appl. Catal., A*, 2019, **582**, 117118.
131 G. Q. Zhang, Y. S. Xu, M. Rauf, J. Y. Zhu, Y. L. Li, C. X. He, X. Z. Ren, P. X. Zhang and H. W. Mi, *Adv. Sci.*, 2022, **9**, 2201677.
132 Y. Xu, M. Fan, W. Yang, Y. Xiao, L. Zeng, X. Wu, Q. Xu, C. Su and Q. He, *Adv. Mater.*, 2021, **33**, 2101455.
133 Z. Liu, J. Ma, M. Hong and R. Sun, *ACS Catal.*, 2023, **13**, 2106–2117.

134 W. Ren, J. Cheng, H. Ou, C. Huang, M.-M. Titirici and X. Wang, *ChemSusChem*, 2019, **12**, 3257–3262.
135 J. Yuan, Y. Tang, X. Yi, C. Liu, C. Li, Y. Zeng and S. Luo, *Appl. Catal., B*, 2019, **251**, 206–212.
136 Y. Ding, S. Maitra, C. Wang, S. Halder, R. Zheng, T. Barakat, S. Roy, L.-H. Chen and B.-L. Su, *Interdiscip. Mater.*, 2022, **1**, 213–255.
137 S. Wan, J. Xu, S. Cao and J. Yu, *Interdiscip. Mater.*, 2022, **1**, 294–308.
138 F. X. Yin, P. Q. Qin, J. S. Xu and S. W. Cao, *Acta Phys. -Chim. Sin.*, 2023, **39**, 2212062.
139 M. Chang, Z. Pan, D. Zheng, S. Wang, G. Zhang, M. Anpo and X. Wang, *ChemSusChem*, 2023, **16**, e202202255.
140 M. K. Bhunia, K. Yamauchi and K. Takanabe, *Angew. Chem., Int. Ed.*, 2014, **53**, 11001–11005.
141 G. Zhang, G. Li, Z.-A. Lan, L. Lin, A. Savateev, T. Heil, S. Zafeiratos, X. Wang and M. Antonietti, *Angew. Chem., Int. Ed.*, 2017, **56**, 13445–13449.
142 G. Zhang, M. Liu, T. Heil, S. Zafeiratos, A. Savateev, M. Antonietti and X. Wang, *Angew. Chem., Int. Ed.*, 2019, **58**, 14950–14954.
143 J. Kröger, A. Jiménez-Solano, G. Savasci, P. Rovó, I. Moudrakovski, K. Küster, H. Schlomberg, H. A. Vignolo-González, V. Duppel, L. Grunenberg, C. B. Dayan, M. Sitti, F. Podjaski, C. Ochsenfeld and B. V. Lotsch, *Adv. Energy Mater.*, 2021, **11**, 2003016.
144 X. Liu, B. Jing, G. Lun, Y. Wang, X. Wang, C. Fang, Z. Ao and C. Li, *Chem. Commun.*, 2020, **56**, 3179–3182.
145 S. Bai, L. Wang, Z. Li and Y. Xiong, *Adv. Sci.*, 2017, **4**, 1600216.
146 J. Yu, J. Low, W. Xiao, P. Zhou and M. Jaroniec, *J. Am. Chem. Soc.*, 2014, **136**, 8839–8842.
147 X. Liang, S. Xue, C. Yang, X. Ye, Y. Wang, Q. Chen, W. Lin, Y. Hou, G. Zhang, M. Shalom, Z. Yu and X. Wang, *Angew. Chem., Int. Ed.*, 2023, **62**, e202216434.
148 T. Kawahara, Y. Konishi, H. Tada, N. Tohge, J. Nishii and S. Ito, *Angew. Chem., Int. Ed.*, 2002, **41**, 2811–2813.
149 J. Zhang, Q. Xu, Z. Feng, M. Li and C. Li, *Angew. Chem., Int. Ed.*, 2008, **47**, 1766–1769.
150 J. Zhang, M. Zhang, R.-Q. Sun and X. Wang, *Angew. Chem., Int. Ed.*, 2012, **51**, 10145–10149.
151 Q. Liang, Z. Li, Y. Bai, Z.-H. Huang, F. Kang and Q.-H. Yang, *Small*, 2017, **13**, 1603182.
152 Z. Liu, G. Wang, H.-S. Chen and P. Yang, *Chem. Commun.*, 2018, **54**, 4720–4723.
153 Z. Jiang, X. Zhang, J. Wang, L. Chen, H.-S. Chen and P. Yang, *Chem. Commun.*, 2018, **54**, 13519–13522.
154 M. Z. Rahman, J. Moffatt and N. Spooner, *Mater. Horiz.*, 2018, **5**, 553–559.
155 X. Zhang, J.-P. Veder, S. He and S. P. Jiang, *Chem. Commun.*, 2019, **55**, 1233–1236.
156 H. Liu, D. Chen, Z. Wang, H. Jing and R. Zhang, *Appl. Catal., B*, 2017, **203**, 300–313.
157 A. Jin, Y. Jia, C. Chen, X. Liu, J. Jiang, X. Chen and F. Zhang, *J. Phys. Chem. C*, 2017, **121**, 21497–21509.
158 Z. Zeng, H. Yu, X. Quan, S. Chen and S. Zhang, *Appl. Catal., B*, 2018, **227**, 153–160.
159 G. Zhang, L. Lin, G. Li, Y. Zhang, A. Savateev, S. Zafeiratos, X. Wang and M. Antonietti, *Angew. Chem., Int. Ed.*, 2018, **57**, 9372–9376.
160 A. Jin, X. Liu, M. Li, Y. Jia, C. Chen and X. Chen, *ACS Sustainable Chem. Eng.*, 2019, **7**, 5122–5133.
161 Y. Li, F. Gong, Q. Zhou, X. Feng, J. Fan and Q. Xiang, *Appl. Catal., B*, 2020, **268**, 118381.
162 J. Zhang, X. C. Liang, C. Zhang, L. H. Lin, W. D. Xing, Z. Y. Yu, G. G. Zhang and X. C. Wang, *Angew. Chem., Int. Ed.*, 2022, **61**, e202210849.
163 R. Paul, Q. Zhai, A. K. Roy and L. Dai, *Interdiscip. Mater.*, 2022, **1**, 28–50.
164 H. Zhang, F. Liu, Z. Mou, X. Liu, J. Sun and W. Lei, *Chem. Commun.*, 2016, **52**, 13020–13023.
165 H. Zhang, Y. Cao, L. Zhong, X. Cao, J. He, J. Sun and W. Lei, *Appl. Surf. Sci.*, 2019, **485**, 361–367.
166 M. Wang, S. Huang, X. Pang, M. Song, C. Du and Y. Su, *Sustainable Energy Fuels*, 2019, **3**, 3422–3429.
167 X. Yan, G. Ning and P. Zhao, *Catalysts*, 2019, **9**, 55.
168 X. Zhang, S. He and S. P. Jiang, *Carbon*, 2020, **156**, 488–498.
169 G. Chen, Z. Zhou, B. Li, X. Lin, C. Yang, Y. Fang, W. Lin, Y. Hou, G. Zhang and S. Wang, *J. Environ. Sci.*, 2023, DOI: **10.1016/j.jes.2023.05.028**.
170 G. Chen, F. Wei, Z. Zhou, B. Su, C. Yang, X. F. Lu, S. Wang and X. Wang, *Sustainable Energy Fuels*, 2023, **7**, 381–388.
171 N. A. Rodriguez, A. Savateev, M. A. Grela and D. Dontsova, *ACS Appl. Mater. Interfaces*, 2017, **9**, 22941–22949.
172 F. Guo, X. Huang, Z. Chen, H. Sun and L. Chen, *Chem. Eng. J.*, 2020, **395**, 125118.
173 M. Wang, Z. Zhang, Z. Chi, L. L. Lou, H. Li, H. Yu, T. Ma, K. Yu and H. Wang, *Adv. Funct. Mater.*, 2023, **33**, 2211565.
174 L. Cheng, X. Y. Yue, J. J. Fan and Q. J. Xiang, *Adv. Mater.*, 2021, **34**, 2200929.
175 Y. Xia, Z. Tian, T. Heil, A. Meng, B. Cheng, S. Cao, J. Yu and M. Antonietti, *Joule*, 2019, **3**, 2792–2805.
176 F. Yang, D. Deng, X. Pan, Q. Fu and X. Bao, *Natl. Sci. Rev.*, 2015, **2**, 183–201.
177 S. Cao, F. Tao, Y. Tang, Y. Li and J. Yu, *Chem. Soc. Rev.*, 2016, **45**, 4747–4765.
178 G. Vile, D. Albani, M. Nachtegaal, Z. Chen, D. Dontsova, M. Antonietti, N. Lopez and J. Perez-Ramirez, *Angew. Chem., Int. Ed.*, 2015, **54**, 11265–11269.
179 X. Li, W. Bi, L. Zhang, S. Tao, W. Chu, Q. Zhang, Y. Luo, C. Wu and Y. Xie, *Adv. Mater.*, 2016, **28**, 2427–2431.
180 S. Cao, H. Li, T. Tong, H.-C. Chen, A. Yu, J. Yu and H. M. Chen, *Adv. Funct. Mater.*, 2018, **28**, 1802169.
181 L. Zhang, R. Long, Y. Zhang, D. Duan, Y. Xiong, Y. Zhang and Y. Bi, *Angew. Chem., Int. Ed.*, 2020, **59**, 6224–6229.
182 J. Wang, T. Heil, B. Zhu, C.-W. Tung, J. Yu, H. M. Chen, M. Antonietti and S. Cao, *ACS Nano*, 2020, **14**, 8584–8593.
183 H. Li, B. Zhu, B. Cheng, G. Luo, J. Xu and S. Cao, *J. Mater. Sci. Technol.*, 2023, **161**, 192–200.
184 Y. Li, B. Li, D. Zhang, L. Cheng and Q. Xiang, *ACS Nano*, 2020, **14**, 10552–10561.
185 L. Lin, C. Wang, W. Ren, H. Ou, Y. Zhang and X. Wang, *Chem. Sci.*, 2017, **8**, 5506–5511.

186 Y. F. Shao, X. Q. Hao, S. D. Lu and Z. L. Jin, *Chem. Eng. J.*, 2023, **454**, 140123.
187 M. Liu, G. Zhang, X. Liang, Z. Pan, D. Zheng, S. Wang, Z. Yu, Y. Hou and X. Wang, *Angew. Chem., Int. Ed.*, 2023, **62**, e202304694.
188 Q. Wang, G. Zhang, W. Xing, Z. Pan, D. Zheng, S. Wang, Y. Hou and X. Wang, *Angew. Chem., Int. Ed.*, 2023, **62**, e202307930.
189 M. Liu, C. Wei, H. Zhuzhang, J. Zhou, Z. Pan, W. Lin, Z. Yu, G. Zhang and X. Wang, *Angew. Chem., Int. Ed.*, 2022, **61**, e202113389.
190 D. Dontsova, S. Pronkin, M. Wehle, Z. Chen, C. Fettkenhauer, G. Clavel and M. Antonietti, *Chem. Mater.*, 2015, **27**, 5170–5179.
191 A. B. Jorge, D. J. Martin, M. T. S. Dhanoa, A. S. Rahman, N. Makwana, J. Tang, A. Sella, F. Cora, S. Firth, J. A. Darr and P. F. McMillan, *J. Phys. Chem. C*, 2013, **117**, 7178–7185.
192 Z. Chen, A. Savateev, S. Pronkin, V. Papaefthimiou, C. Wolff, M. G. Willinger, E. Willinger, D. Neher, M. Antonietti and D. Dontsova, *Adv. Mater.*, 2017, **29**, 1700555.
193 J. Kroger, A. Jimenez-Solano, G. Savasci, V. W. H. Lau, V. Duppel, I. Moudrakovski, K. Kuster, T. Scholz, A. Gouder, M. L. Schreiber, F. Podjaski, C. Ochsenfeld and B. V. Lotsch, *Adv. Funct. Mater.*, 2021, **31**, 2102468.
194 J. Kroger, F. Podjaski, G. Savasci, I. Moudrakovski, A. Jimenez-Solano, M. W. Terban, S. Bette, V. Duppel, M. Joos, A. Senocrate, R. Dinnebier, C. Ochsenfeld and B. V. Lotsch, *Adv. Mater.*, 2022, **34**, 2107061.
195 Y. Li, D. N. Zhang, J. J. Fan and Q. J. Xiang, *Chin. J. Catal.*, 2021, **42**, 627–636.
196 D. B. Nimbalkar, V. Nguyen, C. Y. Shih and H. S. Teng, *Appl. Catal., B*, 2022, **316**, 121601.
197 Z. M. Pan, M. Zhao, H. Y. Zhuzhang, G. G. Zhang, M. Anpo and X. C. Wang, *ACS Catal.*, 2021, **11**, 13463–13471.
198 D. Dontsova, C. Fettkenhauer, V. Papaefthimiou, J. Schmid and M. Antonietti, *Chem. Mater.*, 2016, **28**, 772–778.
199 A. Savateev, S. Pronkin, J. D. Epping, M. G. Willinger, C. Wolff, D. Neher, M. Antonietti and D. Dontsova, *ChemCatChem*, 2017, **9**, 167–174.
200 A. Savateev, S. Pronkin, M. G. Willinger, M. Antonietti and D. Dontsova, *Chem. – Asian J.*, 2017, **12**, 1517–1522.
201 G. Zhang, G. Li, T. Heil, S. Zafeiratos, F. Lai, A. Savateev, M. Antonietti and X. Wang, *Angew. Chem., Int. Ed.*, 2019, **58**, 3433–3437.
202 L. Lin, W. Ren, C. Wang, A. M. Asiri, J. Zhang and X. Wang, *Appl. Catal., B*, 2018, **231**, 234–241.
203 R. Lei, B. Du, X. Lai, J. Wu, Z. Zhang, S. Liu, R. Wu, X. Li, B. Song and J. Jian, *J. Mater. Chem. A*, 2019, **7**, 13234–13241.
204 Y. Dai, Q. Bu, R. Sooriyagoda, P. Tavadze, O. Pavlic, T. Lim, Y. Shen, A. Mamakhel, X. Wang, Y. Li, H. Niemantsverdriet, B. B. Iversen, F. Besenbacher, T. Xie, J. P. Lewis, A. D. Bristow, N. Lock and R. Su, *J. Phys. Chem. Lett.*, 2019, **10**, 5381–5386.
205 L. Cui, X. Hou, H. Du and Y. Yuan, *Appl. Surf. Sci.*, 2020, **501**, 144259.
206 V. V. Shvalagin, G. V. Korzhak, S. Y. Kuchmiy, M. A. Skoryk, O. V. Selyshchev and D. R. T. Zahn, *J. Photochem. Photobiol., A*, 2020, **390**, 112295.
207 Y. Li, D. Zhang, X. Feng and Q. Xiang, *Chin. J. Catal.*, 2020, **41**, 21–30.
208 Y. Xu, C. Qiu, X. Fan, Y. Xiao, G. Zhang, K. Yu, H. Ju, X. Ling, Y. Zhu and C. Su, *Appl. Catal., B*, 2020, **268**, 118457.
209 L. Wang, Y. Hong, E. Liu, Z. Wang, J. Chen, S. Yang, J. Wang, X. Lin and J. Shi, *Int. J. Hydrogen Energy*, 2020, **45**, 6425–6436.
210 P. Deng, L. Shi, H. Wang and W. Qi, *Colloids Surf., A*, 2020, **601**, 125023.
211 G. Q. Zhang, Y. S. Xu, C. X. He, P. X. Zhang and H. W. Mi, *Appl. Catal., B*, 2021, **283**, 119636.
212 G. Q. Zhang, Y. S. Xu, D. F. Yan, C. A. X. He, Y. L. Li, X. Z. Ren, P. X. Zhang and H. W. Mi, *ACS Catal.*, 2021, **11**, 6995–7005.
213 W. B. Wang, Z. Shu, Z. H. Liao, J. Zhou, D. W. Meng, T. T. Li, Z. L. Zhao and L. Xu, *Chem. Eng. J.*, 2021, **424**, 130332.
214 H. N. Che, C. M. Li, C. X. Li, C. B. Liu, H. J. Dong and X. H. Song, *Chem. Eng. J.*, 2021, **410**, 127791.
215 Z. Z. Sun, H. Z. Dong, Q. Yuan, Y. Y. Tan, W. Wang, Y. B. Jiang, J. Y. Wan, J. W. Wen, J. J. Yang, J. Q. He, T. Cheng and L. M. Huang, *Chem. Eng. J.*, 2022, **435**, 134865.
216 Z. H. Yu, X. Y. Yue, J. J. Fan and Q. J. Xiang, *ACS Catal.*, 2022, **12**, 6345–6358.
217 G. Q. Zhang, J. Y. Zhu, Y. S. Xu, C. Yang, C. X. He, P. X. Zhang, Y. L. Li, X. Z. Ren and H. W. Mi, *ACS Catal.*, 2022, **12**, 4648–4658.
218 Y. J. Wang, D. J. Xie, G. Wang, Y. S. Wu, R. Shi, C. Zhou, X. F. Meng and T. R. Zhang, *Nano Energy*, 2022, **104**, 107938.
219 F. Lin, S. Zhou, G. H. Wang, J. Wang, T. Y. Gao, Y. R. Su and C. P. Wong, *Nano Energy*, 2022, **99**, 107432.
220 S. H. Shen, J. Chen, Y. Q. Wang, C. L. Dong, F. Q. Meng, Q. H. Zhang, Y. L. Huangfu, Z. Lin, Y. C. Huang, Y. R. Li, M. T. Li and L. Gu, *Sci. Bull.*, 2022, **67**, 520–528.
221 S. F. An, Y. K. Guo, X. Y. He, P. Gao, G. J. Hou, J. G. Hou, C. S. Song and X. W. Guo, *Appl. Catal., B*, 2022, **310**, 121323.
222 T. Y. Yang, Y. Y. Shao, J. D. Hu, J. F. Qu, X. G. Yang, F. Y. Yang and C. M. Li, *Chem. Eng. J.*, 2022, **448**, 137613.
223 X. Li, J. Wen, J. Low, Y. Fang and J. Yu, *Sci. China Mater.*, 2014, **57**, 70–100.
224 H. Li, B. Zhu, S. Cao and J. Yu, *Chem. Commun.*, 2020, **54**, 5641–5644.
225 Y. Liang, X. Wu, X. Liu, C. Li and S. Liu, *Appl. Catal., B*, 2022, **304**, 120978.
226 H. Li, F. Li, J. Yu and S. Cao, *Acta Phys. -Chim. Sin.*, 2021, **37**, 2010073.
227 L. Cheng, P. Zhang, Q. Y. Wen, J. J. Fan and Q. J. Xiang, *Chin. J. Catal.*, 2022, **43**, 451–460.
228 J. Wu, X. Ji, X. Yuan, Z. Zhao, Y. Li, B. Wen, H. Zhang, D. Yu, Y. Zhao and Y. Tian, *Chem. Mater.*, 2019, **31**, 9188–9199.
229 L. Tian, J. Li, F. Liang, J. Wang, S. Li, H. Zhang and S. Zhang, *Appl. Catal., B*, 2018, **225**, 307–313.
230 Y. Yu and J. Wang, *Ceram. Int.*, 2016, **42**, 4063–4071.
231 Q. Liang, Z.-H. Huang, F. Kang and Q.-H. Yang, *ChemCatChem*, 2015, **7**, 2897–2902.

232 C. Fettkenhauer, X. Wang, K. Kailasam, M. Antonietti and D. Dontsova, *J. Mater. Chem. A*, 2015, **3**, 21227–21232.
233 L. H. Amorin, V. Y. Suzuki, N. H. de Paula, J. L. Duarte, M. A. Toledo da Silva, C. A. Taft and F. D. A. La Porta, *New J. Chem.*, 2019, **43**, 13647–13653.
234 Y. Duan, J. Li, X. Shang, D. Jia, C. Li and S. Liu, *J. Mater. Sci.*, 2020, **55**, 13675–13686.
235 Y. Wang, B. Jing, F. Wang, S. Wang, X. Liu, Z. Ao and C. Li, *Water Res.*, 2020, **180**, 115925.
236 V. Vinoth Kumar, D. Avisar, V. Lakshmi Prasanna, Y. Betzalel and H. Mamane, *J. Hazard. Mater.*, 2020, **398**, 122880.
237 J. J. Wang, P. Li, Y. Wang, Z. Y. Liu, D. Q. Wang, J. J. Liang and Q. H. Fan, *Adv. Sci.*, 2023, **10**, 2205542.
238 Z. Y. Gu, Z. T. Cui, Z. J. Wang, T. R. Chen, P. Sun and D. W. Wen, *J. Mater. Sci. Technol.*, 2021, **83**, 113–122.
239 M. Zhou, L. B. Zeng, R. Li, C. Yang, X. Qin, W. K. Ho and X. C. Wang, *Appl. Catal., B*, 2022, **317**, 121719.
240 Y. Zhang, L. Hu, C. Zhu, J. Liu, H. Huang, Y. Liu and Z. Kang, *Catal. Sci. Technol.*, 2016, **6**, 7252–7258.
241 M. Zhou, P. Yang, R. Yuan, A. M. Asiri, M. Wakeel and X. Wang, *ChemSusChem*, 2017, **10**, 4451–4456.
242 B. Pieber, J. A. Malik, C. Cavedon, S. Gisbertz, A. Savateev, D. Cruz, T. Heil, G. Zhang and P. H. Seeberger, *Angew. Chem., Int. Ed.*, 2019, **58**, 9575–9580.
243 C. Cavedon, A. Madani, P. H. Seeberger and B. Pieber, *Org. Lett.*, 2019, **21**, 5331–5334.
244 J. Wang, H. Zhao, B. C. Zhu, S. Larter, S. W. Cao, J. G. Yu, M. G. Kibria and J. G. Hu, *ACS Catal.*, 2021, **11**, 12170–12178.
245 M. A. R. da Silva, I. F. Silva, Q. Xue, B. T. W. Lo, N. V. Tarakina, B. N. Nunes, P. Adler, S. K. Sahoo, D. W. Bahnemann, N. Lopez-Salas, A. Savateev, C. Ribeiro, T. D. Kuhne, M. Antonietti and I. F. Teixeira, *Appl. Catal., B*, 2022, **304**, 120965.
246 A. Savateev, D. Dontsova, B. Kurpil and M. Antonietti, *J. Catal.*, 2017, **350**, 203–211.
247 B. Kurpil, K. Otte, M. Antonietti and A. Savateev, *Appl. Catal., B*, 2018, **228**, 97–102.
248 B. Kurpil, B. Kumru, T. Heil, M. Antonietti and A. Savateev, *Green Chem.*, 2018, **20**, 838–842.
249 A. Savateev, B. Kurpil, A. Mishchenko, G. Zhang and M. Antonietti, *Chem. Sci.*, 2018, **9**, 3584–3591.
250 B. Kurpil, Y. Markushyna and A. Savateev, *ACS Catal.*, 2019, **9**, 1531–1538.
251 Y. Markushyna, C. Teutloff, B. Kurpil, D. Cruz, I. Lauermann, Y. Zhao, M. Antonietti and A. Savateev, *Appl. Catal., B*, 2019, **248**, 211–217.
252 B. Kurpil, K. Otte, A. Mishchenko, P. Lamagni, W. Lipinski, N. Lock, M. Antonietti and A. Savateev, *Nat. Commun.*, 2019, **10**, 945.
253 A. Savateev, N. V. Tarakina, V. Strauss, T. Hussain, K. ten Brummelhuis, J. M. Sanchez Vadillo, Y. Markushyna, S. Mazzanti, A. P. Tyutyunnik, R. Walczak, M. Oschatz, D. M. Guldi, A. Karton and M. Antonietti, *Angew. Chem., Int. Ed.*, 2020, **59**, 15061–15068.
254 Y. Markushyna, C. M. Schusslbauer, T. Ullrich, D. M. Guldi, M. Antonietti and A. Savateev, *Angew. Chem., Int. Ed.*, 2021, **60**, 20543–20550.
255 C. Yang, S. Wan, B. Zhu, J. Yu and S. Cao, *Angew. Chem., Int. Ed.*, 2022, **61**, e202208438.
256 J. Cheng, S. Wan and S. Cao, *Angew. Chem., Int. Ed.*, 2023, **62**, e202310476.
257 G. G. Kramarenko, S. G. Hummel, S. M. Martin and G. R. Buettner, *Photochem. Photobiol.*, 2006, **82**, 1634–1637.
258 H. Mattila, S. Khorobrykh, V. Havurinne and E. Tyystjärvi, *J. Photochem. Photobiol., B*, 2015, **152**, 176–214.
259 Y. Nosaka and A. Y. Nosaka, *Chem. Rev.*, 2017, **117**, 11302–11336.
260 S. Zhao and X. Zhao, *Appl. Catal., B*, 2019, **250**, 408–418.
261 H. Cheng, J. Cheng, L. Wang and H. X. Xu, *Chem. Mater.*, 2022, **34**, 4259–4273.
262 L. Wang, J. Zhang, Y. Zhang, H. Yu, Y. Qu and J. Yu, *Small*, 2022, **18**, 2104561.
263 J. D. Hu, C. Chen, H. B. Yang, F. Y. Yang, J. F. Qu, X. G. Yang, W. Sun, L. M. Dai and C. M. Li, *Appl. Catal., B*, 2022, **317**, 121723.
264 H. Guo, C. G. Niu, C. Liang, H. Y. Niu, Y. Y. Yang, H. Y. Liu, N. Tang and H. X. Fang, *Chem. Eng. J.*, 2021, **409**, 128030.
265 P. Sharma, T. J. A. Slater, M. Sharma, M. Bowker and C. R. A. Catlow, *Chem. Mater.*, 2022, **34**, 5511–5521.
266 L.-L. Liu, F. Chen, J.-H. Wu, J.-J. Chen and H.-Q. Yu, *Proc. Natl. Acad. Sci. U. S. A.*, 2023, **120**, e2215305120.